Modeling and Structural Optimization of Solid Oxide Fuel Cells

Panagakos, Grigorios; Okkels, Fridolin

Publication date:
2013

Document Version
Publisher's PDF, also known as Version of record

Technical University of Denmark (DTU)
Department of Micro- and Nanotechnology

Doctor of Philosophy Dissertation

Modeling and Structural Optimization of Solid Oxide Fuel Cells

by

Grigorios Panagakos

Supervisor: Associate Prof. Fridolin Okkels

Kongens Lyngby, 2013

Abstract

The research conducted in the context of this PhD, lies on the cross section between multi-scale modeling of flow in porous media, electrochemical diffusion and reaction, in combination with Shape and Structural Optimization techniques. More specifically, we have followed two lines of action for dealing with this problem. On the one hand, we attempt to perform optimization of a Solid Oxide Fuel Cell in the macro scale. Focusing on the anode interconnect, we wish to come up with an optimum interconnect design. This can be achieved in principal, since the interconnect needs to satisfy two major requirements. On the one hand, it needs to secure the intake of fuel into the cell, fact that would require an as low hydraulic resistance as possible, i.e. ideally an open channel and on the other hand to exhibit an as high as possible electronic conductance, which in the ideal case would mean an area blocked completely by a material with high conductivity such as coated stainless steel. The balance between these two competing, oppositely driving forces, indicate that there should be a design that satisfies in the best way both. Similar problems have been successfully dealt by structural-topology optimization approaches and this is one of the first attempts to apply this combination of set of tools to fuel cells. Describing in a nutshell the methodology followed, we use Comsol's ability to create Matlab scripts which incorporate the desired physics of the problem (Partial Differential Equations, treating the setup as continuum) and we combine these scripts with the ones containing the optimization routines like the Method of Moving Asymptotes (MMA). Success in obtaining such a design, would greatly affect the overall cell's efficiency rendering the Solid Oxide Fuel Cell more competitive in the sustainable energy basket of solutions. In this project, consulting role was also undertaken by researchers at National Center for Sustainable Energy, Risø and more specifically by Dr. Martin Søgaard, Dr. Henrik Frandsen and Dr. Peter Vang Hendriksen (team leader).

The other approach is based on attacking the problem in the micro-scale. Taking as starting point the homogenization method for getting an upscaled equation for the diffusion of ion vacancies in a fuel cell's cathode, we derive formulas that express the Area Specific Resistance (ASR) of the electrode as a function of geometric parameters, such as the tortuosity and the porosity of the material, for preselected micro-structures. Furthermore, we apply optimization techniques to lead this ASR to minimization. This work has been the fruit of collaboration with Professor Sossina Haile at the California Institute of Technology (Caltech) and with assistant Professor Francesco Ciucci at the Hong Kong University of Science and Technology (HKUST).

As a complementary in this modeling work, we have also developed other activities, leading to either already accepted, submitted or soon to be submitted publications. These additional to the main focus directions, have had three components. In chronological terms, first was the experimental contribution to the calculation of the

optimum percentage of Zirconium in Zirconium Doped Ceria (ZDC) in the context of my external stay at the California Institute of Technology. Secondly, we have also participated in testing the compound of magnesium hydrides encapsulated in PMMA for a set of experiments aiming at the development of a mass production method through laser ablation for cheap and effective hydrogen storage. This work was done in collaboration with Dr. Athanasios Stubos at the National Center for Scientific Research, in Athens, Hellas. Towards the end of the PhD, we have also worked close with Professor Ciucci once more, on assessing the identifiability of the physical parameters, surface reaction rate k and bulk diffusion coefficient D, as functions of the Biot number and the normalized by the diffusional time scale annealing time, in Isotope Exchange Depth Profiling Measurements (IEDP). Besides computing the expected relative errors, we have also proposed a novel approximation for the confidence intervals on k and D.

Populært dansk resume

Denne Ph.D. afhandling, med engelsk titel: "Modeling and Structural Optimization of Solid Oxide Fuel Cells", udgør en større del af Forskningsprojektet EnergyShaping - "Topolgy optimization of Solid Oxide Fuel Cells and Magnetic refrigeration systems", som er støttet af Forskningsrådet for Teknologi og Produktion.

Afhandlingen omhandler matematisk og numerisk modellering og strukturel optimering af "Solid Oxide" brændselsceller, som er en meget alsidig type brændselscelle idet den fx kan køre på naturgas og luft. Da brændselsceller generelt har en meget høj effektivitet, og både producerer elektricitet og overskudsvarme, vil den nationalt og internationalt planlagte udbredelse af brændselsceller fremme en bæredygtig energiproduktion.

Afhandlingens to dele omfatter modellering og strukturel optimering af to essentielle dele of brændselsceller, som også involverer strukturer på to størrelses-skalaer: På mm-skala transporteres og fordeles brændselsgas og luft ind i og igennem brændselscellen vha. en "interconnect" struktur, og da denne struktur også skal lede den producerede elektriske strøm mellem brændselscellerne er der et stort behov for at optimere de strukturelle bestanddele af interconnect'en. På mikrometer-skala har strukturen af de porøse membran-elementer i brændselscellen stor betydning for effektiviteten af de elektrokemiske reaktioner som driver cellen. I afhandlingen er der udviklet et nyt matematisk værktøj som kan benyttes til bedre at evaluere mulige membran-mikrostrukturer.

Acknowledgements

Every journey when thought over after or near its end, bares a lot of mixed memories. Anxieties and victories, options and decisions made all together form the path of who we are and what we have done. But all of these moments are connected to our interaction with those who are close to us. In this way these few words are a tribute to those who were significant parts of this effort of mine the last four years of my life.
In the beginning, I would like to thank my supervisor Fridolin Okkels for choosing me and assigning to me the undertaking of the tasks emanating from the EnergyShaping project with respect to Fuel Cells, and providing me with the chance to come to Denmark and become a member of its lively research community. I also wish to thank him for broadening my horizons with his perspective on research and problem solving.
Secondly, I would like to thank the Department for Micro-and-Nano Technology for making me part of its family and for providing me with the necessary resources the first three years of my PhD to be focused on fulfilling the academic requirements of the studies. I also wish to thank DTU overall for the fertile academic environment I have experienced.

Part of the work initiated in the context of the EnergyShaping project was done in collaboration with researchers from the Danish National Center for Sustainable Energy, Risœ. In this context, I would like to thank group leader Peter Vang Hendriksen, Dr. Martin Søgaard and Dr. Henrik Lund Frandsen for their valuable contribution, many times well beyond any professional obligation, in helping me to form a realistic background for the development of my modeling.
I wish to also extend my gratitude, deep appreciation and respect to Professor Sossina Haile at the California Institute of Technology (Caltech) who invited me to visit her group and for mentoring me while I was there. Beyond the merits emerging just from visiting an academic and research environment of the caliber of a top world-class Institute like Caltech, I also got the chance to interact and learn from inspired PhD students, researchers and professors. I wish to thank especially Dr. Yong Hao, who hosted me in the group, for guiding me through my small contribution in the experimental work I performed. An additional reason for being grateful to Professor Haile, is her introduction to Dr. Francesco Ciucci and her suggestion that we should work together since we seemed to be of similar backgrounds and shared similar passions about theoretical work and mathematically based modeling. Dr. Ciucci, PhD Caltech allumni, a post doc at the university of Heidelberg at the time of the introduction and soon after an Assistant Professor at the Hong Kong University of Science and Technology (HKUST), has proven to be an invaluable source of both academic inspiration through his excellent and high standard academic work, and of personal motivation through difficult times. I wish to thank Professor Ciucci from the bottom

of my heart for his support and belief in me and for the rare human qualities he has demonstrated ever since I met him. Finally, with respect to the external stays, special thanks also go to the Otticon and Otto Møndsteds Foundations, on whose kind financial support the external stays at HKUST and Caltech were realized.

I wish to also thank Dr Athanasios Stubos, group leader and Head of the Environmental Research Laboratory (EREL) at the National Center for Scientific Researcher "Demokritos" in Athens, for honoring me not only as a collaborator in the production of our mutual publication but also with his sincere, unselfish friendship and impecable academic mentoring.
Furthermore, I wish to thank my friends and fellow PhD students at DTU Nanotech, Dr. Mathias Bækbo Andersen, Dr. Rune Barnkob, and soon Drs to be, Kristian Ejlebjærg Jensen and Andrea Cavalli for sharing the mutual burdens of our academic endeavors, through nice discussions, and also our human sides and for being there for me when I needed a hand of help.

The unseen heroes beneath my effort to bring the PhD to an end, friends and family, have played the most vital role, in supporting me not only financially the last year of my stay in Denmark, but also morally and psychologically and for believing in me even when I was about to stop believing in myself. If I have accomplished anything all the credit should go to them who suffered with me, and to God for bringing these wonderful people in my life. Their presence alone, was a blessing and in the same time the most important lesson in terms of holding the faith that even through darkest times, light will eventually shine and the journey's end will be an honorable one, for those who fight for it.

To my beloved family

Contents

List of Symbols and Abbreviations

Abbreviation	Description	Units
SOFC	Solid Oxide Fuel Cell	
PEM	Proton Electron Membrane	
CTE	Coefficient of Thermal Expansion	
YSZ	Yttria Stabilized Zirconia	
GDC	Gadolinium Doped Ceria	
LSM	Lanthanum Strontium Manganite	
LSC	Lanthanum Strontium Ceria	
LSCF	Lanthanum Strontium Cobaltite Ferrite	
FEM	Finite Element Method	
PDE	Partial Differential Equation	
MEA	Membrane Electrode Assembly	
MIEC	Mixed Ionic Electronic Conductor	
an	Anode	
as	Anode Support	
ic	Interconnect	
gc	Gas Channel	
cc	Current Collector	
Re	Reynolds number	
Pe	Peclet number	
x, y, z	Rectangular Coordinate vectors	m
r, θ, z	Cylindrical Coordinate vectors	m,rad,m
t	Time	s
T	Temperature	C, K
R	Universal Gas Constant	$8.314 \frac{Joule}{molK}$
P	Pressure	Pa
ρ	Density	$\frac{kg}{m^3}$
$\mathbf{u}, u_j$	2D Velocity field with components u_j	$\frac{m}{s}$
ω	Total mass source term	$\frac{kg}{m^3 s}$
μ	Dynamic viscosity	$Pa \cdot s$

Abbreviation	Description	Units
ν	Kinematic viscosity	$\frac{m^2}{s}$
σ_{ij}	Total stress tensor	Pa
τ_{ij}	Shear stress tensor	Pa
f_i	Body forces	N
ζ	Secondary viscosity coefficient	$Pa \cdot s$
α, α_{min}	Damping factor for open channel	$\frac{Pa \cdot s}{m^2}$
χ	Vorticity vector	$\frac{1}{s}$
$\mathbf{B}$	Vector potential	$\frac{m^2}{s}$
Ψ	Stream function	$\frac{m^2}{s}$
R	Cylinder's (pillar) diameter	m
f	Spatial variation of stream function	$\frac{m^2}{s}$
U	Far field velocity	$\frac{m}{s}$
k	Auxiliary coefficient	$\frac{1}{m}$
ξ	Normalized inverse Re	
B_m	Stream function expansion coefficient	
F_D	Drag force on a cylinder	N
ψ_D	Fluid dissipation function per unit area per unit length in the z direction	$\frac{Pa}{s}$
Ψ_D	Fluid dissipation function	W
Φ	Potential	V
σ	Electrical conductivity	$\frac{S}{m}$
h	height	m
$\Omega_{1,2}$	Domain with indices 1 or 2	
$Sa_{an} \cdot i_{ct}$	Volumetric current density	$\frac{A}{m^3}$
c_1	Constant	$\frac{1}{m}$
J_n, Y_n, I_n, K_n	Bessel and modified Bessel functions	
c_2	Constant	$\frac{\sqrt{V}}{m}$
i	area current density in the z direction	$\frac{A}{m^2}$
$\vec{J}_1, \vec{J}_2$	current flux in the r direction	$\frac{A}{m^2}$
V_N	Nerst potential	V
V_{cell}	Cell potential	V
V_p^{an}	Polarization potential loss	V
V_{diff}^{an}	Diffusion potential loss	V
R_p	polarization specific resistance	$\Omega \cdot m^2$
A^{an}	specific resistance constant	$\Omega \cdot m^2$
E_a^{an}	Activation Energy	$\frac{J}{mol}$
x_{H_2}, x_{H_2}	Hydrogen and Oxygen molar fractions	
D_{ij}	Binary Diffusion coefficient	$\frac{m^2}{s}$
D^{eff}	Diffusion coefficient in the porous anode support including correction on the binary and the Knudsen diffusion	$\frac{m^2}{s}$
D_{ij}^{eff}	Corrected binary diffusion coefficient in the porous anode support	$\frac{m^2}{s}$
D_K	Knudsen Diffusion coefficient in the porous anode support	$\frac{m^2}{s}$

Abbreviation	Description	Units
Σ	Diffusive volume	
d_p	Pore size	m
d_{part}	Particle size of which the anode constitutes of.	m
J_{H_2}, J_{H_2}	Hydrogen and Oxygen molar fluxes along the the z axis	$\frac{mol}{m^2 s}$
P_{GEN}	Power of the MEA or cell power	W
P_{JHIC}	Power of joule heating in the interconnect pillar	W
P_{Net}	Power GEN subtracting the ic joule heating and the fluid dissipation	W
γ	Domain design parameter ranging between 0 and 1	
α_{max}	Maximum damping factor in the areas where solid is introduced	$\frac{Pa \cdot s}{m^2}$
q	Parameter defining the convexity of the interpolation in the $\alpha - \gamma$ function	
w	mass fraction	
α_0	Normalized γ	
c	Concentration	$\frac{mol}{m^3}$
β	constraint volume fraction	$\frac{Pa \cdot s}{m^2}$
ε	Porosity	
α_{max}	maximum damping factor in the areas where solid is introduced	$\frac{Pa \cdot s}{m^2}$
F	Faraday' constant	$\frac{Cb}{mol}$
R_{chem}	Area Specific Resistance	$\Omega \cdot m^2$
$\widetilde{R}_{chem}$	Dimensionless Area specific Resistance	
τ	Solid phase tortuosity	
a_f, a_b	Dimensionless kinetic parameters	
r, r_0	reaction rate and exchange reaction rate	$\frac{m}{s}$
δ_p	penetration depth	m
L_{RXN}	Dimensionless cathode reactive zone.	
δ	Pore size of scale separation.	
D_V	Oxygen vacancies diffusivity	$\frac{m^2}{s}$
L_Y	micro-structure length	
$\mathcal{A}$	Specific available for reaction when $L_Y = 1$.	
$c_{Vr}ef$	Reference concentration value	$\frac{mol}{m^3}$
L_{MACRO}	Macroscopic length scale	m
L_{micro}	Microscopic length scale	
T_{RXN}	Reaction time scales	s
T_V	Oxygen vacancies diffusion time scale	s
$\mathcal{S}$	Solid phase	
Γ	Interface between solid and gas phase	
$\mathbf{x}$	Macroscopic coordinate	m
$\mathbf{y}$	Microscopic coordinate	m
$\widetilde{\mathbf{x}}$	Dimensionless macroscopic coordinate	
$\widetilde{\mathbf{y}}$	Dimensionless microscopic coordinate	

Abbreviation	Description	Units
ν	Normal unit vector on γ oriented from the solid towards the pore	

List of Figures

List of Tables

Chapter 1

Introduction

1.1 Solid Oxide Fuel Cells in general, materials and composition

The realization of the necessity for shifting from the profile of absolute dependence of our economy and energy technology on hydro-carbons and fossil fuels for the most of the 20th century to more sustainable, flexible and environment-friendly alternatives has motivated research in this direction. Fuel cells, being one of the promising technologies in the prospect of energy sustainability, have regained much attention in the last decades. Despite the fact that they have been invented in the 19th century, their full potential is far yet from being reached and there is significant room for increasing their efficiencies and enhancing their performance by minimizing the overall losses of the system, thus rendering them more competitive.

Fuel cells are devices whose working principle lies in the field of direct electrochemical conversion of some constantly supplied substances' (fuels) chemical energy to electricity. Consequently, Fuel Cells do not suffer from the Carnot's limit of efficiency, i.e. limitations from working through thermal cycles and they do not involve nor a combustion step nor the subsequent transformation to mechanical energy and then to electricity along the energy transformation process. The set of this outstanding properties have rendered Fuel Cell technology extremely popular and great expectations about them becoming a major factor in our modern societies' energy sustainable future have been put on. Research efforts by scientists from different fields, spanning from material science, and electro-chemistry to solid-state physics, mechanical and process engineering have been combined to materialize these expectations. Despite the fact that they have been invented in the 19th century, their full potential is being constantly explored and their limits expanded, historically based on experimental approaches.

However, the attempt to render Fuel Cells a competitive and viable wide-spread technology has been significantly boosted lately by computer simulations as well, enriching the traditional ways of advancement in this field.

Our choice of dealing with SOFC in particular emanates from the fact that they hold a dominant position among the direct electrochemical conversion devices, since not only do they exhibit high cell efficiency as all fuel cells, but on top of that, the highest power density of any other system. The high operating temperature of SOFCs, ranging from 600° to 800°, dictated by the necessity for high ionic conductivity in the cell and for catalyzing the reduction-oxidation half-reactions, provides the possibility for internal fuel reforming ($T > 650°C$) giving access to unique fueling versatility from hydrocarbons, to jet and commercial fuels and hydrogen [6], [7], [8], [9]. Another advantage of the high operating temperatures is the absence of need to perform water management, a very cumbersome process in other fuel cells like the PEM ones, since the water produced is in the vapor phase. The conductivity and resistance of any part of the cell is thus also not affected by the presence of water.

These characteristics, together with absence of rotating mechanical parts and noise abatement make the use of SOFC very attractive. In the same time however, their operating temperature around 800° does not favor often shut downs and startups, mainly because of the time lag in acquiring the desired load and also because of the consequent acceleration of the cell's degradation processes. The combination of the above advantages and disadvantages, have rendered SOFC the predominant option for stationary applications, while offering them a growing role in transportation as auxiliary power units as well as in other mobile applications [10], [11].

The purpose of this small overview of the material requirements and technology behind standard and state-of-the-art SOFC's is to merely set the scientific background and introduce the main concepts necessary to our work, and not to exhaust the subject, since our focus lies in the application of analytical and computational tools for modeling different parts of the cell. However, this modeling and any attempt for mathematical optimization would be incomplete or out of perspective if not combined with a solid comprehension of the basic material and electrochemical mechanisms that in broad terms take place during the operation cycle of a fuel cell.

The materials used in the different components of SOFC are mainly ceramics, or their combinations with a few metals. The core of every SOFC is an assembly of four main parts, two electrodes, an in-between solid electrolyte and the interconnect. The major electrochemical phenomena characterizing SOFC operation is the oxygen reduction at the cathode, followed by the vacancy transport of oxygen ions through the electrolyte all the way to the anode, where the oxygen

ions react with the oxidized hydrogen ions to form water and electricity. SOFC schematics in terms of the electrochemical conversion and the mass transfer for H_2 of hydrocarbon fuels are given in figure 1.5, 1.3, 1.2 and 1.4 while in figures 1.6 and 1.7 a glimpse is taken in a typical Membrane-Electrode-Assembly (MEA) micro-structure and cathode for a SOFC.

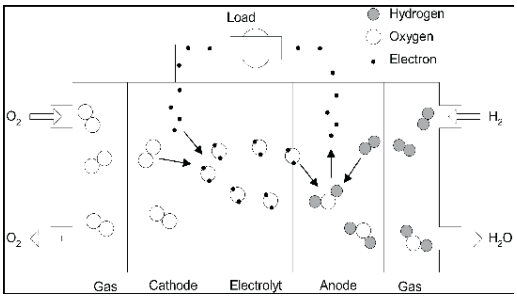

Figure 1.1: Transport of spieces within a SOFC, [1]

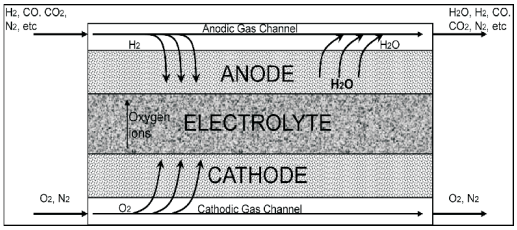

Figure 1.2: Mass transport within an SOFC, [1]

Crucial to the cell's efficiency, durability and degradation, is the chemical and mechanical stability of the materials used and the compatibility of the different components, especially with respect to the expansion strain that they suffer as a result of the cells high operating temperatures. Especially concerning the interconnect, one common source of degradation can result from the uptake of carbon coming from the anode side fueling with hydrocarbons, when carbon is in excess in the fuel. Severe material failure such as cracking or delamination can be also induced by the different behavior of the interconnect and the ceramic parts of the cell (quantified by the Coefficient of Thermal Expansion, CTE) in terms of response to thermal loads over the whole range of the operation of the cell from room temperature during start up to the final steady state temperature of the cell. In the sections describing the main layers of a SOFC we rely on a fraction of the extremely wide literature, as found in [12], [13] and [14].

1.2 Solid Oxide Fuel Cells Components

1.2.1 Electrolyte

Solid electrolytes, or super ionic conductors, are solid materials with electrical conductivity totally or partially due to conduction of ions and they can be of crystallic or semi-crystallic nature. The main mechanisms known when studying these materials are the Frenkel and Shottky suggestions about defects transport in solids. These defects can be caused both by intrinsic reasons (thermodynamic balance adjustment) and external intervention (doping). The electrolyte in SOFCs performs the key task of conducting oxygen ions O^{2-} produced at the cathode through oxygen reduction, to the anode where it combines with protons

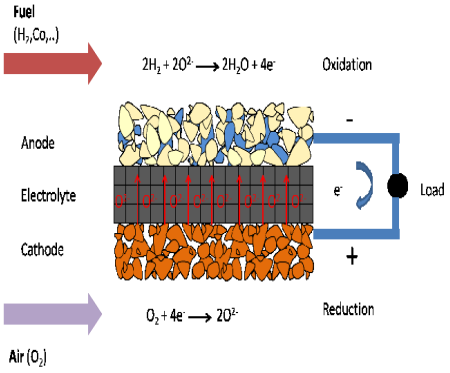

Figure 1.3: Schematic representation of the porous cell structure.

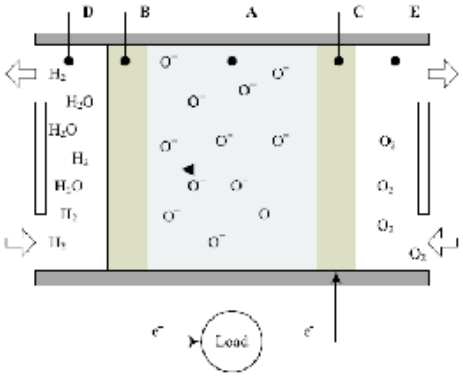

Figure 1.4: A schematic representation of a SOFC. It basically consists of: (A) a solid electrolyte layer, (B) an anode, (C) a cathode electrode, and two channels, one for the fuel (D), and one for the oxidant gas (E) [2]

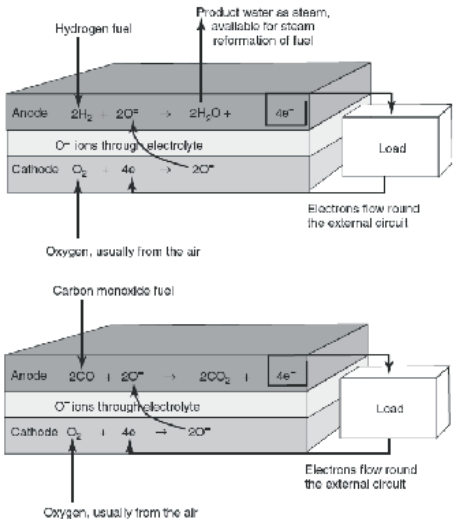

Figure 1.5: The separate anode and cathode reactions for the SOFC, when using hydrogen and carbon monoxide fuel, [3]

H^+ to form water, as shown in fig 1.1, 1.2. In this way the presence of the electrolyte secures closing of the system and completion of the overall electrochemical reaction. The selection of material for an ideal electrolyte for SOFCs is subject to some more requirements beyond the obvious one of high ionic conductivity.

- not allow any electronic current (i.e. practically infinite electronic resistance)
- be impermeable to gas flows

- maintain inertness to the adjacent highly oxidizing and reducing environments of the electrodes

In this way, the ideal candidate materials lie within the family of stable, oxygen ion or proton conducting ceramics.

Solid solutions of divalent or trivalent metals such as CaO, Y_2O_3, and Sc_2O_3 with oxides of quarter valent metals such as zirconia or ceria are crystallized in the fluorite structure. The fluorite structure is face-centered cubic with the anions on the edges of the tetrahedron resulting in a very stable structure. The lower valent of the dopant with respect to the substituted cation results in the creation of the many vacancies through which oxygen ionic transfer is realized. More specifically, interaction of one mole of yttria with one mole of zirconia, results in zirconium having a 4+ oxidation state being substituted by yttrium which has a 3+ oxidation state, assigning thus a negative effective charge to the particular site. Compensation of the cation substitution is achieved through the creation of an ionic, i.e. oxygen in this case, vacancy, with an effective minus two charge being assigned to the particular site. Since the principles of electro-neutrality and mass site balance have to hold for every mole of yttria added to zirconia two moles of cation substitution are formed and one mole of oxygen vacancy. This mechanism of oxygen vacancies creation through doping enhances severely the conductivity with respect to the pure ZrO_2. Higher levels of metal oxide doping, result in higher bulk conductivity of YSZ. Defining the optimum percentage of doping depends on several factors (e.g. impurities, atomistic size and other properties and energetics). The 8% in yttria is in general believed to balance the electrostatic interactions between zirconia defects and oxygen vacancies. The first dominate if $> 8\%$ and then oxygen transport is hindered, while for $< 8\%$ again the imbalance results in lower ionic conductivity. The ionic radius of the anion (oxygen) being smaller than the corresponding one of the cation explains why the ionic diffusion is much higher for oxygen than for the involved cations, e.g. $Zr + 4$, $Y + 3$.

Zirconia, is known to form three crystallographic structures, monoclinic, tetragonal and cubic. The monoclinic is stable from room temperature up to $1170C^{\circ}$, the tetragonal is stable up to $2370C^{\circ}$ while the cubic one is stable above this limit until the melting point is reached ($2680C^{\circ}$). These phase transitions are subjected to noticeable volume changes and although reversible, result in material failure during cool-down. Zirconia doping with another lower-valent cation is a usual technique in order to alleviate the phase instability in ambient temperature and create a stable ceramic. Apart from YSZ, other materials have also been investigated as suitable for electrolyte materials with noticeable performance like SSZ and particularly Ceria.

1.2.2 Anode

The anode of an SOFC is that particular component where the electrochemical oxidation of hydrogen to protons takes place while in the same time these produced protons meet and interact on the TPBs with the oxygen ions coming from the cathode through the electrolyte producing water vapor and electrons according to 1.1.

$$2H_2 + 2O^{2-} \longrightarrow 2H_2O + 4e^- \tag{1.1}$$

Besides this primary operation, anode is also responsible for giving passage to the gas fuel and also access to the electrical species (ions and electrons) to reach the reaction sites 1.3. In order to fulfill these requirements the material which anode is composed of is subjected to the following requirements:

- chemical stability in oxidizing environment.
- catalytic activity for hydrogen oxidation.
- high electronic conductivity.
- high ionic conductivity.
- chemical and physical compatibility with surrounding components.
- mechanical and thermal compatibility with surroundings.
- porosity for high diffusion of the fuel (fig. 1.3, 1.2)
- hindrance of non-desirable reactions, e.g. pyrolysis.

The fuel is being humidified by vapor which is known to lower the anode overpotential, assist the completion of the water-gas shift reaction and clean carbon depositions on the electrode's interface.

Stability and compatibility of the anode refers to a series of not favorable conditions that the anode material has to undergo such as chemical reactions and dimensional/phase changes, resulting from interactions with other SOFC components, the highly reducing atmosphere, the corrosive effect of water vapor produced and/or the average to high operating temperatures.

Providing access to the reaction sites (TPBs) for oxygen ions is performed through a suitable phase while another phase is necessary to offer the way out to electrons to make it to the interconnect posts. The absence of any ceramic materials among the known Mixed Ionic-Electronic Conductors (MIEC) exhibiting simultaneously very high electronic and high ionic conductivity, dictates the use of two different phases so as to perform each task separately, in a percolated network however. In order to perform its proper electrochemical functions, the

anode must be able to transport oxygen ions to the active oxidation sites as well as product electrons away from the active sites.

Metals are known for catalyzing the anode reaction. Among them, Ni is low cost and with good chemical stability. Hence it has been traditionally considered as the metallic phase in the ceramic-metallic compound (cermet). If a ceramic phase such as YSZ is used, emanating basically from the need for good ionic conduction properties, we come up with a material that does not favor Ni agglomeration, diminishes the anode CTE (compared to the pure Ni one), and enhances the mechanical attachment of the anode to the electrolyte.

Typically the cermet production comes from powders of YSZ and NiO which are being mixed and sintered together at temperatures $1300C^{\circ} - 1400C^{\circ}$. After the addition of the electrolyte and the cathode, the cell is being exposed to inert atmosphere until the steady state operating temperature and the NiO is being reduced to Ni by a H_2 current, resulting in Ni to YSZ analogy of $45 - 55\%$. In this way, the highly porous percolated networks of metallic and ceramic phases extend from the electrolyte layer all the way to the anode/interconnect interface.

The amount of Ni proves to be a very important parameter affecting the electrical conductivity of the cermet and its overpotential. The optimum percentage is $40 - 45\%$ vol. of Ni. The electrochemical properties of the anode are further affected by the production method which controls the electrode's micro-structure. Finally, it has been reported that increasing the sintering temperature proves also to be beneficial for the electrochemical efficiency of the anode.

Major factors affecting the anode's degradation are:

- Volume increase of Ni during operation. Ni reoxidation to NiO takes place if oxygen passes in the fueling line. Re-fueling or reducing the anode does not however return the anode in its former state. This re-oxidation results in 70% volume increase of the metallic phase and in total $3 - 9\%$ volume increase of the whole electrode.

- Carbon uptake coming from a hydrocarbon fuel.

- Sulfur poisoning (short and long term).

Dealing with some of the factors leading to anode degradation has served as inspiration in devising alternative materials for SOFC anodes. Particularly favorable seems to be the use of Gadolinium Doped Ceria (GDC) in terms of both resistance to carbon poisoning and increase of electrochemical performance in general, while different perovskites have been proposed as solutions to sulfur poisoning.

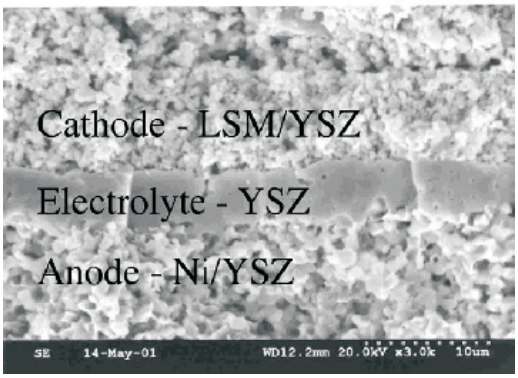

Figure 1.6: Cross-sectional SEM image of a typical SOFC, [4]

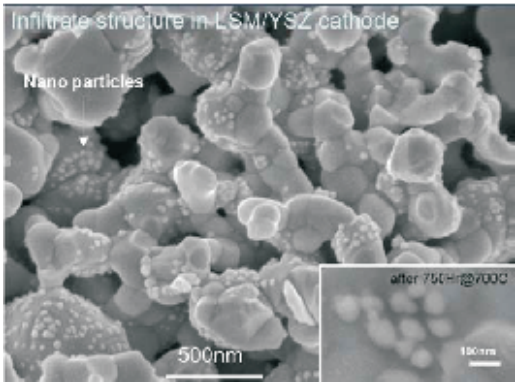

Figure 1.7: SEM image of infiltrated cathode, [4]

1.2.3 Cathode

The dual purpose of the cathode (fig. **??**) in SOFCs consists in the first place of the electrochemical reduction of oxygen f O_2 to O_{2-} as shown in Reaction 1.2.

$$O_2 + 4e- \longrightarrow 2O^{2-} \tag{1.2}$$

Secondly the cathode is responsible for facilitating air i.e. oxygen to reach reduction sites and then the produced oxygen ions to reach the electrolyte. The material requirements for a SOFC cathode can be summarized as follows:

- Catalytically active to oxygen reduction.
- Chemically and mechanically stable.
- High ionic conductivity.
- Thermal and mechanical compatibility with surroundings (thermal expansion coefficient (TEC), mechanical properties).
- High electronic conductivity.

Originally Pt was used as cathode material because of its well known catalytic impact on oxygen reduction, but gradually other materials like perovskites have gained ground because of economic and higher electrochemical activity reasons.

Perovskites are compounds of the form ABO_3. One perovskite used typically for cathode material is the $LaMnO_3$. This particular material undergoes phase transitions which are believed to be due to the partial oxidation Mn3+ to Mn4+. More specifically, it appears orthorhombic structure at $25C^\circ$ and rhombohedric above $600C^\circ$. Hence, naturally, the transition temperatures depend severely on the levels of Mn3+ ions and the oxygen stoichiometry. Once again, increase in the pure $LaMnO_3$ electrochemical properties such as ionic conductivity can be

achieved through means of doping with lower-valent cations such Sr2+ or Ca3+. The general type of these doped perovskites is $La_{1-x}A_xMnO_{3\pm\delta}$, where A is the dopant. In the case at which the dopant is strontium (LSM), the increase in ionic conductivity from around $10S/cm$ at $700C^\circ$ for undoped material, can vary from many decades to several hundreds S/cm. Another advantage from using LSM as cathode, is the fact that it exhibits a CTE close to the one that the electrolyte from YSZ does. It is generally known, and has also been experimentally confirmed, that lowering the cathode's temperature lowers the ionic conductivity and retards the oxygen reduction reaction. As a result, targeting lower operation steady state temperature than the typical around $800C^\circ$, and in the same time preserving high cell efficiency, is attempted by addition of YSZ or GDC, or the fabrication of multi-layer cathodes LSM/LSC/GDC, or finally the addition of catalytically active ceria nano-particles.

Alternative material to LSM are rare earth perovskite oxides with Co (LSCF), and they include oxide mixture of $LaCoO_3$ and $LaFeO_3$ doped with Sr. These compounds exhibit their maximum conductivity, $1000S/cm$, around $600C^\circ$. A drawback of LSCF is the fact that it does not exhibit the desired stability in reducing environment and that its CTE is not so much compatible with the one of the rest of the cell.

To conclude this brief reference to cathode materials we cite the most significant reasons that lead to the cathode's degradation:

- Reaction of perovskites with YSZ
- Reaction of perovskites with interoconnect steels.

1.2.4 Interconnect

The interconnect is the part of the fuel cell that is the interface or connection of the fuel cell to the environment. Through the interconnect, the cell is constantly supplied with fuel in order to sustain a balanced uninterrupted flowrate of fuel to the reaction sites on the anode side. On the cathode side, it acts as a cooling branch, permitting to high amounts of a cheap gas containing oxygen, hence usually just air, to flush and carry away great amounts of the produced heat during all the electrochemical processes involved in the cell. One could think in this way the interconnect as the "mirror" image of the electrolyte. This is a valid picture because the interconnect makes sure not only that the ions do not cross but also separates the two gas streams. Furthermore, equally important is the fact that through the interconnect takes place the electronic conductance from and to the cell and the establishment of the power supply to the load connected to the cell. Hence, the performance of the interconnect is of ultimate importance for the overall performance of a cell. Summing up the requirements for a good interconnect material, we can say that these are:

- Chemical stability in very challenging reducing and oxidizing environments.
- High electronic conductivity.
- Practically zero ionic conductivity. Even the slightest conduction of ion would result in a shortcut and loss of power.
- A proper TCE, matching those of the other parts of the cell.
- Good mechanical stability. Along with the anode support it is the part of the cell that undertakes all the mechanical stresses.
- Low cost material.

For a planar SOFC, usually the interconnect is a system of ribs of parallel channels. They can be assembled in 2 ways giving rise to co-flow/opposite flow or cross flow between the airstream and the fuel stream. A characteristic design for an interconnect is depicted in fig.1.8. Two major categories can be considered

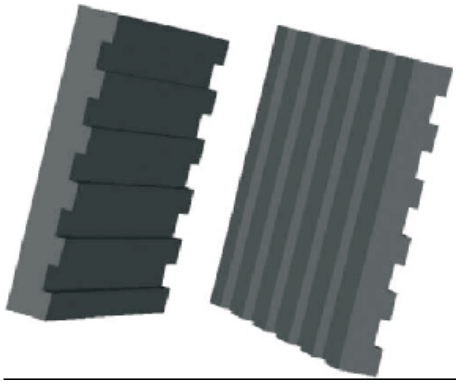

Figure 1.8: Schematic representation of an interconnect for a planar SOFC [3]

when the chemical composition of the interconnect is under discussion: ceramic and metallic interconnects. In any case the decisive factors are the application and the temperature range of operation. When we refer to the application this also includes the kind of fuel used as well as the chemical composition of the adjacent parts, i.e. the two electrodes.
The use of ceramic materials for the interconnect is almost compelling when examining high temperature SOFCs, in the range $900° - 1100°$. The metallic materials in this range would degrade very fast, because of phase transitions, creep and curie temperatures. In terms of fulfilling the requirements mentioned above, the ceramic materials have exhibited good behavior in oxidizing atmospheres but they tend to lose oxygen in reducing atmospheres. A common choice for a ceramic interconnect is $LaCrO_3$ which stable over a wide range of pressures

and its electronic conductivity can be increased by appropriate and careful doping, usually with Sr. A good match with the TCE of the MEA can also been accomplished through doping too. Major barrier however, in the use of ceramic materials so far has been their really high cost, mainly due to the high cost of the relevant manufacturing processes. The difference can be in the area of eight times larger than in the case of using a metallic interconnect at a lower temperature. It is indicative that for a ceramic interconnect the cost of this part alone can rise up to 90% of that of the whole cell [12].

The potential candidates along the metals for this part of the cell would lie between stainless compounds of Ni, Fe, Cr and the noble metals. The cost of the noble metals excludes them instantly from the selection process. Among the remaining candidates, Al is also excluded because the formation of Al_2O_3 lowers the electronic conductivity. The remaining options include austenitic and ferritic stainless steels whose CTE match the one of the other parts of the cell, in the order of $10.5 \cdot 10^{-6} K^{-1} - 12.5 \cdot 10^{-6} K^{-1}$. Among the various products developed in the industry for SOFC applications are the Ducralloy by Metalwerkee Plansee and the CroFer 22 APU by the collaboration of Julich and ThyssenKrupp [14]. The good properties achieved by the former are counter balanced by its forbidding cost while the performance of the later compound seems to be restricted by the increase in the Area Specific Resistance (ASR) of the Mn spinel layer and the volatility of Cr. The degradation of metallic interconnects can originate from corrosion due to the steam in the anode, from oxygen in the air stream, or from carbon and sulphur when dealing with hydrocarbons as fuels. For protection against these factors of loss of power, it is suggested that a proper protective coating layer should be applied.

Chapter 2

Theoretical Investigations

Two inter-affected factors are the principal ones for the manufacture of an ideal interconnect: the materials used and its actual design. Having discussed the choices of materials already, in what follows we focus our efforts in studying the design of a metallic interconnect with our final goal to make contributions in producing optimized interconnect designs and to offer insight in how its geometry can affect the performance of the cell in total. Our analysis intends to primarily study the main two aspects of the interconnect, i.e. the gas flow around it and the electronic conductance through it.

2.1 Fluid Flow

For a fluid flow analysis assuming that we are always referring to length scales at which the continuum hypothesis holds (i.e. one or two order of magnitudes greater that the nanoscale) the necessary theoretical tools are provided by properly expressing in general the major conservations laws for mass, momentum, angular momentum and energy. In what follows we only mention those notions that are necessary to our analysis, i.e. mainly mass, momentum and energy since they suffice for the scope of this work. The flow through-out the channel of an interconnect is a transport problem of a gas of spatially varying density. This happens 2.1 because as we go downstream the gas channel, the composition of the gas (for the shake of simplicity taken to be $H_2 - H_2O$ binary) changes, since hydrogen is being subtracted from the gas and diffuses to the reaction sites, and steam is being added, produced a few hundred microns below, into the membrane.

The differential form of mass balance, termed also as continuity equation, for a fluid flow of density ρ and velocity u_j:

$$\partial_t \rho + \partial_j(\rho u_j) = \omega \tag{2.1}$$

in the above ω is a generation of mass term accounting for source or sink, i.e. accounting for the generation or disappearance of mass as in the case of a reacting flow. In the case of steady, incompressible flow the above becomes:

$$\begin{aligned} u_j \partial_j \rho + \rho \partial_j u_j &= \omega \\ u_j \partial_j \rho &= \omega \end{aligned}$$

giving finally:

$$u_j \partial_j \rho = \omega \tag{2.2}$$

In the last equation we see how the spatial variation of density enters the continuity equation. At this point it is also useful in terms of what follows, to make absolutely clear what we refer to by the term incompressible fluid. By the notion of incompressibility we mean that the volume of a fluid element in the flow under study does not change at any point in space or time, i.e. there is no dilatation or other transformation to its shape (though it can of course, translate, rotate or become skewed). This fact is encapsulated in the mathematical definition of incompressibility [15] [16]:

$$\nabla \cdot \mathbf{u} = \partial_j u_j = 0 \tag{2.3}$$

In other words, incompressibility is not synonymous to preserving constant density only in terms of volume element changes, simply because the change can be due to spatial variations by thermal gradients or reactions taking place. The case of a flow in an interconnect is the case of such a reacting flow. Hence, for our study it is always true that $\partial_j u_j = 0$ but the density overall is or should be in principle treated as variable because of the change of the gas composition, unless we specifically study sub-cases where for the shake of simplicity or under other assumptions we are justified to neglect the density's spatial variation. The conditions under which a flow can produce such phenomena that distort the volume of a fundamental fluid element are met for example in the case of very fast supersonic flows and shock waves emerging flows, extensively studied in the context of aerodynamics and flows through turbine engines. For completion purposes, we add that the criterion for categorizing a flow as compressible is crossing the value 0.3 for the Mach number, the number that provides the ratio of the flow's velocity against the velocity of the speed of sound at the current temperature. The threshold of $Mach = 0.3$ has been set as such because it corresponds to an average change in density of 5% [15]. By an easy calculation, we find that the speed of sound at the operating temperature of our cell i.e. $T = 800°C$(assuming this also to be the temperature of our flow), given by:

$$U_{air} = \sqrt{\frac{\gamma RT}{M}} = 657,16\frac{m}{s} \tag{2.4}$$

R being the universal gas constant M the average molecular weight of air. In our case using a gas mixture with synthesis of $97.28\%H_2$ and $2.78\%H_2O$ giving an average molar mass of $2.4354 \cdot 10^{-3}\frac{kg}{mol}$ the speed of sound is even larger at the same temperature, i.e. $U_{inletgas} = 2.122 \cdot 10^3\frac{m}{s}$. Typical values of gas fuel velocities at SOFC fuel gas channels do not exceed $5\frac{m}{s}$, hence we conclude that the Mach number is practically 0 for our flow and we can safely rely on its incompressibility to hold throughout all of this study.

The force balance, or in Newtonian terms, balance of momentum rate, for viscous flow of a any fluid is fully described by the Navier-Stokes whose differential form in the most general case is given as:

$$(\partial_t(\rho u_i) + \partial_j u_i(\rho u_j)) = \partial_i \sigma_{ij} + \rho f_i \tag{2.5}$$

σ_{ij} is the total stress tensor and f_i is the sum of body forces on the fluid. The total stress tensor is

$$\sigma_{ij} = -p\delta_{ij} + \tau_{ij} \tag{2.6}$$

The viscous stress tensor for dynamic viscosity μ and secondary viscosity ζ is decomposed as follows:

$$\tau_{ij} = \mu(\partial_j u_i + \partial_i u_j - \frac{2}{3}\delta_{ij}\partial_k u_k) + \zeta\delta_{ij}\partial_k u_k \tag{2.7}$$

In the case of a newtonian incompressible fluid the viscous stress tensor is only dependent on the strain rate tensor $\partial_j u_i + \partial_i u_j$ i.e.

$$\tau_{ij} = \mu(\partial_j u_i + \partial_i u_j) \tag{2.8}$$

With the above assumptions the Navier-Stokes for a viscous, incompressible reacting flow with no external body forces, reads:

$$\partial_t(\rho u_i) + \partial_j u_i(\rho u_j) = -\partial_i P + \mu\partial_j^2 u_i \tag{2.9}$$

Expanding now the right hand side and using the definition of incompressibility and steadiness we get,

$$\begin{aligned}
\partial_t(\rho u_i) + \partial_j u_i(\rho u_j) &= u_i(\partial_t\rho) + \rho(\partial_t u_i) + \partial_j(u_i(\rho u_j)) \\
&= u_i(\partial_t\rho) + \rho(\partial_t u_i) + u_i\partial_j(\rho u_j) + \rho u_j\partial_j u_i \\
&= u_i\partial_j(\rho u_j) + \rho u_j\partial_j u_i \\
&= u_i\omega + \rho u_j\partial_j u_i \\
&= \rho u_i\partial_j u_j + u_i u_j\partial_j\rho + \rho u_j\partial_j u_i \\
&= u_i u_j\partial_j\rho + \rho u_j\partial_j u_i
\end{aligned}$$

So finally the Navier Stokes equation for a steady, viscous, incompressible reacting $2-d$ flow takes the form:

$$u_i u_j \partial_j \rho + \rho u_j \partial_j u_i = -\partial_i P + \mu \partial_j^2 u_i \tag{2.10}$$

We also cite the same equation for a steady, viscous, incompressible flow:

$$\rho u_j \partial_j u_i = -\partial_i P + \mu \partial_j^2 u_i \tag{2.11}$$

The inherent characteristics and major physical properties of any flow are elegantly captured by the Reynolds number defined as:

$$Re = \frac{UL\rho}{\mu} = \frac{UL}{\nu} \tag{2.12}$$

where in the above, L is the dominating length scale of the flow, U is the scale of the flow's velocity, μ is the dynamic viscosity and ν is the kinematic viscosity of the liquid (single or multi-component). This definition, emanating from a direct ratio of the inertia versus the viscous forces in a fluid, describes precisely whether one of this two terms dominates. In the limit at which the Reynolds number is very small viscous forces are by far exceeding inertia ones ($Re < 1$), while in the other limit of viscous forces affecting almost not at all the flow, the Reynolds number takes immense values. Typical examples of flows exhibiting both these two so different flow regimes are the flow in a journal bearing with Re below 1 while the supersonic flight of an aircraft in the order of $Re = 10^6$.

A crucial aspect of our simulations is the dimensionality of our study. For the shake of computational power needed and in order to be able to approach the subject from a theoretical-analytical point of view as well, we chose as appropriate to conduct our research in two dimensions. One of the challenges of this work was in general to take special care so that this reduction in dimensions not to affect the range of our conclusions and to still adequately describe in all cases, what is generally admitted to be, a 3-dimensional problem.

As such, we refer to the changes necessary to the above cited expressions of the Reynolds number in order to include the strong effect of the narrow slit, i.e. the gas channel's height. It turns out from lubrication theory [16],[17],[18], that the severe damping imposed by the ceiling and the floor walls for the full three dimensional flow can be adequately incorporated in a two dimensional version of the Navier-Stokes by the addition of a damping term, proportional to the 2D fluid velocity. The constant of proportionality, α is inversely depending on the square of the channel's height.

$$\alpha = \frac{12\mu}{h^2} \tag{2.13}$$

So the version of the Navier-Stokes that we use is:

$$u_i u_j \partial_j \rho + \rho u_j \partial_j u_i = -\partial_i P + \mu \partial_j^2 u_i - \alpha u_i \tag{2.14}$$

It is important to realize in which regime our flow lies, by calculating an approximate Re, so as to devise the right strategy for our analysis. The determination of an average dynamic viscosity and density is done by assuming an inlet gas composition of weight fractions, $w_{H_2} = 0.8, w_{H_2} = 0.2$ from the paper [19] and by calculating an average value according to the expressions supplied by [18]. With substitution we find, $\mu = 6.410^{-5} Pa \cdot s, \rho = 0.0278 \frac{kg}{m^3}$. The average velocity of flows for SOFC anodes in experimental settings are of the order of $2 \frac{m}{s}$, (or refer to calculations under constant dP e.g. $100 Pa$ giving a $Re = 0.12$). For an interconnect channel with dimensions $L = 4cm(length), w = 4cm(width), h = 0.35mm(height)$ the Reynolds number of open channel is below 1 , considering the height h as the characteristic length scale of the problem. This conclusion is very important because it means that for many choices of the design parameters we can neglect the inertia terms in our study without any severe loss either from a qualitative or quantitative perspective. Considering for some part of our work the flow as Stokes flow, will considerably facilitate a theoretical analysis since dropping the inertia terms leaves behind only linear terms in the Navier-Stokes equation which can be integrated and solved for certain 'regular' geometries. As a concluding remark in this section, we state beforehand that working with in general small Reynolds numbers is a choice also dictated by the method of Topology Optimization since in this regime a problem with the viscous dissipation as objective function is proven to be well posed [20]

The point of initiation to derive some analytical insight is to consider the case of one pilar of cylindrical current collector material in the cross flow of the gas. Pictorially this is described in figure 2.1

So now we face the problem of solving the equations of creeping flow for a cylinder in a flow of given gas composition. The relevant Navier Stokes free of inertia terms now reads:

$$\partial_i P = \mu \partial_j^2 u_i - \alpha u_i \tag{2.15}$$

The problem of creeping or Stokes flow, around a sphere and a cylinder is extremely well studied in fluid mechanics and hydrodynamics (references [17], [21], [22], [23], [24]. Here we present in a condensed way the few steps necessary to solve for the velocity field of the Stokes flow. The first step is to take the curl of eq. 2.15, producing:

$$0 = \mu \partial_j^2 \chi_j - \alpha \chi_i \tag{2.16}$$

Since this is a two dimensional flow, a stream function can be defined for this flow. By definition, a stream function is tangent to the velocity vector, i.e.

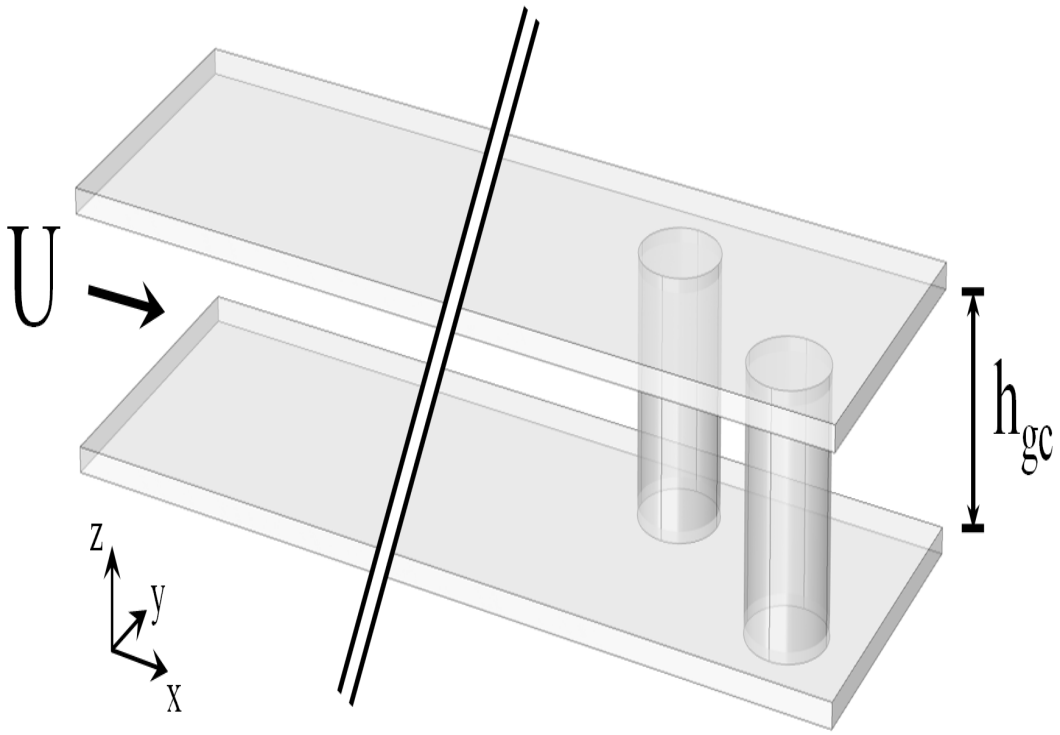

Figure 2.1: 3d geometry of the gas channel. Inflow gas velocity U

$u_i \partial_i \Psi = 0$. Furthermore the velocity field can be represented in general for such a flow as the curl of the vector potential which is the stream function in vector form. For the cylindrical case the vector potential is $\mathbf{B} = [0\ 0\ \Psi]$ in r, θ and z. So we can write:

$$u_i = \epsilon_{ijk} \partial_j B_k \tag{2.17}$$

where ε_{ijk} the Levi-Civita permutation tensor. Taking the curl of eq. 2.17 and keeping in mind the definition of the vorticity we get the expression that relates the vorticity to the stream function.

$$-\chi_i = \partial_j{}^2 B_i \tag{2.18}$$

In the 2-d case with not including the extra damping term in eq. 2.16 or in the general 3-d case, substitution of eq. 2.18 would result in having to solve the biharmonic equation $\nabla^4 \Psi = 0$, accompanied by the suitable boundary conditions. By doing so, as it is proven in [25], [26], [27], there is an acceptable solution that can match the flow around the sphere to the far field flow. This is not the case however in two dimensions and especially about a cylinder whose case is problematic. As we will vigorously demonstrate, for the cylinder case there can

be achieved no such matching no matter what choice we make regarding the constants emerging from solving our equations. The mathematical proof of this lack of solution, relies in a perturbation expansion of the solution on the Re number. Literature work on this topic is found in [28] and [29] for instance but we refrain from expanding on it significantly since it is not our primary objective.

The theoretical inability to solve to the pure Stokes problem for a cylinder had led the scientists at the beginning of the previous century to consider the creeping flow around a cylinder as one that cannot be achieved by nature. To the rescue came Oseen in 1910 presenting a proposal of not dropping the inertia term entirely but keeping a linearized form of it, i.e $\mathbf{U}\nabla\mathbf{u}$ where $\mathbf{U}$ is the far field velocity that needs to be matched and $\mathbf{u}$ is the "near" the sphere velocity. This idea was reasoned on the basis of scaling arguments showing inertia terms dominating in the region far from the perturbation of the flow imposed by the presence of the cylindrical structure. Oseen furthermore predicted an even better estimate for the drag around such a cylinder than the one coming form the sphere analysis, when compared to the experimentally acquired values. Lamb (1911) picked up from Oseen and many researchers ever since have contributed in studying this mathematical problem. Theoretical work was done by Faxen, Godstein [23] and Tomotika [24], providing exact analytical solutions for the velocity field and estimates on the drag force.

Returning to eq.2.16, as we will soon see, the addition of the viscosity term actually resolves the issue, and a matching with the far field velocity can be achieved naturally and without the need of similar to Oseen's ideas. In fact, we propose that this can be a universal treatment of similar problems, under a certain scaling condition.

Moving along, our goal is to formulate the relative modified biharmonic/shifted equation. As a first step we present the velocity and vorticity fields. In all the analysis that follows we refer to cylindrical-polar coordinates.

$$u_r = \frac{1}{r}\frac{\partial \Psi}{\partial \theta} \tag{2.19}$$

$$u_\theta = -\frac{\partial \Psi}{\partial r} \tag{2.20}$$

$$-\chi_z = \frac{\partial^2 \Psi}{\partial r^2} + \frac{1}{r}\frac{\partial \Psi}{\partial r} + \frac{1}{r^2}\frac{\partial^2 \Psi}{\partial \theta^2} \tag{2.21}$$

Taking the Laplacian of χ_z as:

$$\nabla^2 \chi_z = \frac{1}{r}\partial_r(r\partial_r \chi_z) + \frac{1}{r^2}{\partial_\theta}^2 + {\partial_z}^2 \tag{2.22}$$

By doing the appropriate substitution and performing the successive differentiations presented in the Appendix, we finally get the following expression for $\nabla^2\chi_z = L^2\Psi$:

$$\nabla^2\chi_z = -\partial^4_{r^4} - \frac{2}{r}\partial^3_{r^3}\Psi + \frac{2}{r^3}\partial^3_{\theta^2 r}\Psi - \frac{2}{r^2}\partial^4_{r^2\theta^2} - \frac{1}{r^3}\partial_r\Psi + \frac{1}{r^2}\partial^2_{r^2} - \frac{4}{r^4}\partial^2_{\theta^2}\Psi - \frac{1}{r^4}\partial^4_{\theta^4}\Psi \tag{2.23}$$

Taking a look at the boundary conditions required to be fulfilled, these are that both the r and θ components of the velocity be zero on the cylinder's boundary, which we assume to be of radius R, and very far from the body to acquire the freestream velocity U. Translated into equations for the stream function we have the following:

$$\Psi(R,\theta) = 0 \tag{2.24}$$

$$\frac{\Psi(R,\theta)}{\partial r} = 0 \tag{2.25}$$

$$\Psi(r\to\infty,\theta) = Ursin(\theta) \tag{2.26}$$

From eq. 2.26 we get the inspiration to look for the stream function solutions of the form

$$\Psi(r,\theta) = f(r)\cdot sin(\theta) \tag{2.27}$$

Taking into account eq. 2.27,eq. 2.23,eq. 2.21 and substituting into eq. 2.16 gives an ordinary differential equation for the function f which encompasses the spatial variation of the Ψ.

$$-\mu f'''' - \frac{2\mu}{r}f''' + \left(\frac{3\mu}{r^2}+\alpha\right)f'' + \left(-\frac{3\mu}{r^3}+\frac{\alpha}{r}\right)f' + \left(\frac{3\mu}{r^4}-\frac{\alpha}{r^2}\right)f = 0 \tag{2.28}$$

In the above, we notice that the terms multiplied with the mere viscosity, originate from the differentiation of Ψ in χ_z^2. The terms originating from the χ_z term are naturally of lower order, so they contribute up to the second order.

At this point, we make a slight pause in the solution process to demonstrate what the problem is in the 2d case of the cylinder as discussed above. In this way we can easier introduce the solution procedure and we can easily draw the conclusion that inclusion of the damping term has substantially benefited the existence of a solution for our case.

If in eq. 2.28 we take away all the terms involving α we get an equation which corresponds to the biharmonic $\nabla^4\Psi = 0$.

$$-f'''' - \frac{2\mu}{r}f''' + \left(\frac{3}{r^2}\right)f'' + \left(-\frac{3}{r^3}\right)f' + \left(\frac{3}{r^4}\right)f = 0 \tag{2.29}$$

As it is suggested by the form of f in eq.2.29 we are looking for solutions of the form $f = ar^n$. Substitution in eq.2.29 reveals the following algebraic equation:

$$-an(n-1)(n-2)(n-3)r^{n-4} - \frac{2}{r}an(n-1)(n-2)r^{n-3} + \frac{3}{r^2}an(n-1)r^{n-2} - \frac{3}{r^3}anr^{n-1} + \frac{3}{r^4}ar^n = 0$$
$$ar^{n-4}(-n(n-1)(n-2)(n-3) - 2n(n-1)(n-2) + 3n(n-1) - 3n + 3) = 0$$

The roots of the expression in the parenthesis are $3, 1, 1$ (double)and -1. This suggests that f should take the form:

$$f(r) = Ar^3 + Brlnr + Cr + \frac{D}{r} \tag{2.30}$$

A,B,C and D are the constants that we need to define through fulfilment of the boundary conditions.

Lets first translate the boundary conditions given for Ψ to the relevant to f form.

$$f(R) = 0 \tag{2.31}$$

$$f'(R) = 0 \tag{2.32}$$

$$f(r \to \infty) = Ur \tag{2.33}$$

From eq.2.33 we immediately conclude that A and B must be set to zero. Using the other two condition on the boundary of the cylinder it is easy to calculate that they are identically zero as well. This is the mentioned above inability for this solution, known as Stokes solution, to adequately resolve the flow near the cylinder and satisfy in the same time the far field condition.

Closing this slight deviation from the solution of our actual problem, we state that we will implement the same reasoning as indicated above. For the solution of eq. 2.28 we assume a similar separation of variable since the same boundary condition at infinity has to be satisfied and use again the trial function ar^n for the function f. Substitution yields:

$$a\mu r^{n-4}(-n(n-1)(n-2)(n-3)-2n(n-1)(n-2)+3n(n-1)-3n+3)+a\alpha r^{n-2}(n(n-1)+n-1) = 0 \tag{2.34}$$

To go further we recall the definition of $\alpha = \frac{12\mu}{h^2}$. With a glance we observe that the last expression makes in this way sense dimensionally. On top of that we are able to solve eq. 2.34 by examining three different cases depending on the ratio of r/h.

- $r < \frac{h}{2\sqrt{3}}$. In this case the contribution to eq. 2.34 from the damping term becomes insignificant. Hence the solution is dominated by the contribution coming from the viscous term and the damping one can be dropped. This case corresponds directly to the case already examined for the pure viscous term balancing the pressure, and as we have seen does not accept a solution in closed form. In this case it is required that we revert to ideas similar to the one applied by Oseen or other later researchers.

- $r \sim \frac{h}{2\sqrt{3}}$. Both contributions are important and the solution must be sought by collecting all the alike terms together.

- $r > \frac{h}{2\sqrt{3}}$. In this case we can depend only on the term originating form the damping, for the solution and neglect the viscous part of eq. 2.34.

From the above analysis, it is obvious that as long as we choose the radius of our study greater or equal to an order of magnitude less than our channel's height, we can hopefully escape from the pitfalls of the mere viscous flow around a cylinder. We proceed by analyzing all the above cases separately.

2.1.1 Case $r < \frac{h}{2\sqrt{3}}$

In what follows we briefly present the solution obtained in the relevant literature. It was found convenient to define some new quantities. These are $k = \frac{U}{2\nu}$ and $\xi = kr$. If by definition the Re is $Re = \frac{UD}{\nu}$ then $\xi = \frac{1}{4Re}$. Proudman [28] proposes the use of an approximation for the stream function, normalized by $(U \cdot R)$, of the flow originally suggested by Lamb:

$$\psi = \left(r + \frac{1}{2B_o r}\right) sin\theta - \sum_{n=1}^{\infty} \frac{1}{2B_0} \phi_n \left(\frac{1}{2} Rer\right) \frac{rsinn\theta}{n} + O(B_0^{-2}) \tag{2.35}$$

where in 2.35 $B_o = \frac{1}{2} - \gamma_0 - ln(\xi)$ and $\phi(n) = 4K_1 I_n + 2K_0(I_{n+1} + I_{n-1})$, K and I being the modified Bessel functions and γ_0 the Euler-Mascheroni constant which up to 5 digit reads 0.57721. Let us also note that in eq.2.35 the used radius r is also normalized with the cylinder's radius R.

This approximation is sufficient since the accuracy sought from any analytical solution cannot exceed the order of magnitude of the dropped inertia terms.

However, ignoring such considerations, Tomotica et al. in [24] have provided such analytical solutions.

$$\psi = U\left(r - \frac{R^2}{r}\right) sin\theta + \frac{1}{4} \sum_{m=0}^{\infty} \sum_{n=1}^{\infty} B_m \left(\left(\frac{R}{r}\right)^{n+1} \Phi_{m,n}(\xi_0) - \Phi_{m,n}(kr)\right) \frac{rsinn\theta}{n} \tag{2.36}$$

In eq. 2.36 $\xi_0 = kR = \frac{1}{4Re}$, and the coefficients $B'_m s$ are determined through the following expression.

$$\sum_{m=0}^{\infty} B_m \lambda_{m,n}(\xi_0) \quad = \quad \begin{cases} 4 & n = 1 \\ 0 & n = 2, n = 3 \end{cases} \tag{2.37}$$

where, $\lambda_{m,n}(\xi_0) = I_{m-n}(\xi_0)K_{m-1}(\xi_0)+I_{m+n}(\xi_0)K_{m+1}(\xi_0)+I_{m-n+1}(\xi_0)K_m(\xi_0)+I_{m+n-1}(\xi_0)K_m(\xi_0)$

For sufficiently small Reynolds numbers however and taking into account that flow is non-symmetric in the vertical to the flow direction, leading to cancellation of the double series terms in 2.36 corresponding to $m = 0, n = 1, 2$, there has also been proposed an approximation for the normalized stream function as function of the normalized distance, the angle and the Reynolds number that we deem sufficient for the purposes of our analysis.

$$\psi = (A(r_1 - \frac{1}{r_1}) - Br_1 ln(r_1))sin\theta + (F(r_1^2 - \frac{1}{r_1^2}) - Gr_1^2 lnr_1)sin2\theta \tag{2.38}$$

the constants A,B,C and D are all functions of the Reynolds number. More specifically, $A = \frac{B}{2} = \frac{1}{2(lnRe-2.02223)}$, $F = \frac{Re}{16}$, $G = -BC$.

With eq. 2.38 at our disposal we can calculate the velocity components:

$$u_r = \frac{-cos\theta \left(ArR(-r^2 + R^2) + Br^3 Rln(\frac{r}{R}) + (2F(-r^4 + R^4) + 2Gr^4 ln(\frac{r}{R})sin\theta)\right)}{r^3 R} \tag{2.39}$$

$$u_\theta = \frac{sin\theta \left(rR(Br^2 - A(r^2 + R^2)) + Br^2 ln(\frac{r}{R}) + (Gr^4 - 2F(r^4 + R^4) + 2Gr^4 ln(\frac{r}{R}))sin\theta\right)}{r^3 R} \tag{2.40}$$

Knowing the velocity field we can now calculate the viscous dissipation. This expression originating from straight-forward differentiations of the above velocity components by the definition eq.2.54 is at our disposal as well. The drag force on the cylinder per unit depth in the z axis is found to be:

$$F_D = 2\pi\mu U \sum_{m=0}^{\infty} B_m \tag{2.41}$$

Keeping the first term from the above sum, we get the Bairstow approximation:

$$F_D = \frac{4\pi\mu U}{I_0(kR)K_0(kR) + I_1(kR)K_1(kR)} \tag{2.42}$$

By recognizing B_0 as the denominator of the last equation, we get the well known Lamb approximation for the drag:

$$F_D = \frac{4\pi\mu U h}{\frac{1}{2} - \gamma_0 - ln(\frac{kR}{2})} \tag{2.43}$$

2.1.2 Case $r \sim \frac{h}{2\sqrt{3}}$

In this case we perform the substitution $h^2 = 12r^2$ and by factorization and combining alike terms we get:

$$\begin{aligned} -n(n-1)(n-2)(n-3) - 2n(n-1)(n-2) + 4n(n-1) - 2n + 2 = 0 \\ (n-1)\cdot(-n(n-2)(n-3) - 2n(n-2) + 4n - 2) = 0 \\ (n-1)\cdot((-n^2+2n)(n-3) - 2n^2 + 4n + 4n - 2) = 0 \\ (n-1)\cdot(-n^3 + 3n^2 + 2n - 2) = 0 \\ (n-1)\cdot(n+1)\cdot(n-3.414213562373094)\cdot(n-0.585786437626905) = 0 \end{aligned}$$

In other words the roots of the algebraic expression, are not imaginary and more specifically are $3.414213562373094, 1, 0.585786437626905$ and -1, in descending order. To an accuracy of $\frac{2}{1000}$ we substitute the decimals with the fractions, $3.414213562373094 \rightarrow \frac{41}{12}$ and $0.585786437626905 = \frac{10}{17}$. Hence we rewrite:

$$(n-1)\cdot(n+1)\cdot(n-\frac{41}{12})\cdot(n-\frac{10}{17}) = 0 \tag{2.44}$$

As a result we can now state that the spatial variation of the stream function adopts the form:

$$f(r) = Ar^{\frac{41}{12}} + Br + Cr^{\frac{10}{17}} + \frac{D}{r} \tag{2.45}$$

We now apply the boundary equations eq.2.31-2.33. More specifically from eq.2.33 we conclude that $A = 0$ and B has to be identically equal to U, $B = U$. Solving the simple two by two system for C and D from application of the boundary on the perimeter of the cylinder of radius R, we get, $C = -\frac{34}{27}UR^{\frac{7}{17}}$ and $D = \frac{7}{27}UR^2$. Thus we rewrite f as,

$$f(r) = Ur - \frac{34}{27}UR^{\frac{7}{17}}r^{\frac{10}{17}} + \frac{7}{27}\frac{UR^2}{r} \tag{2.46}$$

Now we can also give the exact form of the stream function as:

$$\Psi = f(r)sin\theta = (Ur - \frac{34}{27}UR^{\frac{7}{17}}r^{\frac{10}{17}} + \frac{7}{27}\frac{UR^2}{r})sin\theta \tag{2.47}$$

Combining eq. 2.47 with eq.2.19 and with eq.2.20 we get:

$$u_r = \left(U - \frac{34U}{27} \left(\frac{R}{r} \right)^{\frac{7}{17}} + \frac{7U}{27} \left(\frac{R}{r} \right)^2 \right) cos\theta \tag{2.48}$$

$$u_\theta = \left(-U + \frac{20U}{27} \left(\frac{R}{r} \right)^{\frac{7}{17}} + \frac{7U}{27} \left(\frac{R}{r} \right)^2 \right) sin\theta \tag{2.49}$$

At this point we also note that the above calculated velocity field satisfies the incompressibility assumption of $\nabla \cdot \mathbf{u} = 0$. With this notice we can safely return to the Navier-Stokes eq.2.15 and after inserting the acquired for the velocity expressions we can integrate to gain the pressure. Having the pressure will then allow us to compute the drag force on the body and the drag coefficient. We find:

$$p = \left(\frac{1}{r} - \frac{239R^{\frac{7}{17}}}{162r^{\frac{24}{17}}} + \frac{7R^2}{81r^3} \right) U\mu cos\theta \tag{2.50}$$

The normal and shear stress components are given respectively by:

$$\sigma_{rr} = 2\mu \frac{\partial u_r}{\partial r} = \frac{28}{27} \left(\frac{R^{7/17}}{r^{24/17}} - \frac{R^2}{r^3} \right) U\mu cos\theta \tag{2.51}$$

$$\tau_{r\theta} = \mu \left[r \frac{\partial (u_\theta / r)}{\partial r} + \frac{1}{r} \frac{\partial u_r}{\partial \theta} \right] = \frac{14R^{7/17}(7r^{27/17} - 34R^{27/17})}{459r^3} U\mu sin\theta \tag{2.52}$$

The drag force now is given by integration of the projections of the pressure, normal and shear stresses in the direction of the flow, on the cylinder's surface multiplied with the channel's height, i.e:

$$F_D = h \int_0^{2\pi} (-pcos\theta + \sigma_{rr} cos\theta - \tau_{r\theta} sin\theta) R \, d\theta = \frac{371}{306} h\pi\mu U. \tag{2.53}$$

Finally we can deduce the viscous dissipation function for our flow.

$$\psi_D = \mu \left[2 \left[\left(\frac{\partial u_r}{\partial r} \right)^2 + \left(\frac{1}{r} \frac{\partial u_\theta}{\partial \theta} + \frac{u_r}{r} \right)^2 \right] + \left[r \frac{\partial}{\partial r} \left(\frac{u_\theta}{r} \right) + \frac{1}{r} \frac{\partial u_r}{\partial \theta} \right]^2 \right] \tag{2.54}$$

$$\psi_D = \frac{196}{289} \frac{U^2 \mu}{R^2} sin^2\theta \tag{2.55}$$

2.1.3 Case $r > \frac{h}{2\sqrt{3}}$

In this case we neglect the terms coming from $\nabla^2\mathbf{u}$ in the Navier-Stokes equation and hence by dropping the relevant terms not including α in eq. 2.34 the algebraic equation for the indices reads:

$$(n-1)(n+1) = 0 \Rightarrow n = \pm 1 \tag{2.56}$$

The meaning of the last result is that the sought spatial variation of Ψ is going to be of the form:

$$f(r) = A_1 r + \frac{B_1}{r} + C1 \tag{2.57}$$

and in combination with the boundary conditions used above eq. 2.31 - 2.33 it yields:

$$f(r) = Ur + \frac{UR^2}{r} - 2UR \tag{2.58}$$

Finally, the stream function is:

$$\Psi(r,\theta) = \left(Ur + \frac{UR^2}{r} - 2UR\right) sin\theta \tag{2.59}$$

the velocity profile now is:

$$u_r = Ucos\theta\left(1 - \frac{2R}{r} + \frac{R^2}{r^2}\right) \tag{2.60}$$

$$u_\theta = -Usin\theta\left(1 - \frac{R^2}{r^2}\right) \tag{2.61}$$

Integration of the Navier-Stokes from $\frac{h}{2\sqrt{3}}$ reveals the pressure field according to:

$$P(r,\theta) = -\frac{2U\mu cos(\theta)}{rh^3}\left(\sqrt{3}h^2 r(1-2\sqrt{3}) + 6R^2(h-2\sqrt{3}r) + 6hrRln\frac{12r^2}{h^2}\right) \tag{2.62}$$

An interim check of our theoretical derivations is that besides the velocity's divergence being zero, computation of the curl of pressure gradient for the derived formula gives zero, i.e. $\nabla \times \nabla P = 0$.
The new normal and shear stress components are given respectively by:

$$\sigma_{rr} = 2\mu\frac{\partial u_r}{\partial r} = 4U\mu cos\theta\frac{R}{r^2}\left(1 - \frac{R}{r}\right) \tag{2.63}$$

$$\tau_{r\theta} = \mu\left[r\frac{\partial(u_\theta/r)}{\partial r} + \frac{1}{r}\frac{\partial u_r}{\partial\theta}\right] = 2U\mu sin\theta\frac{R}{r^3}(r-2R) \tag{2.64}$$

As before, we are interested in the projections of the pressure and the normal and shear stresses in the far field's flow direction.

$$F_D = h\int_0^{2\pi}(-pcos\theta+\sigma_{rr}cos\theta-\tau_{r\theta}sin\theta)R\,d\theta = \frac{2\pi U\mu}{h^2}\left(h^3+\sqrt{3}R(h^2-12R^2)+6hR^2ln\frac{12R^2}{h^2}\right) \tag{2.65}$$

The viscous dissipation function (per unit length) now is given by:

$$\psi_D = \frac{4R^2U^2\mu}{r^6}(3r^2-8Rr+6R^2+(r^2-2R^2)cos(2\theta)) \tag{2.66}$$

Integration of the above expression for the height of the channel accounts for the total dissipation from the surface of the cylinder to an outer radius R_2. Assuming that R is greater than the height:

$$\Psi_D = h\int_R^{R_2}\int_0^{2\pi}\psi_D r d\theta dr = \frac{4\pi hU^2\mu}{3R_2^4}(-9R^4+16R^3R_2-9R^2R_2^2+2R_2^4) \tag{2.67}$$

If the radius of the cylinder is smaller than $h/\sqrt{12}$ then we need to add the dissipation for the viscous dissipation form the calculations for the inner part of the cell.

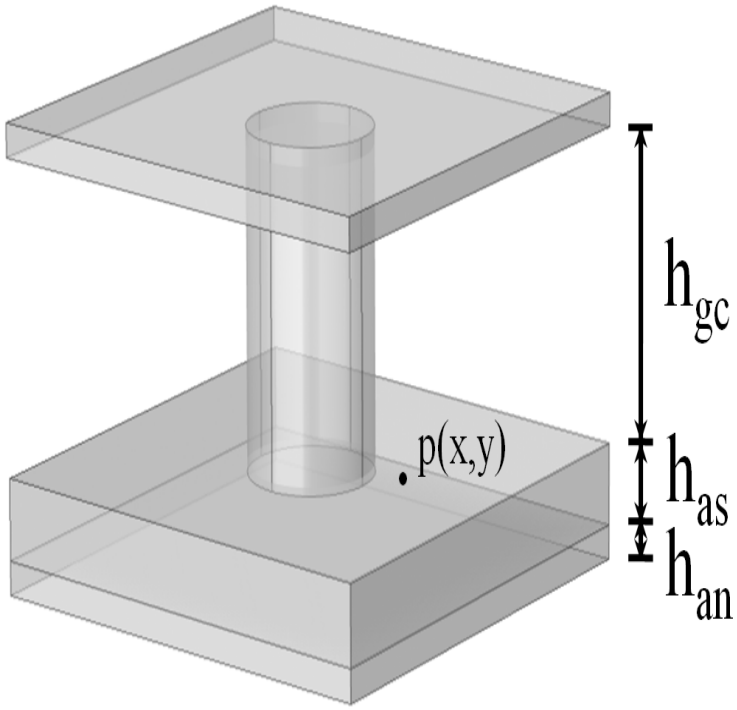

Figure 2.2: 3d geometry of the gas channel and the SOFC's anode and anode support layers below

2.2 Electrical Problem

The second major function of the interconnect is the electronic conduction between the cells electrodes and to the external circuit. The geometry to which we refer to is a half cell, with one end on the anode/electrolyte interface and the other on the far outer end of the current collector fig.2.2.

In the analysis to follow later on, regarding the potentials associated with the operation of the fuel cell and its losses exact connection between the current density and the electrode's overpotential will be provided. In this point we need to stress that the choice for a linear function instead of a Buttler-Volmer like equation, among other requirements, has to meet the assumption of overall linear Partial Differential Equations (PDEs) for the potential of different parts of the cell as it will become clear from this section.

The electrical conductivity problem in the current collector in three dimensions is described by a Laplace PDE [1]: for the potential Φ.

$$\sigma_{ic}\nabla^2\Phi_{ic} = 0 \tag{2.68}$$

Where in eq. 2.68 and hereafter the index "ic" stands for interconnect. The

boundary conditions for this problem is flux continuity through the interface between current collector and the electrode and a fixed potential on the other side, such that a current can be established and in the anode side a drain of electrons is being achieved while on the cathode side an electronic influx.

Since we are restricted for the purposes of our approach to two dimensions we need a two dimensional version of eq. 2.68. We claim that the accurate transition of the full three dimensional case to the two dimensional one is accomplished by the addition of a source term, corresponding to the drain of electrons, confining ourselves to the anode from now on, to the two dimensional Laplace equation. Determination of this extra term follows our physical intuition and understanding of the problem as well as scaling arguments. Assuming without loss of generality that the other than the current collector's/anode's interface of the current collector is grounded, the current that is being drawn is given by diving the potential difference of top and bottom with the relevant area specific resistance, which is $\frac{\sigma_{ic}}{h_{ic}}$. Hence the equation that we solve for in the areas where current collector material will appear in our domain is the following:

$$h_{ic}\sigma_{ic}\nabla^2\Phi_{ic} = \sigma_{ic}\frac{\Phi - V_0}{h_{ic}} \tag{2.69}$$

In eq. 2.69 as already noted $V_0 = 0$.

In a similar way, the three dimensional equation for the anode is a Poisson equation in the potential of the anode, with boundary conditions insulation at the interface with the electrolyte and all around and flux continuity on the interface with the anode support.

$$\sigma_{an}\nabla^2\Phi_{an} = Sa_{an}i_{ct} \tag{2.70}$$

and a Laplace for the anode support With boundary conditions influx and outflux of charge in the parallel to the current flow direction (z axis), electrical insulation on the periphery and potential connected to the grounded edge of the current collector.

$$\sigma_{as}\nabla^2\Phi_{as} = 0 \tag{2.71}$$

Another equivalent modeling strategy is also to treat the current generation as boundary influx in the anode's interface with the electrolyte. In eq. 2.70, i_{ct} is the charge transfer current accounting for the generation of electrons from the charge transfer reaction and Sa_{an} is a geometric parameter related to the path of the species involved in the reaction rendering the product $Sa_{an}i_{ct}$ the local volumetric current generation. While due to its definition, Sa_{an}'s units may vary, depending on whether the reaction is believed to be taking place at a triple phase boundary $(1/m^2)$ or at the surface of a Mixed Ionic Electronic Conductor $(1/m)$, overall the term $Sa_{an}i_{ct}$ has always units of current per volume.

The collapse of this fully 3 dimensional model in 2 dimensions cannot preserve all the information conveyed by the full picture and more specifically, we cannot distinguish between the 3 different potentials on the interfaces of the cell's layers entering our calculations. As imposed by our decision to study thus the problem in 2 dimensions comes the fact that we have to treat the anode and the anode support areas as a single lumped element. This approximation though unwanted and far from the truth in terms of conventional Ni/YSZ anodes and anode support materials, it is not too far though for other MIEC like for example CGO. From a mathematical point of view, this treatment can be accepted because of the linearity of eq.2.71 and eq.2.70 and the similarity of the electrical conductivities of the anode and anode support. An "addition" of the two equations is that possible leading to a single potential variable for the combined region. Now taking advantage of the transition from the volumetric current production to the current density i, locally for every point in the x-y plane in the anode, we can write $Sa_{an}i_{ct} = \frac{i}{h_{an}+h_{as}}$.

Combining these arguments we reach the following two dimensional analog of the governing equation in the lumped element:

$$(h_{an} + h_{as})\sigma_{an}\nabla^2\Phi_{an-as} = i \tag{2.72}$$

From now on we re-assign to the potential of the combined anode-anode support the symbol Φ_{ans}.

It is also interesting to note that eq.2.72 is in essence an implicit Helmholtz equation, because of the assumed linear dependence of the current density on the electrode's potential as it will be later explained. By a closer look in equation 2.72

Apart from the physical reasoning, we also provide quantitative proof for the validity of eq. 2.69. For the purposes of checking the adopted expressions, we can safely assume a constant generation of electrons throughout the cell. This assumption is valid only in this paragraph alone.

Out of need to link these results to the afore-presented fluid flow analysis, we choose an axially symmetric geometry for the current collector pillar and the anode-anode support layer below. In the simulations to follow, unless otherwise noted, we use the sets of parameters as given in the table 2.1.

Table 2.1: SOFC parameters

h_{ic}	h_{as}	h_{an}	σ_{ic}	σ_{an}	i_{ctan}
$350\mu m$	$300\mu m$	$20\mu m$	$10^4\frac{S}{m}$	$10^6\frac{S}{m}$	$10^4\frac{A}{m^2}$

In fig.2.3,2.4,2.5 we show a solution of the two dimensional model which includes all the reasoning developed so far. During the parametric runs we used

a fixed circular domain for the anode-anode support domain of $1cm$, outer diameter, and a varying r_{ic} from $1mm$ to $9mm$,inner circle depicted by a black line. The boundary conditions are flux and voltage continuity at the two areas interface and insulation on the outer diameter.

From these figures we are able to see at once that our 2D model accurately accounts in all cases for the grounded potential inside the interconnect pillar. The other two major checks that need to be made are to test the matching of the current through the different areas and their deviation from a full three model.

Very important for our analysis is also figure 2.6 which shows a cross section along any diameter, of the computational domain (because of its symmetry). It is evident that in the anode/anode support region the profile of the potential is a parabolic one, while in the interconnect it has another profile with a very saddle, compared to the outer region, decrease. From a first glance this profile looks like an exponential one and actually it can be fitted nicely using this law, but the analytical solution we achieve later in the context of this analysis will also reveal the exact mathematical formula for the potential in the inner domain. Returning to checking the vertical fluxes we find the relative errors by comparing the integral of the fluxes through the inner domain with the integral of the flux through the top boundary of an axisymmetric model, again for a parametric study of varying pillar radius. The potential distribution for a typical 3D case can be found in fig.2.7 and a direct comparison with fig.2.5 shows how well our model overall compares with a full model for which current generation takes place in part of the outer lower domain. Stressing this important fact by looking closer at the relative figures, we see that the achieved minimum values in the 2D model is $-0.0398V$ while in the 3D (the axisymmetric model is in every aspect a 3D model and we treat and refer to it as such), the minimum value is $-0.0388V$. Overall, the computed relative errors are in the range of $1-5\%$ for most part of the span of the parametric study and thus we deduce a good agreement between the two models. As another subtle assumption for our model comes the fact that because of the dimensionality of our analysis, we cannot account for current generation below the current collector pillars.

We now proceed in deriving an analytical solution for our model. for this derivation we refer to fig.2.8 and we name, for ease of writing the relevant equations, the combined anode-anode support as region 1 and the current collector area 2 assigning the corresponding index to all the magnitudes used. The major steps of the analysis are presented here. For the potential in area 1 the following PDE is true:

$$\sigma_1 \nabla^2 \Phi_1 = \sigma_1 \frac{1}{{h_1}^2} \Phi_1 \Rightarrow \nabla^2 \Phi_1 = c_1^2 \Phi_1 \tag{2.73}$$

where we have set:

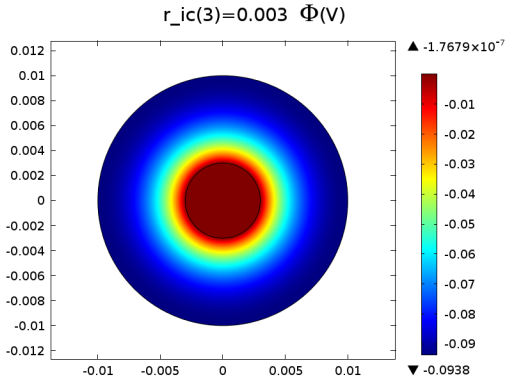

Figure 2.3: 2D solution for potential Φ. $r = 3 \cdot 10^{-3} m$

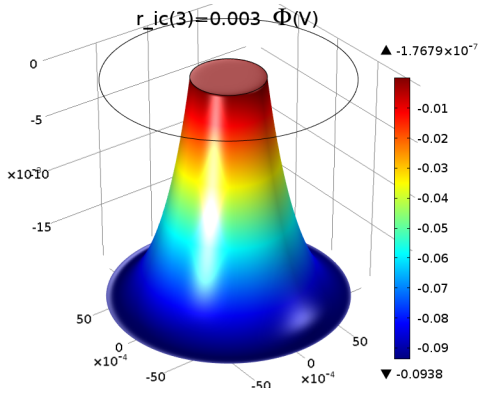

Figure 2.4: Height representation of 2D solution for potential Φ. $r = 310^{-3} m$

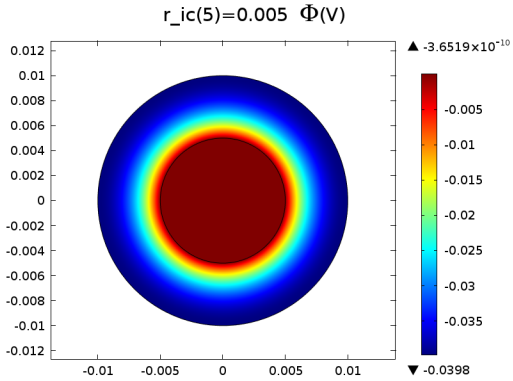

Figure 2.5: 2D solution for potential Φ. $r = 5 \cdot 10^{-3} m$

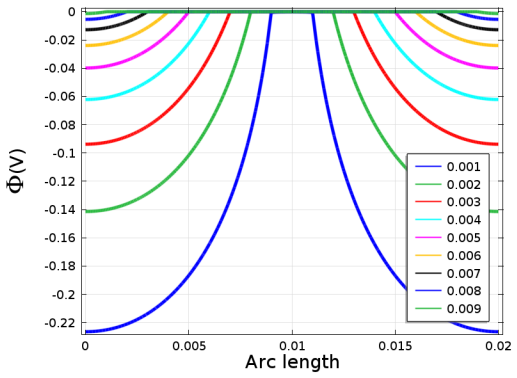

Figure 2.6: Cross section representation of potential Φ along a diameter

$$(c_1)^2 = \frac{1}{{h_1}^2} \tag{2.74}$$

Because of the axial symmetry,

$$\Phi_1(r, \theta) = \Phi_1(r) \tag{2.75}$$

And we get the bessel ODE:

$$\sigma_1 \nabla^2 \Phi_1 = \sigma_1 \frac{1}{h_1^2} \Phi_1 \tag{2.76}$$

$$\Phi_1'' + \frac{1}{r} \Phi_1' = {c_1}^2 \Phi_1 \tag{2.77}$$

$$r^2 \Phi_1'' + r \Phi_1' - r^2 {c_1}^2 \Phi_1 = 0 \tag{2.78}$$

With general solution

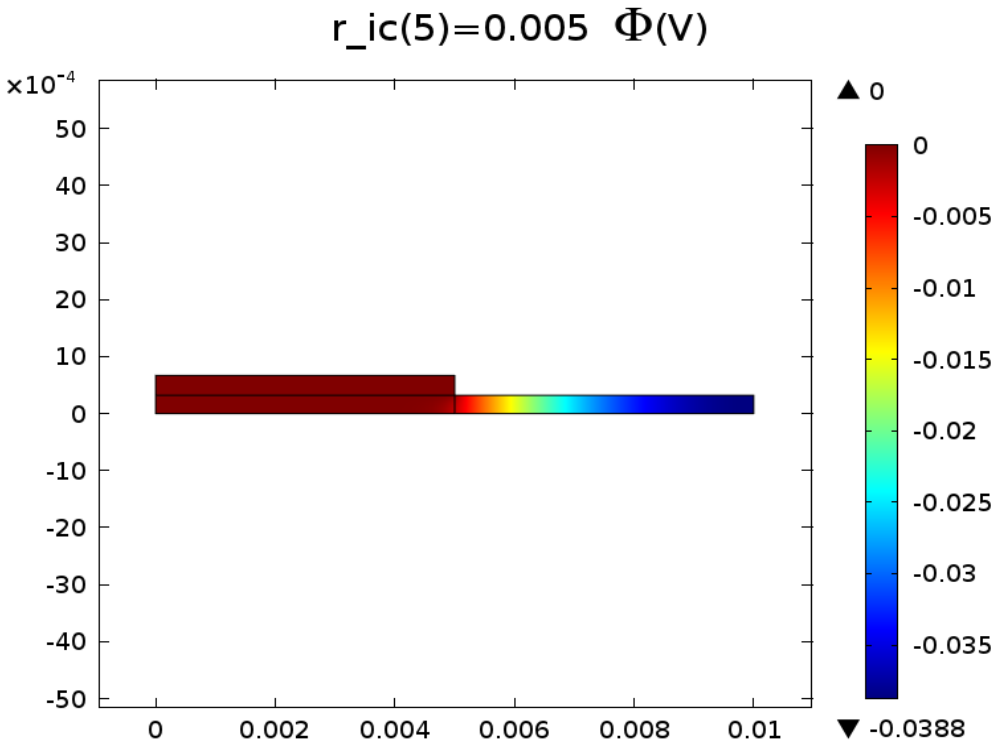

Figure 2.7: Axisymmetric electrical problem, $r = 5 \cdot 10^{-3} m$

$$\Phi_1 = A_1 J_n(0, ic_1 r) + A_2 Y_n(0, ic_1 r) \tag{2.79}$$

From the condition that the solution at the center needs to be bounded we conclude that $A_2 = 0$ Hence,

$$\Phi_1 = A_1 J_n(0, ic_1 r) \tag{2.80}$$

Turning to area 2 if we are given the vertical current density i,

$$\sigma_2 \nabla^2 \Phi_2 = \frac{i}{h_2} \Rightarrow \nabla^2 \Phi_2 = c_2^2 \tag{2.81}$$

where we set:

$$(c_2)^2 = \frac{i}{\sigma_2 h_2} \tag{2.82}$$

Given the axial symmetry of the problem,

$$\Phi_2(r, \theta) = \Phi_2(r) \tag{2.83}$$

We acquire the Euler ODE,

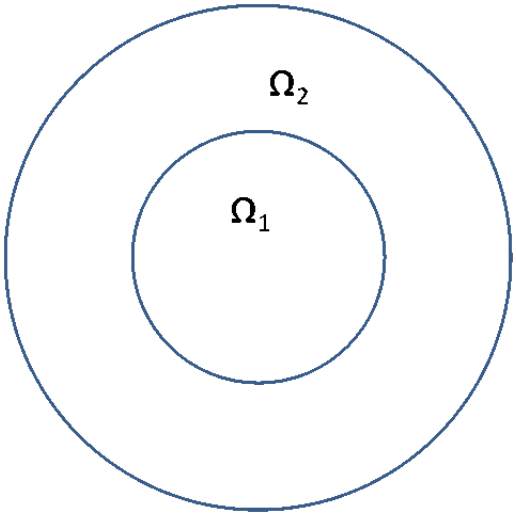

Figure 2.8: 2D model fixed geometry

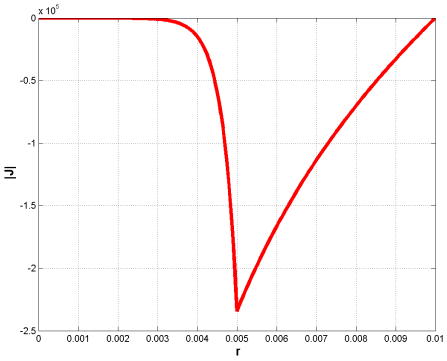

Figure 2.9: Total Flux for 2D fixed model

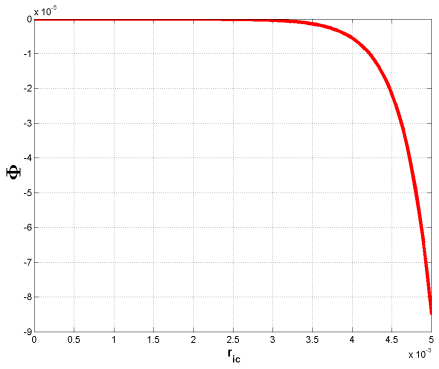

Figure 2.10: potential cross section inside the pillar, analytical solution

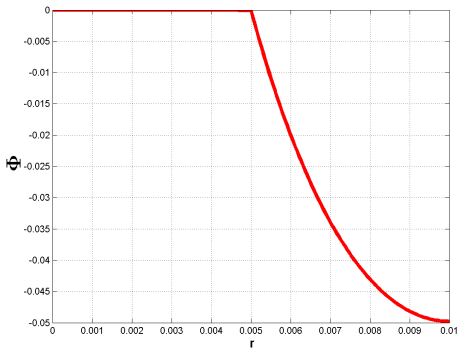

Figure 2.11: potential cross section for domains 1 and 2, analytical solution

$$\Phi_2'' + \frac{1}{r}\Phi_2' = {c_2}^2 \tag{2.84}$$

With general solution,

$$\Phi_2 = \frac{c_2^2 r^2}{4} + B_2 + B_1 lnr \tag{2.85}$$

The boundary conditions of our problem, given by the next three equations are respectively,flux and potential continuity at the interface, and zero flux at the outer boundary of area 1.

$$\vec{J}(r = r_2)\hat{n} = 0 \Rightarrow \nabla\Phi_2(r = r_2) = 0 \tag{2.86}$$

$$\Phi_1(r = r_1) = \Phi_2(r = r_1) \tag{2.87}$$

$$\vec{J_1}(r = r_1)\hat{n}_1 = -\vec{J_2}(r = r_1)\hat{n}_2 \tag{2.88}$$

By substitution and doing the necessary algebra we get:

$$\sigma_1 A_1 i c_1 J_n(1, ic_1 r_1) = \sigma_2(\frac{c_2^2 r_1}{2} + \frac{B_1}{r_1}) \tag{2.89}$$

$$B_1 = -\frac{c_2^2 r_2^2}{2} \tag{2.90}$$

$$A_1 = \frac{\sigma_2}{\sigma_1}\frac{1}{ic_1 J_n(1, ic_1 r_1)}(\frac{c_2^2 r_1}{2} + \frac{B_1}{r_1}) \tag{2.91}$$

$$B_2 = A_1 J_n(0, ic_1 r_1) - \frac{c_2^2 r_1^2}{4} - B_1 lnr_1 \tag{2.92}$$

With the determination of the 4 constants A_1, A_2, B_1, B_2 we have an analytical solution for our two dimensional problem. Dimensionally, these constants have all dimensions of potential. Predictions for this model for the case of interconnect radius $5 \cdot 10^{-3} m$ is given in figures 2.10,2.11,2.9. In these figures we can see respectively the same qualitative trends that we have seen in the two and the three dimensional models solved earlier by Comsol. Since this analytical solution provides exactly the same results as the two dimensional relative numerical model, our analytical solution is also quantitatively well established. One of the conditions fulfilled by the model is the equality of current through the two domains as expressed by:

$$\int_{\Omega_1} i_1 d\Omega_1 = \int_{\Omega_2} i_2 d\Omega_2 \quad \Rightarrow \int_{\Omega_1} \sigma_1 \frac{\Phi_1}{h_1} d\Omega_1 = \int_{\Omega_2} i_2 d\Omega_2 \tag{2.93}$$

An important feature of our solution, as presented in fig.2.10 is the fact that the change in the potential from the value on the boundary with the anode-anode support, takes place only in a portion of the pillar, on a thin "skin", rendering the rest of the material practically useless. An important goal thereafter, should be to decrease the waste material as far as possible, if there are no mechanical stability requirements prohibiting such reduction. Another crucial comment is the fact that because of the form of the drain term, the interconnect conductivity cancels out from the equation the PDE and it only enters our problem through the continuity boundary conditions. Despite this fact, the potential Φ_1 is proportional to the ratio $\frac{\sigma_2}{\sigma_1}$ as we can see from eq.2.92 and eq.2.80 and hence this ratio is an important parameter of our problem.

In figures 2.13 and 2.12 we can see the fitting by non-linear squares method of the negative of the analytical solution by an exponential $exp(a) \cdot exp(b \cdot r)$ with constants $:b = 2.5416e + 003, a = -22.3435$. Although we will not make use of

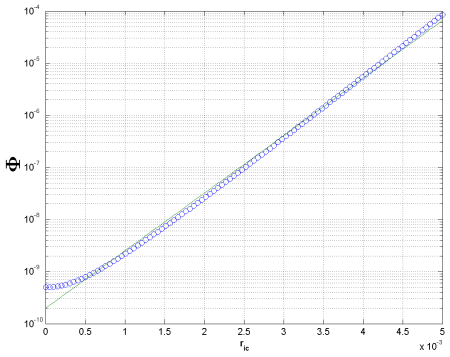

Figure 2.12: Potential in pillar in logarithmic scale and fitted line

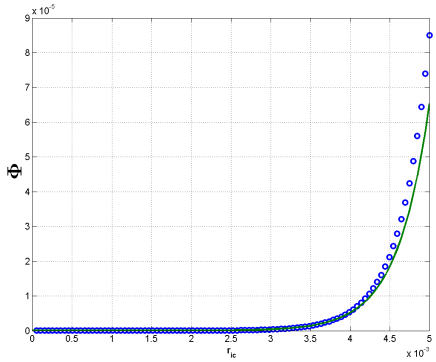

Figure 2.13: Potential in pillar and fitted line

this exponential fit it is useful because it facilitates a qualitative analysis when it is necessary on the fly.

From a conceptual but also practical point of view, having an analytical solution for the potential at our disposal is a great asset for a twofold reason. On the one hand, it allows the theoretical calculation of the power of the (half) cell and on the other, it offers a theoretical estimate for the length-scale of the pillar.

Dealing in the first place with the calculation of the characteristic length scale of the potential drop inside the interconnect we make use of the known from the relevant theory approximations of the modified Bessel function of zero order of the first kind. In the two distinct limits of the scaled variable $c_1 r$ taking values much less and much more than one it is proven that [30] it can take too distinct forms. By substitution for our $\Phi_1 = A_1 J_0(c_1 r)$ we get,

$$\Phi_1 = A_1 J_0(c_1 r) \quad = \quad \begin{cases} A_1 \sum_{k=0}^{\infty} \frac{1}{k!}^2 \left(\frac{(c_1 r)^2}{4}\right)^k, & c_1 r \ll 1 \\ A_1 \frac{exp(c_1 r)}{\sqrt{2\pi c_1 r}}, & c_1 r \gg 1 \end{cases} \tag{2.94}$$

In eq.2.94 having experimented with both the expressions we were able to conclude that for the series expansion actually 11 terms were sufficient. Since however the value of the constant c_1 being the reciprocal of the interconnect height is quite big, this means that for radii comparable to the parametric studies performed above, we can safely rely on the second approximation for our estimation. The calculation of the length-scale is done as usually, by extrapolating the line of the boundary rate of change at the interface with region 2 until it meets the horizontal axis. Estimation of the relative derivative and executing the necessary algebra, reveals the following expression for the meeting distance r^* at which the drop realized is approximately 63% of the boundary value.

$$r^* = r_1 \frac{2c_1 r_1 - 3}{2c_1 r_1 - 1} \tag{2.95}$$

We can use eq.2.95 to calculate the minimum element size that can capture the given structure of radius r_1. Another interesting notion by inpsection of eq.2.95 is that the length scale that determines the exponential rise (or decay depending on whether we are looking at actual Φ or its negative) solely depends on the chosen height of the interconnect gas channel.

As a quick validation of the last expression let us state that comparing the results with the exponential fit for $r_1 = 5 \cdot 10^{-3} m$ earlier described we get accordance more than $10^{-4}\%$. Of course expression 2.95 is much more powerful and generic and does not necessitate solving and fitting each time the solution. As a result it is of much greater significance and so is the approximation 2.94.

2.3 SOFC Anode Potential

In open circuit conditions, the potential drop between anode and cathode in any cell is equal to the theoretical maximum of the voltage that any H_2 fuel cell can provide. This in turn is known [3] to be given as the ratio of the maximum electrical energy that can be produced (Gibbs free energy) to the charge that is being transferred in the electrochemical reaction, resulting in:

$$V_N = V^0 + \frac{RT}{2F} ln \left(\frac{P_{H_2} P_{O_2}^{1/2}}{P_{H_2O}} \right) \tag{2.96}$$

where in the above $V^0 = \frac{-\Delta \bar{g}_f^0}{2F}$, $-\Delta \bar{g}_f^0$ is the change of molar Gibbs free energy of formation at standard pressure, F is the Faraday constant, R the universal gas constant, and P_k, $k = H_2, O_2, H_2O$ are the inlet partial pressures of hydrogen, oxygen and steam respectively. Assuming standard inlet conditions of weight fractions $w_{H2} = 0.8$, $w_{H2} = 0.2$ which in molar fractions are $x_{H2} = 0.9728$ $x_{H2O} = 0.0272$, and on the cathode side a surplus of air with $\lambda = 2$ we get a value for the Nerst potential: $V_N = 1.1V$.

Taking into account the various losses in the half cell, implicitly assuming a perfect cathode and electrolyte, and in general adopting the modeling procedure of [31] we can written:

$$V_{cell} = V_N - V_p^{an} - V_{conv}^{an} - V_{diff}^{an} + \Phi \tag{2.97}$$

where V_p^{an},V_p^{an} and V_p^{an} are the modeled potential drops of the voltage, translating also to power losses, because of polarization, conversion and diffusion mechanisms in the half cell's operation. It is true that the assumption especially of the perfect cathode is not realistic, since the cathodic losses in general are considerable. However, by the time we have completed this work it will have become

obvious that a similar model for the cathode can be built and by including the linearity of the ohmic contribution to the resistance by the electrolyte, we can thus model the whole fuel cell in steady state in two dimensions.

In the next few paragraphs we explain the nature of each term appearing in eq.2.97 and how and under which circumstances it is included in our calculations. In all the expressions that will follow we will be looking at values for the non-constant field variables, which are the concentrations (or equivalent molar fractions) and the potential in a random point p in the x-y plane. the index "inlet" refers at the inlet in the gas channel compositions of hydrogen and steam and the the "gc" to gas channel.

For all of this losses we assume an Ohmic dependence with the current density through the cell of the form:

$$V_m^{an} = i_2 \cdot R_m^{an}, \quad m = p, conv, diff. \tag{2.98}$$

- Polarization Loss. This term includes the heat generation coming from all the reaction steps of the hydrogen anode oxidation. This loss can be considered as independent of the electrode's potential.

$$R_p^{an} = A^{an} exp\left(\frac{E_a^{an}}{RT}\right)(x_{H_2})_{H_2}^{n}(x_{H_2O})^{n_{H_2O}} \tag{2.99}$$

  The coefficients in eq.2.99, dependent on the the micro-structure and the gas composition, are taken from [31] to be: $n_{H_2} = 0$, $n_{H_2O} = -0.35$, $A^{an} = 8.5 \cdot 10^{-6}[\Omega cm^2]$, $E_a^{an} = 77\frac{kJ}{mol}$. The operational temperature of the cell is for all our study $T = 1023K$ and $R = 8.31451\frac{J}{molK}$ The molar fractions will emerge from solving the mass balance problem and it will be handled in the following section.

- Conversion Loss. This loss accounts for the drop in the electromotive force that drives the reaction because of the change of composition as the fuel flows from left to right, in the direction of the flow. We thereby have:

$$V_{conv}^{an} = \frac{RT}{2F} ln\left(\frac{x_{H_2}^{inlet}}{x_{H_2}}\frac{x_{H_2O}}{x_{H_2O}^{inlet}}\right) \tag{2.100}$$

- Diffusion Loss. This term accounts for the drop in the driving electrochemical force by the fact that at the reaction sites, the molar fractions of hydrogen and steam are not the same as in the same location in the x,y plane in the gas channel. It holds that:

$$V_{diff}^{an} = \frac{RT}{2F} ln \left(\frac{x_{H_2}^{gc}}{x_{H_2}} \frac{x_{H_2O}}{x_{H_2O}^{gc}} \right) \tag{2.101}$$

In our implementation we distinguish three different levels of approaching the problem at hand. At each level we add one more of the afore-mentioned losses. i.e. At level 1 we include the polarization loss, at level 2 we add the conversion and at level 3 we add the diffusion loss. We can regard this splitting as 3 subproblems of the original one.
The current density through the cell can be calculated from the following linear equation:

$$i = \frac{V_N - V_{cell} - V_{conv}^{an} - V_{diff}^{an} + \Phi}{R_p^{an}} \tag{2.102}$$

It is generally known this simplification emerges from a linearization of the Butler-Volmer equation at equilibrium conditions. So it is very likely that this assumption breaks down and that eq.2.102 is not globally valid throught the whole range of the design space explored. However, as already mentioned in our case the use of eq.2.102 is not dictated by simplicity arguments, but by our need to decompose it in a part that depends on the overpotential u and a constant part. i.e. we wish to write:

$$i = \frac{V_N - V_{cell} - V_{conv}^{an} - V_{diff}^{an}}{R_p^{an}} + \frac{\Phi}{R_p^{an}} \tag{2.103}$$

so that we can include this decomposed form into eq.2.72. Treating an expression like the Butler-Volmer or more complicated ones suggested in the literature is also an option and a proposed extension of our work. Computing the current for each point in our design domain, necessitates the calculation of the involved potential losses. The potential of the cell, V_{cell} is treated as an input parameter in our problem. From here on we can drop the index denoting the anode that was used only for introductory purposes, since we are treating just the anode side of the cell.

2.4 Mass Transport

Depending on the just above described level of precision on the calculation of the current density by gradual inclusion of the different terms in eq.2.102 the adequacy of the level of the physics to account for mass balance and transport changes as well.

- At level 1 at which we neglect both V_{conv} and V_{diff} the mass balance in the gas channel of the interconnect can be adequately described by $\nabla \cdot \mathbf{u} = 0$,

since at this approximation there are no reactions and no change in the gas composition in our problem. For the solution of this subproblem it suffices to take into account equations 2.14 setting the gradient of the density to zero, 2.72 and 2.69 (combined they describe the potential both in areas with current collector pillars and anode-anode support) and 2.102 setting the diffusion and conversion losses to zero. This is a system with four unknowns, velocity pressure and potential and four equations. For this case alone, an analytical solution of the velocity the pressure and the potential fields is possible.

- At level 2, the conversion loss is included. This means that we need to have access to the molar fractions of the species in the gas mixture. This is accomplished by solving the convection-diffusion-reaction equation, [1]:

$$u_j \partial_j(\rho w_k) = \partial_j(\rho D_k \partial_j(w_k)) + \omega_k \tag{2.104}$$

w_k is the corresponding mass fraction, $k = H_2, H_2O$, D_k is the binary diffusion. The assumption that we make at this point is that the gas is a binary mixture and consequently the diffusion can be considered to be adequately described by Fick's law. We also note that equation 2.104 is in essence the same as eq.2.1.

The density ρ now is a variable density in every point p in our domain and needs to be calculated from its constituents. Under the perfect gas assumption for the mixture and its individual constituents, we have:

$$\rho = \rho_{H_2} + \rho_{H_2O} = \frac{P(x_{H_2} M_{H_2} + x_{H_2O} M_{H_2O})}{RT} \tag{2.105}$$

where by M we have denoted the molecular weights and P the gas channel's pressure.

The term ω_k^p in eq.2.104 is the reaction term that is given by

$$\omega_k = \begin{cases} -\frac{iM_{H_2}}{2F}, & k = H_2 \\ +\frac{iM_{H_2O}}{2F}, & k = H_2O \end{cases} \tag{2.106}$$

The Peclet number of this setup defined as $Pe = \frac{UL}{D}$ for typical values of our simulations is in the order of magnitude of 100 so convection is dominating and the convective flux boundary condition at the outlet is also valid. The closed system of coupled equations to be solved has now been expanded and includes 2.104, 2.106, 2.105, 2.3, 2.14, 2.72 and 2.69. Overall there are 6 independent equations form a system with additional unknowns from the

previous case the two concentrations. This model because of its coupled form is solved only numerically in Comsol.

- At the third more sophisticated and also more realistic level of our treatment, inclusion of diffusion on the vertical to the flow plane direction is required. Since our model is a two dimensional model, we incorporate the computation of the concentrations and molar fractions at the anode by assuming for every point of the x,y plane a one dimension linear relation between the gas channel and the anode taking the mass flux in each case to be equal to the local reaction generation or consumption.

$$\omega_k \cdot M_k = J_k = D^{eff} \frac{c_k^{an} - c_k^{gc}}{h_{as}} \tag{2.107}$$

The closed system now has two more variables and two more equations, in total 8.

In eq.2.107 we have assumed a Fickian diffusion form. However, unlike before, this is not a good approximation for the tortous path that the gases follow inside the porous anode support material. This is due to the fact that the collision frequency between the molecules of the mixture has changed in comparison to the value of the open channel and the collisions with the wall depending on the pore size must also be included (Knudsen diffusion). In order to correct this we use an effective corrected diffusivity based on the literature e.g. [32] on the Bosanquet approximation.

$$D^{eff} = \left(\frac{1}{D_{ij}^{eff}} + \frac{1}{D_K^{eff}} \right)^{-1} \tag{2.108}$$

where D_{ij}^{eff} is the effective binary diffusivity and D_K^{eff} is the effective Knudsen diffusion. These effective diffusivities accounting for the tortous paths include the term ϵ/τ , ϵ being the porosity of the material and τ the tortuosity. By making the common assumption of $\epsilon/\tau = \epsilon^{1.5}$ we get:

$$D_{ij}^{eff} = \epsilon^{1.5} \frac{0.0143 T^{1.75}}{P \cdot (10^3 M_{ij}) \left({\Sigma_i}^{1/3} + {\Sigma_j}^{1/3} \right)^2} \tag{2.109}$$

$$D_k^{eff} = \epsilon^1.5 \frac{97}{2} d_p \left(\frac{T}{10^3 M_{ij}} \right)^{1/2} \tag{2.110}$$

In the above, $M_{ij} = \frac{1}{\frac{1}{M_i} + \frac{1}{M_j}}$ is the average molecular mass and Σ_i,Σ_j are the diffusion volumes of species i and j respectively. Finally, the pore size d_p

is calculated as function of the particle size of which the anode constitutes of according to:

$$d_p = \frac{2d_{part}\epsilon}{3(1-\epsilon)} \tag{2.111}$$

Using the values , $\epsilon = 0.3$, $d_{part} = 3\mu m$ we compute the following values which are included in our model: $D_{H_2,H_2O} = 3.5682 \cdot 10^{-4}$, $D^{eff}_{H_2,H_2O} = 5.8631 \cdot 10^{-5}$, $D_K = 1.1751 \cdot 10^{-4}$ and finally $D^{eff} = 3.9114 \cdot 10^{-5}$

2.5 Energy balance

The analysis made so far in the context of this work has demonstrated that under certain accepted in the most part simplifications, it is possible to derive analytical expressions for the solution of the first of the three subproblems we are dealing with. Still the theoretical derivations made are powerful and allow for calculations over a wide range of sizes of geometries exhibiting axial symmetry. Our primary interest in taking advantage of what we have discussed so far, is to derive expressions that offer the possibility to grasp the direction that an optimized cell, in terms of the net power generated, should lead. The temperature distribution has not been included in this approach, but having the gas concentrations and velocity field everywhere, the addition of the thermal balance is a natural and imminent extension of our work. However, this does not mean that we cannot perform accurate power calculations, because we have taken into account all the heat generation emerging in the cell. More specifically we have accounted for:

- The electrochemical conversion of H_2 and all its steps modeled by the polarization resistance as well as all the other electrode losses that eventually also get converted to heat.
- The fluid power dissipation transformed to heat.
- The current collector's joule heating is easy to be added having computed the power density that goes through it.

We refer to the net power generated by the cell (without the current collector) P_{GEN}.

$$P_{GEN} = V_{cell} \cdot \int_{\Omega_2} i_2 d\Omega_2 = V_{cell} \cdot \int_{\Omega_2} \frac{V_N - V_{cell} + \Phi_2}{R_p} d\Omega_2 \tag{2.112}$$

R_p is a fixed value for the whole domain relying on the inlet steam molar fraction. Because of the power law, using a lower than what it should be H_2O molar fraction results in a higher than what it should be value for R_p, resulting in underestimating the current. On the other hand, omission of the conversion

and diffusion losses over estimates the current, so some kind is achieved and the current is actually more realistic than one would expect.

The current collector Joule heating:

$$P_{JHIC} = \int_{\Omega_1} (\Phi_1 - V_0) \cdot i_1 d\Omega_1 = \int_{\Omega_1} \Phi_1 \cdot i_1 d\Omega_1 \tag{2.113}$$

The net power that we get out from operating a cell with the afore-mentioned contributions, takes the form:

$$P_{Net} = P_{GEN} - \Phi_D - P_{JHIC} \tag{2.114}$$

Which because of eq.2.54, eq.2.112 and eq.2.113 can be rewritten as:

$$\begin{aligned} P_{Net} = V_{cell} \cdot \int_{\Omega_2} \frac{V_N - V_{cell} + \Phi_2}{R_p} d\Omega_2 - \int_{\Omega_1} \Phi_1 \cdot \frac{\sigma_1 \Phi_1}{h_1} d\Omega_1 \\ - \int_{\Omega_2} \mu \left[2 \left[\left(\frac{\partial u_r}{\partial r} \right)^2 + \left(\frac{1}{r} \frac{\partial u_\theta}{\partial \theta} + \frac{u_r}{r} \right)^2 \right] + \left[r \frac{\partial}{\partial r} \left(\frac{u_\theta}{r} \right) + \frac{1}{r} \frac{\partial u_r}{\partial \theta} \right]^2 \right] d\Omega_2 \end{aligned} \tag{2.115}$$

To conclude these theoretical investigations and in order to show how these derivations can bee of service when dealing with energetic concepts, we confine ourselves in studying a case that fulfils the criterion of $r > \frac{h}{\sqrt{12}}$ from the flow perspective and $c_1 r \gg 0$ from the potential perspective. To satisfy both these, we will do a parametric study similar to the one done in the context of the electrical problem. We fix the radius of area 2 to $1cm$ and the radius of area 1 will range with a step of $1mm$ from $2mm$ to $8mm$.

By doing the necessary integrations over the appropriate domains we get,

$$P_{GEN} = \frac{2\pi V_{cell}}{R_p} \left(\left[V_N - V_{cell} + \frac{B_2}{2} - \frac{B_1}{4} \right] (R_2^2 - R_1^2) + \frac{c_2^2}{16} (R_2^4 - R_1^4) + \frac{B_1}{2} (R_2^2 ln(R_2) - R_1^2 ln(R_1)) \right) \tag{2.116}$$

$$P_{JHIC} = \frac{\sigma_1 A_1^2}{2c_1} \left(e^{2c_1 R_1} - 1 \right) \tag{2.117}$$

The valid expression for the fluid flow dissipation function in this case is given by eq.2.67. Finally, the expression that provides the net power that we get out of the cell is:

$$\begin{aligned} P_{Net} = \frac{2\pi V_{cell}}{R_p} \left(\left[V_N - V_{cell} + \frac{B_2}{2} - \frac{B_1}{4} \right] (R_2^2 - R_1^2) + \frac{c_2^2}{16} (R_2^4 - R_1^4) + \frac{B_1}{2} (R_2^2 ln(R_2) - R_1^2 ln R_1) \right) \\ - \frac{\sigma_1 A_1^2}{2c_1} \left(e^{2c_1 R_1} - 1 \right) - \frac{4\pi h U^2 \mu}{3R_2^4} (-9R_1^4 + 16R_1^3 R_2 - 9R_1^2 R_2^2 + 2R_2^4) \end{aligned} \tag{2.118}$$

Equation 2.118 is an analytical expression whose thorough investigation can lead in the determination of the set of parameters that lead to the maximization of the net power we can get out of the cell. A full scan with the parameters entering the closed analytical expression of the P_{Net} will reveal its rich content. From the analysis we have performed so far, it has become evident that the important parameters of the problem are, the ratios $\frac{r_1}{r_2}$ and $\frac{\sigma_1}{\sigma_2}$, the channel's height h_1,cell's potential V_cell, and the inflow velocity U in the channel. Below we present characteristic plots of the power expressions derived for a set of parameters (additionally to those described in table 2.1 and the constants for the calculation of R_p as explained in the mass transport section), $V_{cell} = 0.8V$, $U = 2.5\frac{m}{s}$, viscosity and density corresponding to the inlet gas compositions, $\rho = 0.0278\frac{kg}{m^3}$, $\mu = 6.4 \cdot 10^{-5} Pa \cdot s$

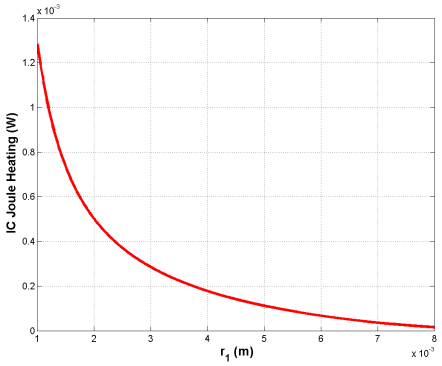

Figure 2.14: Joule Heating of the interconnect pillar as a function of the cylinder's diameter

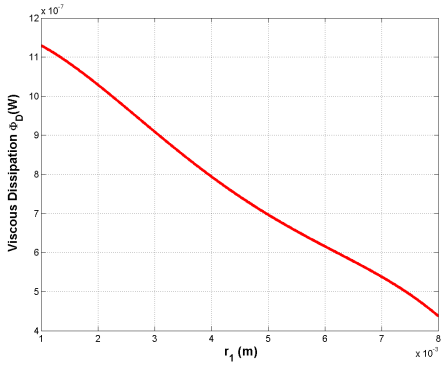

Figure 2.15: Fluid dissipation of the flow around the pillar as a function of the cylinder's diameter

Two very interesting trends that we can see at once, is that the power generated dominates by far over the two extra losses terms and the viscous dissipation i far from competing, mainly due to the very low viscosity of the gas at the given temperature. Furthermore, we are able to see that for the set the specific set of parameters, the power generated and consequently the net power exhibit a distinct maximum at $r_1 = 0.0032mm$ of $6.9070W$ and $6.9068W$ respectively. Such and other similar optimizations can emerge by sweeping through a well selected parametric space based on eq.2.118 as well as from deriving the corresponding expressions for the the whole range of possible variations of the cylinder's size and this is an on going work. *

*To be submitted for publication soon after the end of the PhD

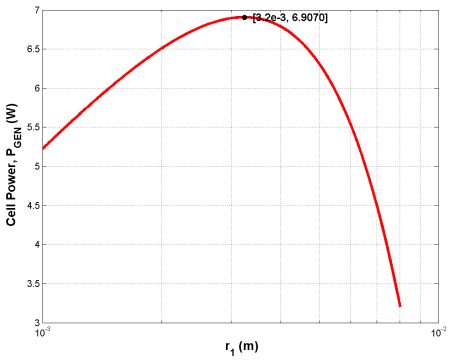

Figure 2.16: Cell Power Generation as a function of the cylinder's diameter

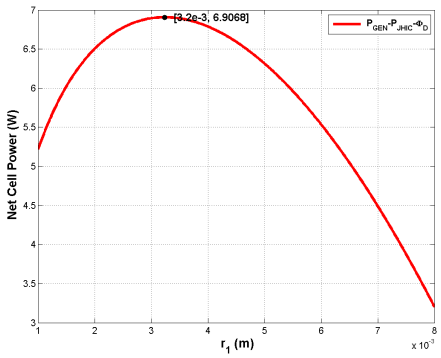

Figure 2.17: Net Cell Power as a function of the cylinder's diameter

Chapter 3

Topology Optimization Introduction

3.1 Literature overview

Topology optimization was initially introduced in the context of structural mechanics by Bendse and Kikuchi [33]. The primal objective of those early applications where problems for the optimization of the performance of beams under various loading situations, given some volumetric constraints for the amount of material to be used. The method's versatility and universality resulted in its expansion in may fields where optimal designs are sought, with more pronounced examples the design of optical and acoustics devices, structural mechanisms and fluidic applications. Full overviews of the subject are presented in [34], [35] and [36]. The goal of the method in each case, is to introduce and define the shape and size of material in a computational domain where on the background the solution of a physical problem takes place, usually in the form of some coupled together PDE's with their boundary conditions. To distinguish between areas of solid and free areas, we usually assign black color to the sold phase and white to its complementary. The discretization of the problem, usually through the handy finite elements analysis, implies that the domain consists of a group of elements (e.g. triangular, quadrilateral). Hence, the introduction of material in an element or a sub-group of elements and its absence in other areas, would result in an integer problem. This would be highly undesirable, because of the non differentiable and highly discontinuous nature of the stiffness matrix even under regularization. Thus, it has been proposed to use instead a continuous density function. In this way, it is expected to have a smooth transition between the black and the white, resulting in gray areas in the design domain. This approach is known as the Solid Isotropic Material Penalization Method (SIMP).

The branch of topology optimization in fluid mechanics was introduced by Borvall and Petersson [20]. In their original work, they provided theoretical proof of the well posedness of the solution coming from the application of the method on a Stokes flow in two dimensions and they made the transition of the necessary concepts from the already advanced solid mechanics field to fluid mechanics. The realization of the continuous interpolation between areas of material and of no material was based on a Brinkman model for porous media, at which the local permeability was linked to the design continuous design variable. This means that in free channel areas the local permeability should be zero while when a solid obstacle is created, the local permeability increases enormously, penalizing the flow and almost shutting it off in this region. An extension from the Stokes flow regime to moderate Re was made by [37] and [38].The theoretical backup for the use of the incompressible Navier-Stokes equations in the laminar regime was provided by [39] while in [40] the mathematical foundation of the original Stokes problem was also expanded. An alternative approach using a combined Stokes-Darcy equation and equal order quadrature for velocity and pressure (for stabilization purposes) as found in [41], was applied for the whole range of incompressible Navier-Stokes. Three dimensional work in fluid problem has also been reported e.g. [42], [43] although the increase in the size of the problem requires significantly more computational power compared to the $2d$ simulations. A different than ours description for the damping term accounting for the collapse of the the third dimension of the fluid flow relies on mapping and parameterization on the midplane of the height and finally renormalization using the parabolic velocity profile from lubrication theory [38].
The idea of applying topology optimization in fuel cells modeling has emerged lately as a natural extension of the progress in modeling fluid/porous media flows. However the level of complexity of the necessary modeling to take into account the multiplicity of physical phenomena involved, is by definition cumbersome. Two relative works found in the literature are [44] and [45] . In the former, optimization of gas channels for SOFC cathodes in the perpendicular to the flow direction is studied. They included a convection-diffusion equation in the gas channel and an ionic potential field with diffusivity and electrical conductivity dependent on the design variable. Their design parameter was the channel aspect ratio. As objective function was chosen the maximum current output from the cathode and they recorded an $8\% - 9\%$ increase of the optimized results when compared to a reference case. In the later work, optimization of anode gas channels in PEM Fuel Cell was attempted in the same as before direction, in terms of optimizing the route of the gas introduction and branching in the cell. The applied equations used where Navier-Stokes, convection diffusion reaction for the hydrogen being the only constituent of the fuel gas.

3.2 Mathematical Formulation of Optimization Problems

Any optimization problem consists of some fundamental pieces of information and a problem's setup that has to be put into mathematical form if we are about to treat it in a generic and efficient way in order to allow us to treat problems for all the scope of science and engineering. Assuming that we have a space of n design parameters, x_n whose full determination completely defines all the expression entering our problem. Let us further assume now, that there is function of these design parameters, that we wish it to accomplish a maximum or a minimum value. Since this maximization or minimization is the purpose, or in other words, the objective of our study, we call this function, objective function, and we denote it by $\Phi_{obj}(x_1, x_2, .., x_n)$. The design parameters will in the general case satisfy a set of equality constraints and another set of inequality constraints. As a result the optimization problem consists exactly of the determination of the design parameters vector, that while satisfying all the constraints, accomplishes the sought optimization. Since maximization of any function can be considered as the minimization of its negative, the standard convention of the formulation of any optimization problem, acquires the following form [46]:

$$\begin{aligned} &min \quad \Phi_{obj}(\mathbf{x}) = \Phi_{obj}(x_1, x_2, ..., x_n) \\ &h_j(\mathbf{x}) = h_j(x_1, x_2, ..., x_n) = 0, \quad j = 1 \quad \text{to} \quad p \\ &g_i(\mathbf{x}) = g_i(x_1, x_2, ..., x_n) \leq 0, \quad i = 1 \quad \text{to} \quad m \end{aligned} \tag{3.1}$$

We note that the inequality constraints contain the so called, "box" constraints for the x_n as well, i.e. constraints of the form, $x_{nlow} \leq x_n \leq x_{nupper}$

Chapter 4

Topology Optimization Methodology

The purpose of this chapter is to present all the necessary steps for the formulation of our problem, the definition of all the equality and inequality constraints and derive the appropriate form for the objective to be by convention minimized according to the common practised adopted in eq.3.1.

4.1 Fluidic Power Dissipation

In all cases, the dissipated in the fluid power is given by [37], [47]:

$$\Psi_D(\mathbf{u}, P, \gamma) = \int_\Omega \left[\frac{1}{2}\mu \sum_{i,j} \left(\frac{\partial u_i}{\partial x_j} + \frac{\partial u_j}{\partial x_i} \right)^2 + \sum_i \alpha(\gamma) u_i^2 \right] d\mathbf{r} \tag{4.1}$$

The late expression, under the condition of steadiness of the flow and no slip condition on the walls parallel to the flow direction, is equal to the work by external forces (pressure) and the increase in the kinetic energy:

$$\Psi_D(\mathbf{u}, P, \gamma) = \int_{\partial\Omega} -\mathbf{n}\mathbf{u} \left(p + \frac{1}{2}\rho u^2 \right) ds \tag{4.2}$$

4.2 Governing Equations

In the context of deriving the necessary equations, following the convention of the previous chapter, we continue referring to the areas where solid material arises as area 1 and its complementary open for fluid flow and also anode and anode

support power generation, as area 2. We highlight however that these indices do not refer to different design domains.

As already discussed in the theoretical investigations on the mass transport we have attempted to solve numerically 3 different subproblems.

4.2.1 Subproblem 1

Only the fluid flow for a constant composition gas and the electrical problem are treated, cut off from any connection to the actual electrochemistry of the problem. This can be of relevance when in general it can be argued that the average fluctuations of the density in the flow and of the current in the electrical problem do not deviate significantly from the values used here. Similar works e.g.[48] point to this conclusion of week coupling between the gas channel fluid flow and the electrochemical processes, making this approach particularly handy.

The form of the Navier-Stokes equation for this case is:

$$\rho(\mathbf{u}\cdot\nabla)\mathbf{u} = \nabla P + \mu\nabla^2\mathbf{u} - \alpha\mathbf{u} \tag{4.3}$$

The boundary conditions used are constant inlet flow-rate on the left edge, symmetry on the top and bottom and atmospheric pressure at the outlet.

The LHS in eq.4.3 is the convective term and the RHS consists of the pressure gradient, the viscous term and finally the damping term. This last term has a dual role. In the area of the fluid flow ($\gamma = 1$)the damping comes from adequately describing in the two dimensions the suppression of the flow in the third (flow through a slit) with:

$$\alpha_{min} = \frac{12\eta}{h_{ic}^2} \tag{4.4}$$

as described in the theory chapter. In the area where interconnect regions are created by the topology optimization ($\gamma = 0$)the extreme damping experienced by the flow is linked to the local permeability and design parameter γ and the value of the damping term acquires its maximum value:

$$\alpha_{max} = \frac{\eta}{DaL^2} \tag{4.5}$$

L being the length scale of the problem. This is done by defining a sufficiently low Darcy number which in all cases for our numerical investigations was taken to be $Da = 10^{-5}$

The interpolation between these maximum and minimum values for α is done by:

$$\alpha = \alpha_{max} + (\alpha_{min} - \alpha_{max})\cdot\alpha_0 \tag{4.6}$$

where:

$$\alpha_0 = \frac{\gamma(q+1)}{q+\gamma} \tag{4.7}$$

The value of the parameter q defines the convexity of the interpolation of α between its minimum and maximum values as γ changes. For $q << 1$ the interpolation is very convex while for $q > 1$ becomes linear as shown in fig.4.1 for some indicative values. These values are generally problem dependent. In our case we used the following vector $q = [10^{-4}, 10^{-3}, 10^{-2}, 10^{-1}1]$. The progressive increase and finally the use of an almost linear interpolation emanates from the conclusion of Borvall and Petersson that for the Stokes regime a linear interpolation scheme ensures a full discretization between areas of zero and one in the design domain.

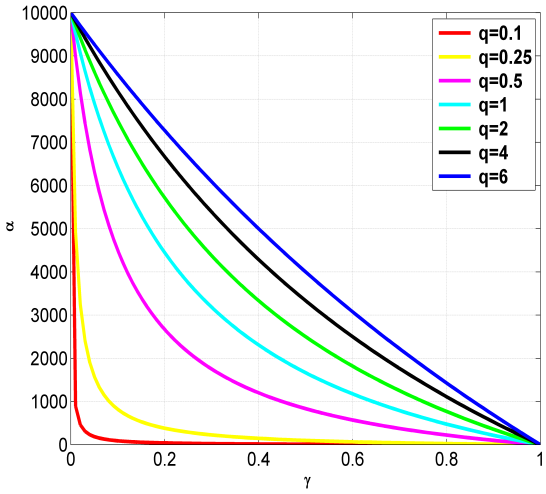

Figure 4.1: $\alpha - \gamma$ interpolation with different values of parameter q. $\alpha_{max} = 10000, alpha_{min} = 0$

The equation that describes in two dimensions the electrical problem is written as follows:

$$(\gamma h_2\sigma_2 + (1-\gamma)h_1\sigma_1)\nabla^2\Phi - \left((1-\gamma)\frac{\sigma_1}{h_1} + \frac{\gamma}{R_p}\right)\Phi = \frac{V_N - V_{cell}}{R_p} \tag{4.8}$$

As also discussed earlier, the top of the interconnect is assumed to be grounded. The boundary condition is electrical insulation in all four edges of the design domain, i.e. $\frac{\partial\Phi}{\partial n}$, n being the normal to the edge outward vector.

The coupling for the two problems, though solved simultaneously, is indirect through the geometry. Along with the continuity equation:

$$\nabla \cdot \mathbf{u} = 0 \tag{4.9}$$

we have a system of four equations and four unknowns the velocity (u,v), pressure P and potential Φ.

The objective function is:

$$\Phi_{obj} = \int_{\Omega} \left[\gamma \cdot V_{cell} \cdot \frac{V_N - V_{cell} + \Phi}{R_p} - \gamma \cdot \Phi_D - (1-\gamma)\frac{\sigma_1}{h_1}\Phi^2 \right] \tag{4.10}$$

4.2.2 Subproblem 2

In this case we include as a novelty of our work the changing density gradient and also account for the varying concentrations of the constituents of the gas anode mixture. The Navier-Stokes now reads:

$$\mathbf{u}(\mathbf{u}\nabla)\rho + \rho(\mathbf{u}\cdot\nabla)\mathbf{u} = \nabla P + \mu\nabla^2\mathbf{u} - \alpha\mathbf{u} \tag{4.11}$$

The convection-diffusion-reaction problem is written as:

$$\mathbf{u}\nabla(\rho w_k) = \gamma \cdot D_k \nabla^2(\rho w_k) + \omega_k \tag{4.12}$$

where $k = H_2, H_2O$, D_k the binary diffusion. The boundary conditions for the concentrations are: fixed concentration multiplied with a Heaviside function to smooth the transition at the inlet, symmetry on top and bottom and convective flux at the outlet. In the above, the velocity field is already carrying the information on γ. The information of γ in reaction rates is passed through:

$$\omega_k \quad = \quad \begin{cases} -\frac{i_2 M_{H_2}}{2F}, & k = H_2 \\ +\frac{i_2 M_{H_2O}}{2F}, & k = H_2O \end{cases} \tag{4.13}$$

where the current and potential are:

$$i_2 = \gamma \frac{V_N - V_{cell} - V_{conv} + \Phi}{R_p} \tag{4.14}$$

$$(\gamma h_2\sigma_2 + (1-\gamma)h_1\sigma_1)\nabla^2\Phi - \left((1-\gamma)\frac{\sigma_1}{h_1} + \frac{\gamma}{R_p}\right)\Phi = \frac{V_N - V_{cell} - V_{conv}}{R_p} \tag{4.15}$$

From the extra equations in comparison to subproblem 1, only two are independent. Finally, we have a system of 6 coupled equations for 6 unknowns.

The problems objective function reads:

$$\Phi_{obj} = \int_{\Omega} \left[\gamma \cdot V_{cell} \cdot \frac{V_N - V_{cell} - V_{conv} + \Phi}{R_p} - \gamma \cdot \Phi_D - (1-\gamma)\frac{\sigma_1}{h_1}\Phi^2 \right] \tag{4.16}$$

4.2.3 Subproblem 3

The two additional equations in this subproblem are:

$$c_k^{an} = c_k^{gc} \frac{\omega_k M_k h_2}{D^{eff}} \tag{4.17}$$

and the potential includes the relevant losses:

$$(\gamma h_2 \sigma_2 + (1-\gamma) h_1 \sigma_1) \nabla^2 \Phi - \left((1-\gamma) \frac{\sigma_1}{h_1} + \frac{\gamma}{R_p} \right) \Phi = \frac{V_N - V_{cell} - V_{conv} - V_{diff}}{R_p} \tag{4.18}$$

as well as the current:

$$i_2 = \gamma \frac{V_N - V_{cell} - V_{conv} - V_{diff} + \Phi}{R_p} \tag{4.19}$$

We now have a 8 by 8 system of independent coupled equations.
The objective function for this cases takes the form:

$$\Phi_{obj} = \int_\Omega \left[\gamma \cdot V_{cell} \cdot \frac{V_N - V_{cell} - V_{conv} - V_{diff} + \Phi}{R_p} - \gamma \cdot \Phi_D - (1-\gamma) \frac{\sigma_1}{h_1} \Phi^2 \right] \tag{4.20}$$

4.3 Problem in divergence form

Following the formulation of [37] the problem is set in the convenient for finite elements analysis, divergence form as follows:

$$\nabla \Gamma_i = F_i, \qquad \text{in} \quad \Omega, \text{Governing equations} \tag{4.21}$$

$$R_i = 0 \quad on \qquad \partial\Omega, \text{Dirichlet} \qquad \text{B.C.} \tag{4.22}$$

$$-\mathbf{n} \cdot \Gamma_i = G_i + \sum_{j=1}^{3} \frac{\partial R_j}{\partial u_i} \lambda_j, \quad \text{Neumann B.C} \tag{4.23}$$

In the above, Γ_i is a 2 by 1 vector in each case, which is associated with the diffusive term in each one of the PDEs introduced at the governing equations section. More specifically, it is taken as the ith column of the relative tensor (the projection in the x and y directions). The vector F contains all the other terms of the governing equations moved to the right hand side.

4.4 Objective function

It is worth noticing now, how each one of the terms involved in the expression of the objective function behaves in terms of material emerging in the design

domain as the optimization process moves along. We will analyze this behavior in the context of subproblem 1 because it exemplifies sufficiently for all the cases.

Though we use in our calculations eq.4.1, we will use eq.4.2 to derive our conclusions in the context of this discussion because it is much offers a much more illustrative way of the energy interplay of the fluid.

Referring to eq.4.10 we examine each term separately.

- $\gamma \cdot V_{cell} \cdot \frac{V_N - V_{cell} + \Phi}{R_p}$. This term comes form the anode-anode support material and is governed by the difference $V_N - V_{cell} + \Phi$ everything else being a constant. In fig.2.6 and in the analytical solution we derived for the potential in this region, it was evident that the potential follows a parabolic profile which deepens the further two hypothetical pillars are put. In this way, by increasing the distance between these two pillars, the value of $V_N - V_{cell} + \Phi$ will decrease and so will the power generated by the anode-anode support layers. In other words, bringing up new material in the domain ΩS or bringing closer existing increases this term. Hence maximization of this term, introduces material in the domain.

- $\gamma \cdot \Phi_D$. In order to assess the effect of changes in this term, we refer as mentioned to eq.4.2. From this expression, it can be deduced that under the constant flowrate boundary condition at the inlet, minimization of this term, requires minimization of the hydraulic resistance and hence it favors removing material from the domain.

- $(1 - \gamma)\frac{\sigma_1}{h_1}\Phi^2$. This term comes form expressing the thermal losses in the current collector. Its role, according to the reasoning for the anode-anode support first term, is that its minimization also favors introduction of new material

From the above analysis, it is obvious that two out of the three terms are responsible for the introduction of material in our domain while only the term coming from the fluid's dissipated power tends to create free passage. All the above are also from an intuitive point of view correct.

4.5 Optimization

Our problem with respect to mathematical optimization theory is formulated as follows:

$$\begin{aligned} &min \quad \Phi_{obj}(\mathbf{u}(\gamma), \gamma) \\ &\int_{\Omega} \gamma(\mathbf{r}d\mathbf{r} - \beta|\Omega|) \leq 0, \\ &\quad 0 \leq \gamma(\mathbf{r}) \leq 1, \\ &eq.4.9, 4.3, 4.8, 4.11, 4.12, 4.15, 4.18, 4.17 \end{aligned} \tag{4.24}$$

where, β is the fraction of the design domain that is not to be covered by material and the cited equations are the governing equations of our in total. So each subproblem is taking the above form with each one governing equations and boundary conditions.

In mathematical optimization, the literature on strategies to solve an optimization problem, is enormous. Factors on which the choice of the algorithm usually are the existence or no existence of constraints, the order and the linearity or non-linearity of the system of equations and the constraints, accurate access to information for computing the gradient and the Hessian, the degrees of freedom of the problem and so on. Usually information of the Hessian or to its approximation is computationally expensive, so gradient based methods like the steepest descent or conjugate gradient are preferable. In the case of topology optimization however, with many degrees of freedom and few constraints a more efficient choice is the Method of Moving Asymptotes (MMA) developed by Svanberg [49] and it is the choice that we also make in the context of our work in order to update in each iteration the design variable γ, based on the information and the sensitivity analysis of the previous step.

4.6 Sensitivity Analysis

According to standard finite element theory, the generalized vector of the solution $\mathbf{V}$ of the governing equations is approximated by a set of basis functions, $\phi_{i,n}$ and so is the design variable γ with corresponding expansion coefficients. This approximation results in a discretized, linear or non-linear system of equation according to the choice of the basis functions and the form of the PDEs.

We used the well known Taylor-Hood scheme for satisfying the Ladyszhenskaya-Babuska-Brezzi (LBB) stability criterion [50]. The scheme imposes a second order quadrature for the velocity and first order for the pressure [20], [37], [42] built in a combined way to ensure the convergence of the discrete solution to the continuous one.

For the potential Φ, and the concentration fields second order elements were also used. For the gamma field, it suffices to use Lagrange elements of first order.

The sensitivity analysis is dealing with calculating the gradient:

$$\frac{d}{d\gamma}[\Phi_{obj}(\mathbf{V}(\gamma),\gamma)] = \frac{\partial \Phi_{obj}}{\partial \gamma} + \int_{\Omega} \frac{\partial \Phi_{obj}}{\partial \mathbf{V}} \cdot \frac{\partial \mathbf{V}}{\partial \gamma} d\mathbf{r} \tag{4.25}$$

This gradient provides information of the dependence of the objective function on the design variable and the solution (which is also a function of the design variable) and it is a necessary input in the gradient based routine, in our case MMA, in order to update the design variable for the next step in the iteration process. The calculation of $\frac{\partial \Phi_{obj}}{\partial \gamma}$ employs the standard adjoint method [51], [37].

4.7 Implementation

4.7.1 Numerical Setup-Geometry-Boundary conditions

The implementation was realized using the scripting interface of Comsol to Matlab. In the codes used, which are set up for minimization, the objective function, that we wish to be maximized, is entered as its negative.

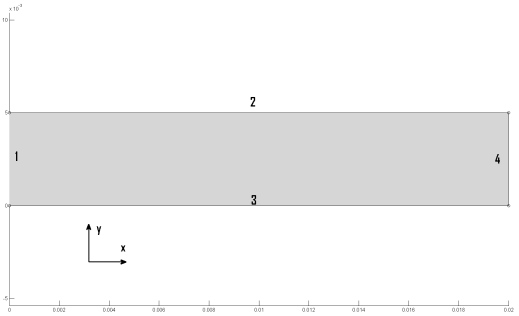

Figure 4.2: Design domain

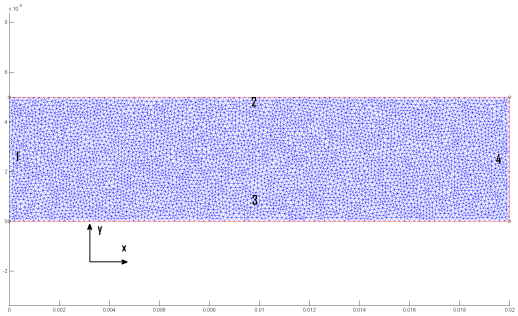

Figure 4.3: Typical mesh

The domain used in depicted in fig. 4.2It is a two dimensional rectangle of dimensions $w = 5mm$ (y axis) and length $L = 2cm$ (x axis). The domain was taken so small because of the fine meshing needed because of the concentration fields which were very demanding and of the absence of stabilization techniques. A typical mesh for Subproblem 1 is shown in fig.4.3. The maximum element size is 10^{-4} and an unstructured mesh like the one presented here is always used.

The boundary conditions are as follows:

- Fluid Flow. Uniform inlet velocity Uo_{in} (edge 1) and atmospheric pressure condition at the outlet (edge 4). Symmetry boundary conditions on the top and bottom (edges with numbers 2 and 3). The severe damping of the flow by the extreme aspect ratio of the channel, makes indifferent actually if the incoming condition is a parabolic or bulk uniform value in terms of the designs achieved.

- Electrical Helmholtz. Zero flux condition on all the four edges of the domain.

- Concentrations in the gas channel. Fixed concentration inlet weight fraction for fuel gas, smoothed by a Heaviside function to alleviate discontinuities. However, this alleviation proved to be more challenging than expected. The exit condition is convective flux while edges 3 and 4 are zero Neumann conditions.

- Concentrations in the anode. This values are a mere numerical linear mapping of the gas channel's concentrations as already explained and the same holds for the boundary conditions.

The parametric sweep performed for our numerical experiments are depicted in the following table.

Table 4.1: Values of parameters used in simulations

Parameters	$\mathbf{V_{cell}}(V)$	$\mathbf{Uo_{in}}\left(\frac{m}{s}\right)$	$\sigma_{\mathbf{ic}}\left(\frac{S}{m}\right)$
Values	0.7, 0.8	0.25, 0.5 1	10^2, 10^3, 10^4, 10^5, 10^6

The low electrical conductivities appearing in our parameters space emerge from the fact that the pillar that collect and conduct the electronic current are in real designs covered by protective to corrosion layers. Assuming that these coatings have a significantly lower conductivity than the one of the metallic material of the interconnect, we treat the two as single material with an electronic conductivity interpolated between the minimum, (coating), and maximum, (steel), values.

We also stress out the fact that all our numerical work, in the same way as our theoretical one before, that we do not take into account the gradients in the temperature T, meaning that we assume the whole cell to operate on isothermal conditions.

4.7.2 Algorithm Flowchart

The flow chart of the algorithm used is presented below:

1. Initialization of Subproblem Geometrical setup, Physical and numerical constants definition (iteration counter, q, maximum number of iterations etc), assign initial guess for γ.

2. Possibly apply density filter to γ

3. Solve for the current γ the coupled PDEs by FEM in Comsol and acquire the solution $(V(\gamma))$.

4. Compute the objective functionΦ_{obj}
5. Compute the sensitivities $\frac{\partial \Phi_{obj}}{\partial \gamma}$ by the adjoint method, formulating appropriately the problem in Comsol
6. Update design variable by calling the relevant MMA routines.
7. check for convergence. If maximum number of iterations not reached or if convergence not accomplished return to 2 and increase iteration counter by 1
8. Post processing.

4.7.3 Stabilization-Filtering-Convergence Criterion-Starting Conditions

No stabilization method was used, nor for the fluid flow nor for the convective mass transfer. For the fluid flow this was not an issue, since the speeds in our implementation are fairly low, and the LBB criterion is satisfied. However, the absence of stablization technique for the convective transport, means that a very refined mesh had to be used and since our computational resources were limited, in many circumstances we witnessed instabilities when treating subproblems 2 and 3.
On occasions we applied a density filter as described in [43] and [34] because at some instances the results were giving an impression of slight mesh dependance. However, because of the non-linearities of the problem it did appear to pay off usinf the filtering and so it was not a general treatment.
The convergence criterion to change to another value q defining the linearity of the interpolation as already explained, in the process of the algorithm was the the absolute value of the difference between two successive γ values to be less than 10^{-3}. The maximum iteration number was set to 500.
In all subproblems, the codes demonstrated robustness in the initial conditions, i.e. for diffferent initial conditions for the original guess for the design parameter γ the same result was always produced.

Chapter 5

Topology Optimization Results and Discussion

The main focus of this discussion, is out of the three subproblems earlier set, subproblem 1. The reason for this is that the scripts for this case exhibit both stability and very good convergence for all the range of our design parameters on the one hand. On the other hand, the level of complexity of the models involved in subproblems 2 and 3 resulted in the models finalization and fine tuning only near the end of this work. Not to mention that the complexity and the non-linearity, invoked many instabilities whose partial alleviation was achieved also but recently. So only a very few indicative cases are available for the moment. However, the exploration of the full scan of the design domain and a quantitative analysis of all subproblems is an on going process that we wish to conclude soon after the completion of this work.

5.1 Subproblem 1

In figure 5.1 we see a typical example of the distribution in our design domain This image was generated after a 150 iterations.

As we are able to observe in this figure, the contrast between values of 0, i.e. interconnect material and values of 1, i.e. fluid or anode/anode support layer, is ideal and almost no grey areas appear with values in-between. Next, we take a look at the potential distribution corresponding to the same parameters and design domain.

In the first place, in accordance to the the models developed in the theory chapter, we see that in the areas where interconnect material is introduced by the topology optimization, the potential value reduces to 0 while in the anode/anode

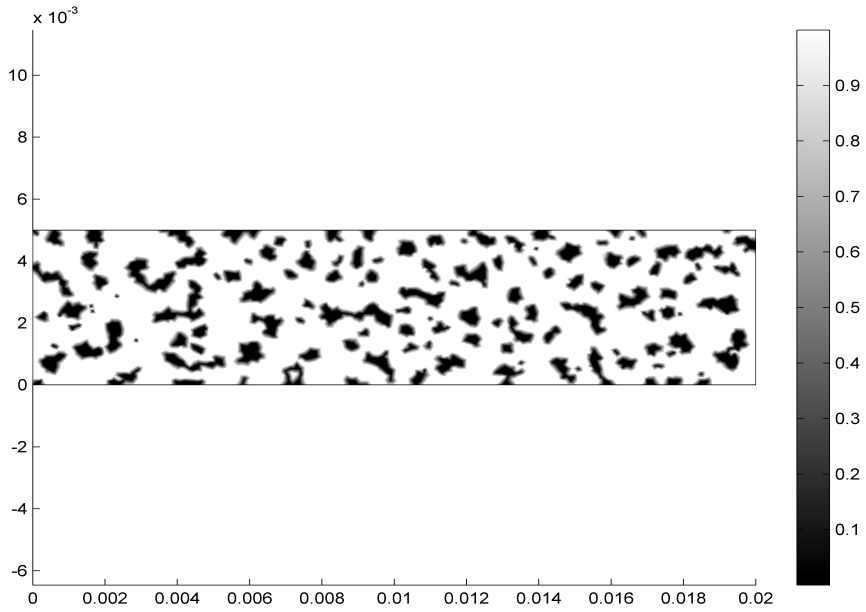

Figure 5.1: γ distribution in design domain, $V_{cell} = 0.8V$, $Uo_{in} = 0.5\frac{m}{s}$, $\sigma_{ic} = 10^3\frac{S}{m}$

support region it accomplishes negative values. It is more illustrative, if we look at the same values in a $3D$ height representation, fig.5.3

Furthermore, we see that for this setting, the minimum value of the potential is $-0.036V$.

Crucial to the accuracy of our results is the sign of the difference $V_{net} = V_N - V_{cell} + \Phi$ to always remain constant, fig.5.4. Indeed, this is always true, since the values of Φ are in general one to two orders of magnitude smaller than $V_N - V_{cell}$.

Since the fluctuations in V_{net} are minute, the current density,in $\frac{A}{m^2}$, of the domain with $\gamma = 1$ appears consequently more or less uniform in the anode/anode support, fig.5.5. The maximum value computed here is $1.5\frac{A}{cm^2}$, which obviously is over estimated compared to real life values.

The integral of the current density over this domain must be equal to the current density of the current going through the interconnect as the conservation of charge dictates. Since the area available for current collection is smaller the (negative) current through it must be significantly larger. Indeed, this is true, and more specifically as we see in 5.6 almost an order of magnitude larger.

We now take on the fluidic part of our problem. In the first place the velocity distribution looks like this:

The maximum value of the velocity in the domain is $3.96042\frac{m}{s}$. Calculating

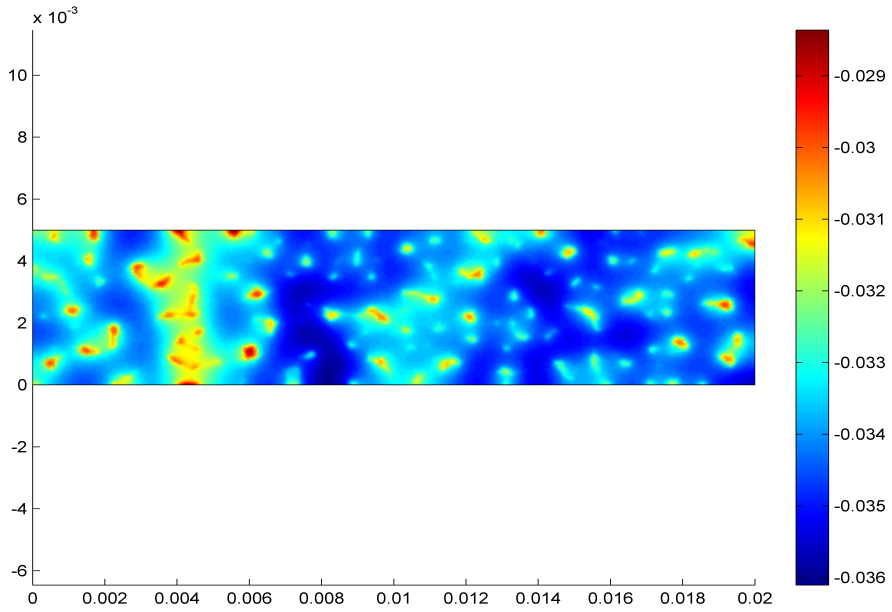

Figure 5.2: Φ distribution in design domain, $V_{cell} = 0.8V$, $Uo_{in} = 0.5\frac{m}{s}$, $\sigma_{ic} = 10^3\frac{S}{m}$

the Reynolds number of the flow, we find that $Re = 0.6081$. Hence we can say that we are not so far away form our original argument that the fluid flow can be considered as a Stokes flow. We can also take a look at the pressure drop that takes place as we move with the fuel gas in a plot where we are omitting the γ so as to reveal the slight change fig.5.8 and a contour plot fig5.9.

Turning our attention to the energy calculations, as expected by the preceded analytical calculations in the theoretical investigations chapter, the orders of magnitude of the fluid dissipated power, the joule heating of the interconnect and the power generated from the MEA having subtracted all the included in each subproblem losses, are quite different. This is evident in the following typical examples of the same set of parameters.

In fig.5.10 we observe that the power given by the cell, is around $12\frac{kW}{m^2} = 1.2\frac{W}{cm^2}$. In fig.5.11 we depict the actual value that is being minimized during the optimization process, i.e. the negative of $P_{gen} - P_{fluid} - P_{jhic}$. The close proximity between absolute values of P_{gen} and P_{net} is due to the lower values of the other two losses included, i.e. P_{fluid} fig.5.12 and P_{jhic}, fig5.13.

In these figures we see that the order of magnitude of P_{fluid} is $0.01\frac{W}{cm^2}$ and that of the joule heating of the interconnect material is $0.36\frac{W}{cm^2}$
In order to demonstrate how the iteration process evolves, we show in figure 5.14, some characteristic instances for a slightly different set of parameters. The

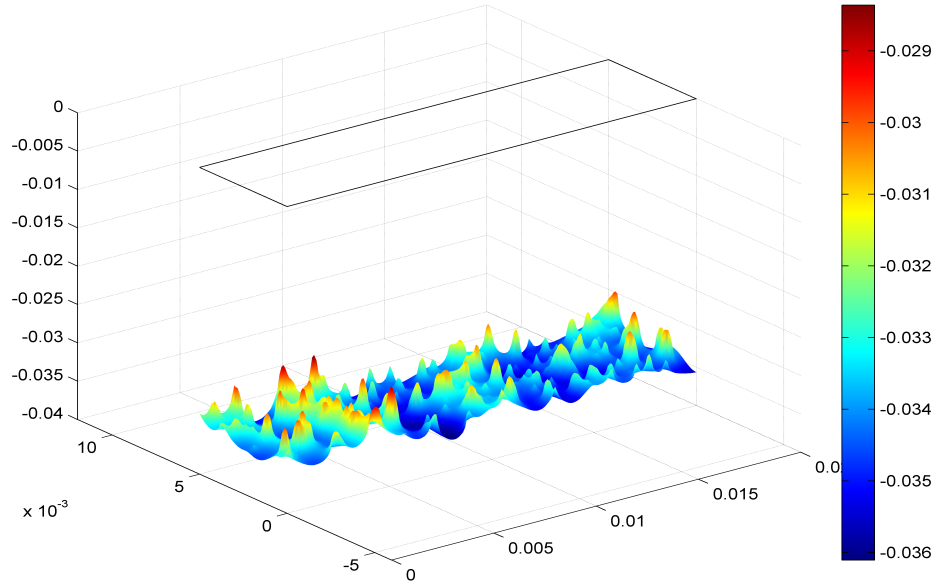

Figure 5.3: Φ height representation of distribution in design domain, $V_{cell} = 0.8V$, $Uo_{in} = 0.5\frac{m}{s}$, $\sigma_{ic} = 10^3\frac{S}{m}$

satisfaction of convergence criteria for the vector q used, gave 163 iterations. It is apparent from these figures that progressively, as q changes, the gray areas are successfully giving their position to more discrete ones.

In fig.5.15 we vary the conductivity of the interconnect and the potential of the cell for a fixed $Uo_{in} = 0.25\frac{m}{s}$. An obvious observations which is also a general trend of our findings is that the higher the used conductivity the thinner the areas of interconnect material grow. However, we are able to see the distinct difference between $V_{cell} = 0.7$ and $V_{cell} = 0.8$. The later one assists the better contrast between regions of solid and open space, while the former has a tension for giving more homogenized and grey areas. In any case, this tendency concurs with our physical intuition that the the larger the conductivity of the interconnect material, the lesser material is needed to give passage to the same as before charge per area per time.

5.2 Subproblems 2 and 3

Subproblem 2, was actually built as an intermediate step for subproblem 3. Qualitatively the solutions they produce are quite similar so we proceed in presenting directly some indicative results from the simulations performed on subproblem 3.

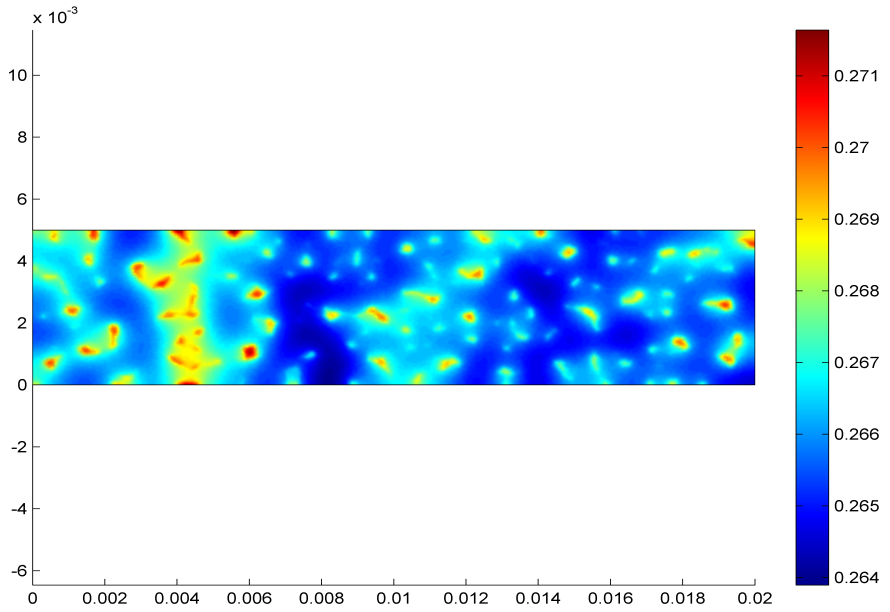

Figure 5.4: V_{net} distribution in design domain, $V_{cell} = 0.8V$, $Uo_{in} = 0.5\frac{m}{s}$, $\sigma_{ic} = 10^3\frac{S}{m}$

In fig.5.16 we see the γ distribution produced after500 iterations, for the following set of parameters: $V_{cell} = 0.8V$, $Uo_{in} = 1\frac{m}{s}$, $\sigma_{ic} = 10^6\frac{S}{m}$

A general observed tendency, was that the convergence for these problems benefited from increase of σ_{ic}. Returning to fig.5.16 we see that by comparison with the previously observed trend, the high interconnect electronic conductivity does not result in an as scattered pattern of small structures, but rather gives rise to thicker and more rounded structures. Furthermore, we see that the there are gray areas and hence the discretization could probably be enhanced by the application of the relevant filter.

By inspection of the potential hight representations fig. 5.18 and 5.19 we see that in the case of subproblem 3 a slightly lower potential is achieved. This is totally what we would expect from just observing at the γ distribution, in combination with the theoretical results and the comments we made on the effect of the different terms entering the objective function, according to which increasing the separation between the interconnect pillars would deepen the second order potential drop in area 2. The values we observe are $-3.5 \cdot 10^{-3}$ for subproblem 1 and $-4.5 \cdot 10^{-3}$ for subproblem 3.

Turning our attention to fig.5.20 and 5.21, we see how the current distribution increases as we go downstream. This is also something expected from the expression eq.4.19. The denominator R_p decreases as water vapor is produced

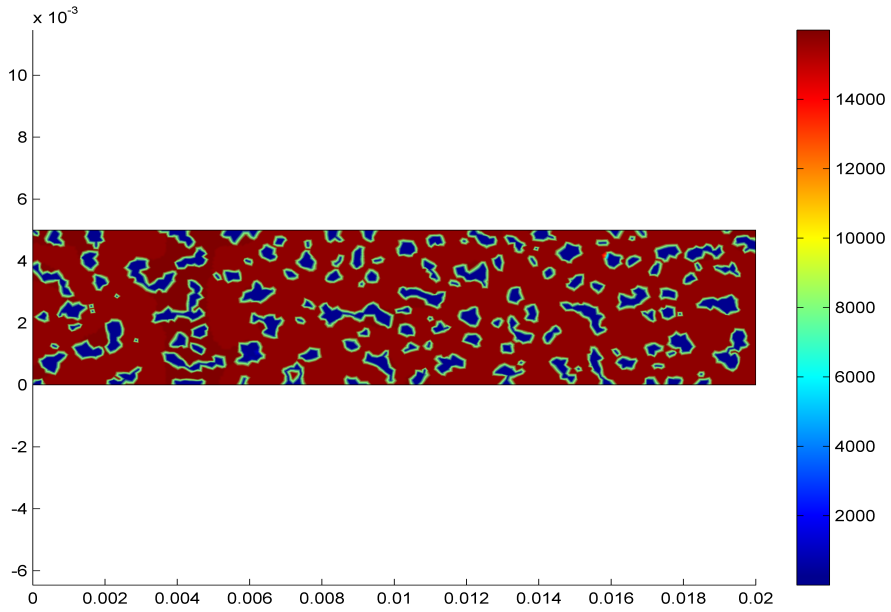

Figure 5.5: Anode/anode support current density distribution in design domain, $V_{cell} = 0.8V$, $Uo_{in} = 0.5\frac{m}{s}$, $\sigma_{ic} = 10^3\frac{S}{m}$

downstream and hence this results in an increase in the current.

This higher current, has as a natural consequence the increase, of the net power we are able to extract from the cell as indicated in figures 5.22 and 5.23 where the negative net power in subproblem 3 is about $0.2\frac{W}{cm^2}$ more than the one in subproblem 3. Next, we demonstrate the concentration fields calculated in our simulations. In fig.5.24 we see the slight variation in the hydrogen concentration from the fixed at the inlet value of $11.23\frac{mol}{m^3}$ to $10.7\frac{mol}{m^3}$ at the outlet. In fig.5.25 we see the same figure multiplied by γ

In fig.5.26 we observe the increase of the mass fraction of water vapor downstream, from 0.2 at the inlet to 0.36 at the outlet. In fig.5.27 we show the molar fraction of H_2 ranging from 0.9727 at the inlet to 0.9323 at the outlet.

The reaction rate in $\frac{mol}{m^2 \cdot s}$, is shown in fig.5.28

We have stressed in our theoretical derivations and in the numerical simulations' setup that the density is variable in the design domain, depending on the variable concentrations of H_2 and H_2O. In fig.5.29 we see the increase from the inlet value of $0.0278\frac{kg}{m^3}$ to the outlet value of $0.0334\frac{kg}{m^3}$. This increase of 20.14% is due to the steam production and participation with a higher molar fraction in the calculation of the outlet compared to the inlet one.

To conclude this qualitative analysis, we show in fig. the variation in the cell of the conversion and diffusion losses.

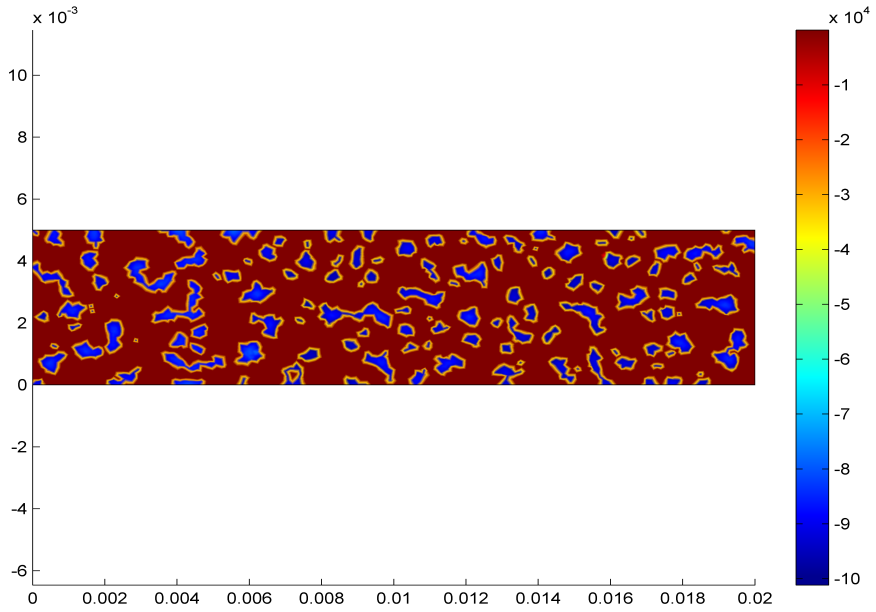

Figure 5.6: Current collector current density distribution in design domain, $V_{cell} = 0.8V$, $Uo_{in} = 0.5\frac{m}{s}$, $\sigma_{ic} = 10^3\frac{S}{m}$

By inspection it is evident that the conversion losses are almost two orders of magnitude greater and hence more important in our calculations.

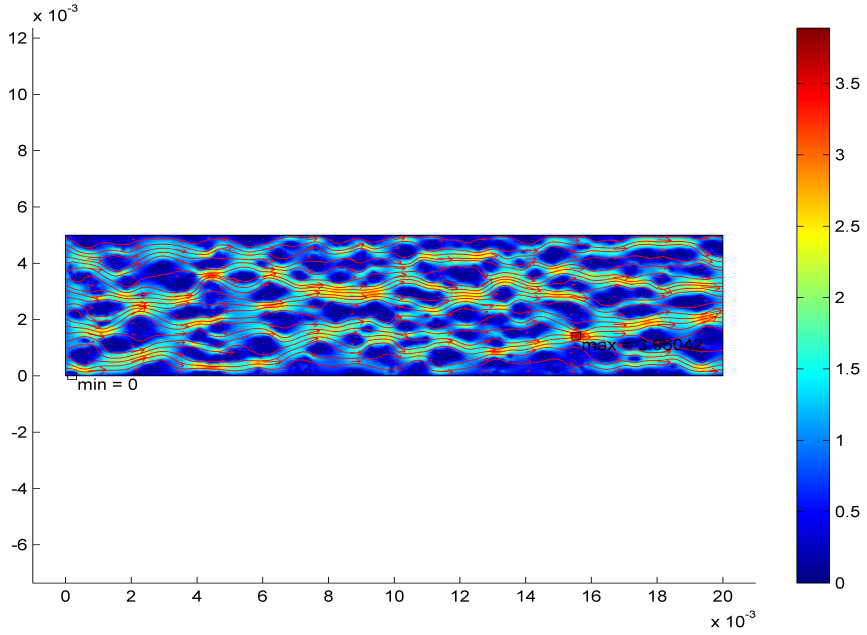

Figure 5.7: Velocity distribution with stream lines in design domain, $V_{cell} = 0.8V$, $Uo_{in} = 0.5\frac{m}{s}$, $\sigma_{ic} = 10^3\frac{S}{m}$

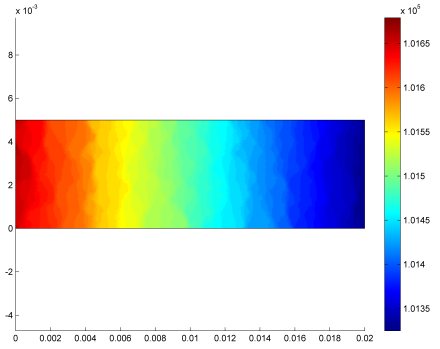

Figure 5.8: Pressure distribution in design domain, $V_{cell} = 0.8V$, $Uo_{in} = 0.5\frac{m}{s}$, $\sigma_{ic} = 10^3\frac{S}{m}$

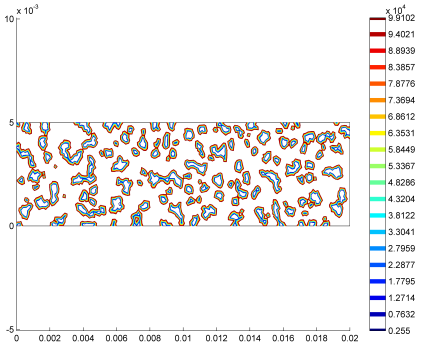

Figure 5.9: Pressure contours in design domain, $V_{cell} = 0.8V$, $Uo_{in} = 0.5\frac{m}{s}$, $\sigma_{ic} = 10^3\frac{S}{m}$

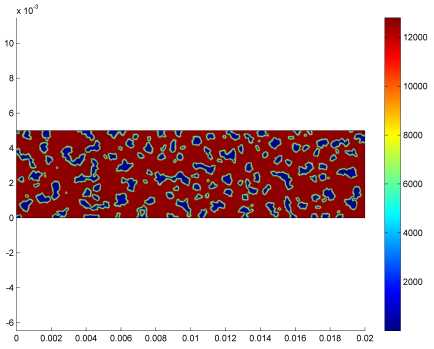

Figure 5.10: P_{gen} distribution in design domain, $V_{cell} = 0.8V$, $Uo_{in} = 0.5\frac{m}{s}$, $\sigma_{ic} = 10^3\frac{S}{m}$

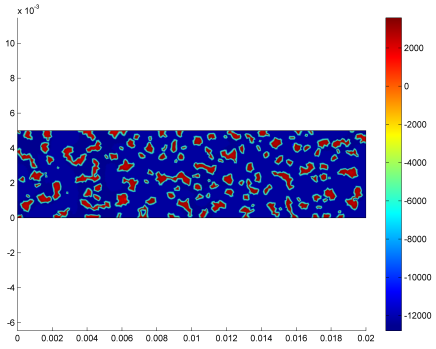

Figure 5.11: $-P_{net}$ distribution in design domain, $V_{cell} = 0.8V$, $Uo_{in} = 0.5\frac{m}{s}$, $\sigma_{ic} = 10^3\frac{S}{m}$

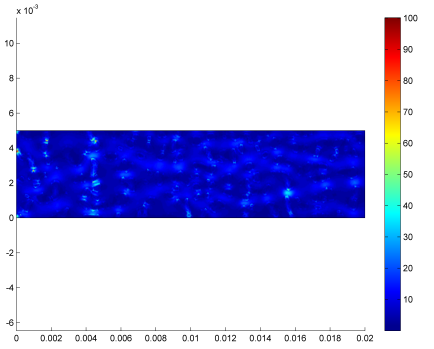

Figure 5.12: Fluid dissipation,P_{fluid}, distribution in design domain, $V_{cell} = 0.8V$, $Uo_{in} = 0.5\frac{m}{s}$, $\sigma_{ic} = 10^3\frac{S}{m}$

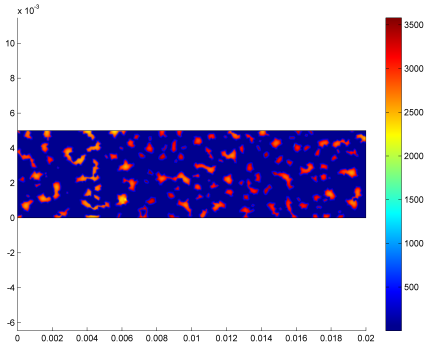

Figure 5.13: Current collector joule heating P_{jhic}, in design domain, $V_{cell} = 0.8V$, $Uo_{in} = 0.5\frac{m}{s}$, $\sigma_{ic} = 10^3\frac{S}{m}$

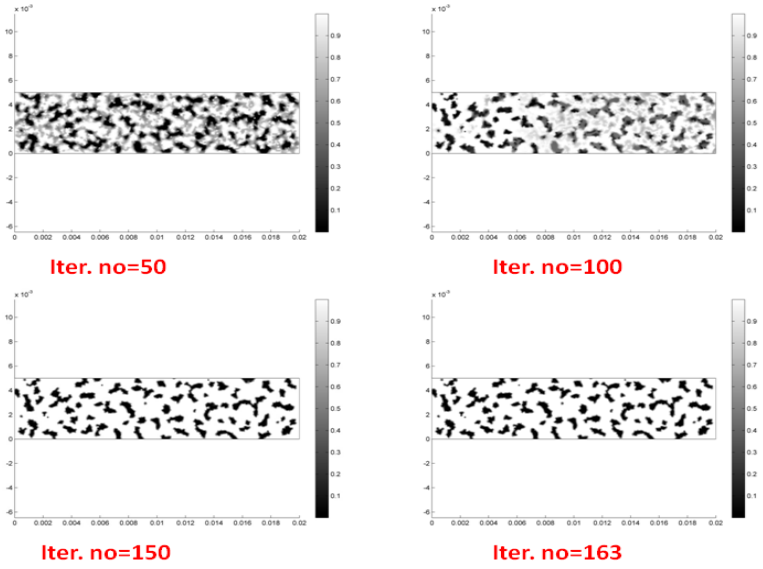

Figure 5.14: γ after, 50, 100, 150 and finally 163 iterations, $V_{cell} = 0.7V$, $Uo_{in} = 0.5\frac{m}{s}$, $\sigma_{ic} = 10^3 \frac{S}{m}$

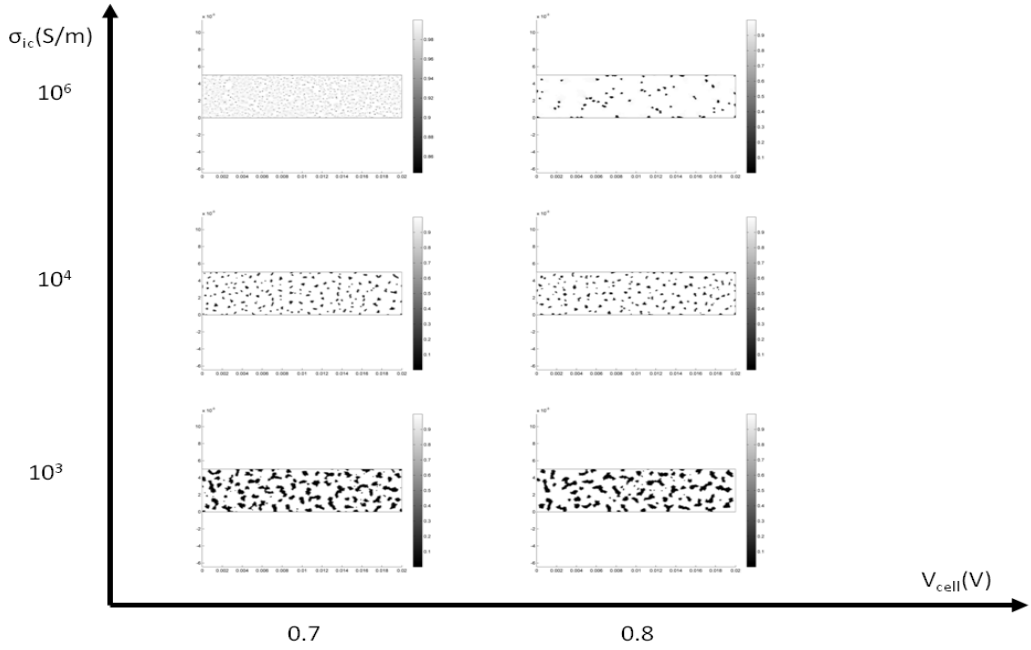

Figure 5.15: Variation of γ with V_{cell} and σ_{ic} for fixed $Uo_{in} = 0.25\frac{m}{s}$

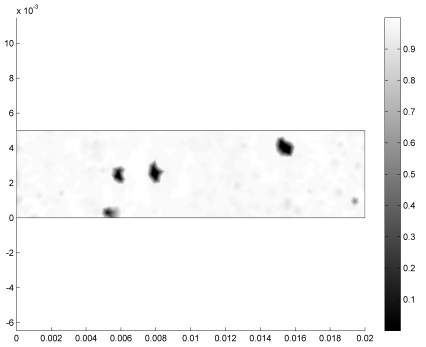

Figure 5.16: γ distribution in design domain for subproblem 3, $V_{cell} = 0.8V$, $Uo_{in} = 1\frac{m}{s}$, $\sigma_{ic} = 10^6\frac{S}{m}$

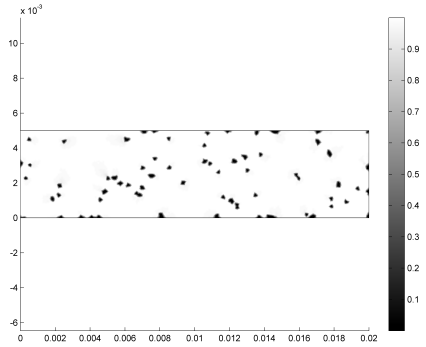

Figure 5.17: γ distribution in design domain for subproblem 1, $V_{cell} = 0.8V$, $Uo_{in} = 1\frac{m}{s}$, $\sigma_{ic} = 10^6\frac{S}{m}$

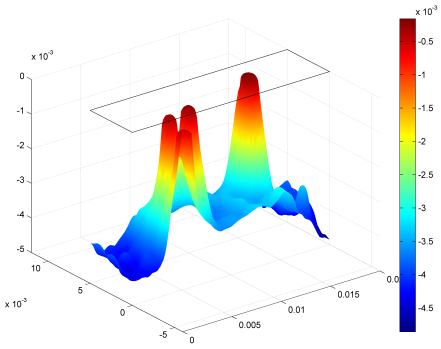

Figure 5.18: height representation of potential Φ in design domain for subproblem 3, $V_{cell} = 0.8V$, $Uo_{in} = 1\frac{m}{s}$, $\sigma_{ic} = 10^6\frac{S}{m}$

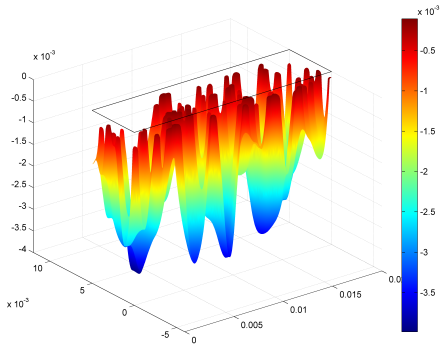

Figure 5.19: height representation of potential Φ in design domain for subproblem 1, $V_{cell} = 0.8V$, $Uo_{in} = 1\frac{m}{s}$, $\sigma_{ic} = 10^6\frac{S}{m}$

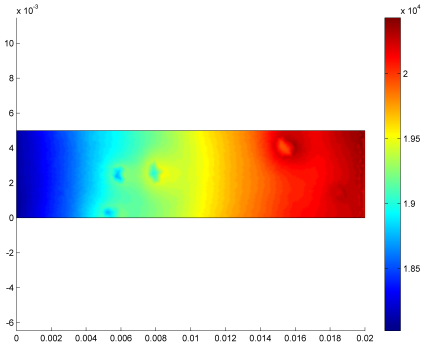

Figure 5.20: Area 2 current distribution in design domain for subproblem 3, $V_{cell} = 0.8V$, $Uo_{in} = 1\frac{m}{s}$, $\sigma_{ic} = 10^6\frac{S}{m}$

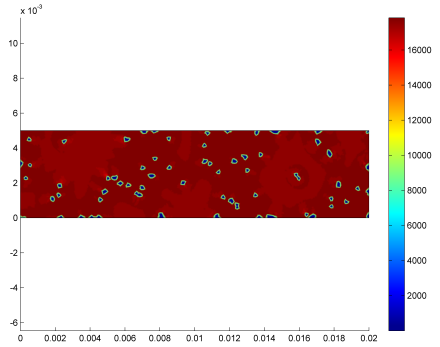

Figure 5.21: Area 2 current distribution in design domain for subproblem 1, $V_{cell} = 0.8V$, $Uo_{in} = 1\frac{m}{s}$, $\sigma_{ic} = 10^6\frac{S}{m}$

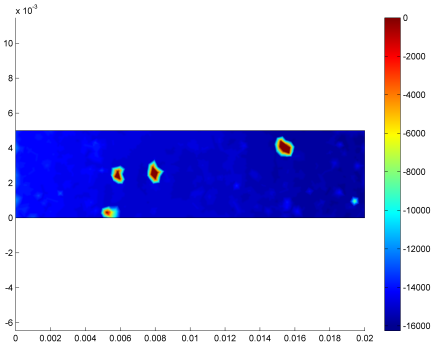

Figure 5.22: Area 2 net power distribution in design domain for subproblem 3, $V_{cell} = 0.8V$, $Uo_{in} = 1\frac{m}{s}$, $\sigma_{ic} = 10^6 \frac{S}{m}$

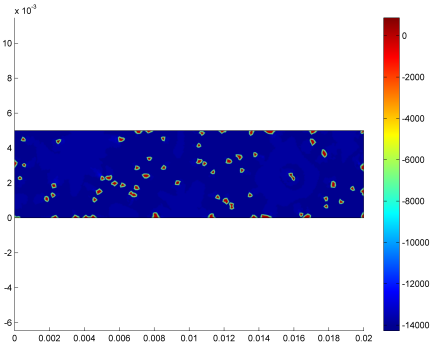

Figure 5.23: Area 2 net power distribution in design domain for subproblem 1, $V_{cell} = 0.8V$, $Uo_{in} = 1\frac{m}{s}$, $\sigma_{ic} = 10^6 \frac{S}{m}$

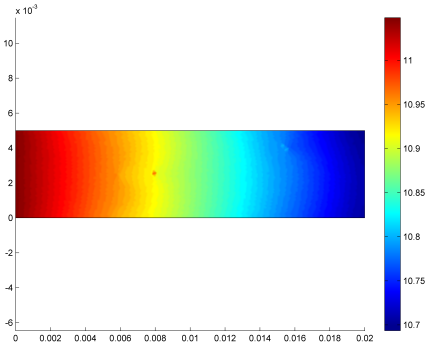

Figure 5.24: c_{H_2} distribution in gas channel design domain for subproblem 3, $V_{cell} = 0.8V$, $Uo_{in} = 1\frac{m}{s}$, $\sigma_{ic} = 10^6 \frac{S}{m}$

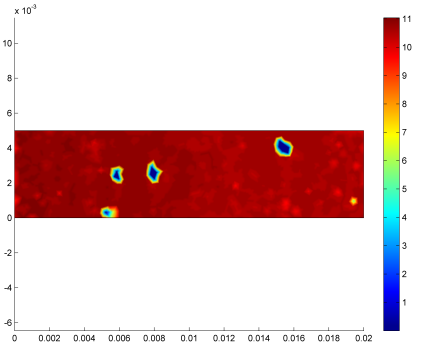

Figure 5.25: c_{H_2} distribution in gas channel design domain for subproblem 1 with embedded γ, $V_{cell} = 0.8V$, $Uo_{in} = 1\frac{m}{s}$, $\sigma_{ic} = 10^6 \frac{S}{m}$

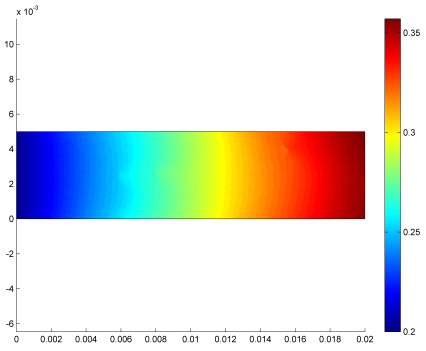

Figure 5.26: H_2O mass fraction distribution in gas channel design domain for subproblem 3, $V_{cell} = 0.8V$, $Uo_{in} = 1\frac{m}{s}$, $\sigma_{ic} = 10^6\frac{S}{m}$

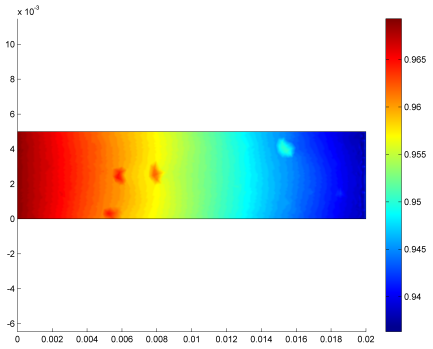

Figure 5.27: H_2 distribution in anode design domain for subproblem 3, $V_{cell} = 0.8V$, $Uo_{in} = 1\frac{m}{s}$, $\sigma_{ic} = 10^6\frac{S}{m}$

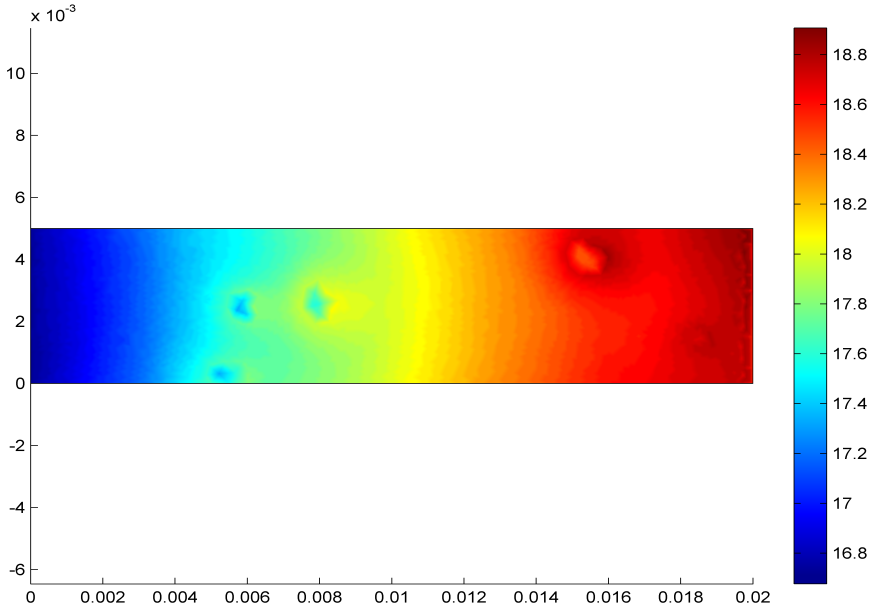

Figure 5.28: H_2O reaction rate distribution in $\frac{mol}{m^2 \cdot s}$, $V_{cell} = 0.8V$, $Uo_{in} = 1.0\frac{m}{s}$, $\sigma_{ic} = 10^6\frac{S}{m}$

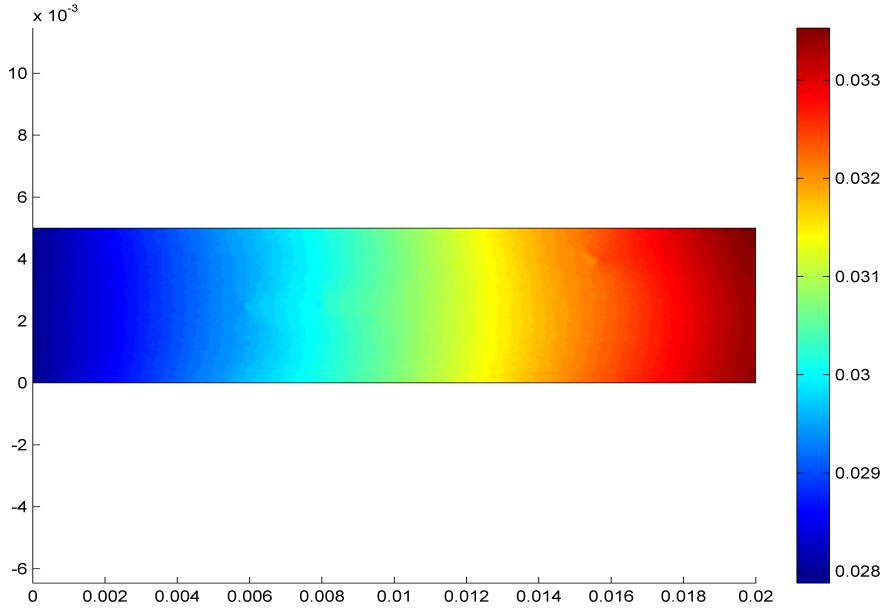

Figure 5.29: Density distribution in $\frac{kg}{m^3}$, $V_{cell} = 0.8V$, $Uo_{in} = 1.0\frac{m}{s}$, $\sigma_{ic} = 10^6 \frac{S}{m}$

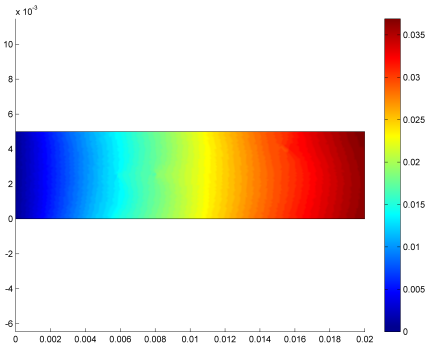

Figure 5.30: Conversion potential loss distribution in gas channel design domain for subproblem 3, $V_{cell} = 0.8V$, $Uo_{in} = 1\frac{m}{s}$, $\sigma_{ic} = 10^6 \frac{S}{m}$

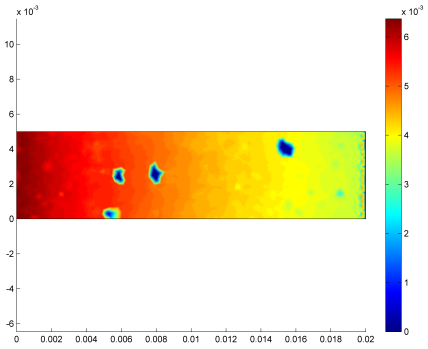

Figure 5.31: Diffusion potential loss distribution in anode design domain for subproblem 3, $V_{cell} = 0.8V$, $Uo_{in} = 1\frac{m}{s}$, $\sigma_{ic} = 10^6 \frac{S}{m}$

Chapter 6

Homogenization

6.1 Overview

The goal in this work is to define optimal micro-structures for a Solid Oxide Fuel Cell Cathode through modeling. This modeling relies on homogenization for the derivation of the up-scaled equation describing the diffusion of oxygen vacancies in the cathode under steady state conditions. Solution of this equation leads to correlation of the Area Specific Resistance of the cathode to the geometric features of the micro-structure such as the porosity and the area available for oxygen surface exchange reaction and the tortuosity. We focus on studying four geometries that are of specific interest due to their ease of manufacturing, i.e. a cylinder, inverse opal, sphere and inverse sphere. The structures radius, for given specific material and micro-cell length scale proves to be the important parameter of our problem. Thus, it is natural to investigate the effect of sweeping through different radii on the electrodes resistance for each one of the selected structures. Calculation of the tortuosity is achieved by means of a relevant expression, emanating from the performed homogenization, while the other two structural-geometric elements, i.e. porosity and reaction available area can be directly computed, either during simulation or analytically. Combination of theoretical and computational results will reveal the optimum geometry exhibiting the lowest non-dimensional resistance among the ones studied.

6.2 Modeling of SOFC Cathodes-Cathode micro-structure manufacturing and control

When our interest is focused on an electrode, these loses mainly come from charge transfer processes, both electronic and ionic, gas diffusion, as well and chemical

reactions and they are quantified by the notion of generalized resistance conveniently defined on a per surface basis as Area Specific Resistance (R_{chem}). The minimization of R_{chem} through modeling for a Solid Oxide Fuel Cell (SOFC) cathode under certain assumptions is the primary goal of this work. Many different mechanisms have been proposed as governing the oxygen cathode reaction [52], [53]. In our analysis we assume that the bulk pathway of oxygen ion transport is the dominant one as oxygen absorption and inclusion and bulk diffusion are facile. Out of the components of which any hydrogen/oxygen fuel cell consists of, it is known that the rate limitations come from the cathode and that it is the main origin of the activation overpotential [54], due to the high oxygen reduction activation energy. These cathodic losses can reach a fraction of up to 65% in some cases of the total losses measured in a SOFC [55]. For material such as LSCF it has been reported that the gas diffusion influence on the overall polarization resistance of the cathode is minimal [56], [57] and that the charge transfer process in a LSCF/GDO interface is also facile and favored by reducing temperatures [57]. In this context, we focus our study on the minimization of the Area Specific Resistance due to the ionic solid state diffusion and the chemical exchange mechanism alone, i.e. not including the interfacial charge transfer at the electrodes boundaries for a SOFC cathode model with no gas diffusion limitations. Some of the numerous modeling attempts of SOFC cathodes published earlier are summarized in [58]. According to [53] the different modeling approaches can be classified within the following categories depending on the level of sophistication and length-scale utilized: continuum electrode, many particles, local current density distributions and chemical kinetics. Another more general categorization in micro- [59] and macro-models [5]-[60] is proposed in [58]. Modeling validation is often done through comparison with experiments and Electrochemical Impedance Spectroscopy (IES) results. Combination of experimental data and macro-modeling is also very often since the former can provide the values of properties necessitated by the macro-models or direct use of theoretical results derived through modeling are combined with experiments as in [61]. Another classification for the models used for simulations of SOFC cathodes emanates from the level of general complexity and whether the totality of electrochemical and physical processes is involved or simplified assumptions are taken into consideration regarding some of them as well as whether their target is simulating the steady state regime or the transient one. Accounting for all or some of the steps that the oxygen reduction reaction consists of and determining the rate limiting one in each case, is another way to distinguish between modeling approaches. The advancement in computational techniques and power has rendered possible the transition from simplified analytical solutions coming from one dimensional models to resolution of two [62] or even full three dimensional ones [63] via commercial packages or in house codes. Research regarding manufactur-

ing energy conversion systems in general does not exclusively rely anymore on the conventional approach of inventing new materials with outstanding properties in a pure chemical sense, but has also been boosted by incorporating micro-and nano-structured materials. Thus, methods have been proposed [64]-[65] and [66], [67] that lead to control of the morphology on the micron scale.

6.3 Homogenization on Fuel Cell modeling

The phenomena involved in the study of fuel cells electrodes concern flows of gases or liquids through pores as well as conduction of electrons and ions through complex networks of appropriately interconnected solid phases. In this sense, it is natural that the shaping of the micro-structure is of ultimate importance to the observed electrode properties and it is also expected that the material of which the electrode consists, exhibits heterogeneity in these properties. Approaching this problem from a theoretical point of view, one method to make a transition from equations describing the problem on a micron scale to a macroscopic description is to resort to Volume Averaging. This is technique is used in [68] for deriving effective electronic conductivity and gas effective diffusivity for a model of a SOFC anode composed of the cermet Ni/YSZ. Another more general, theoretically rigorous and versatile alternative is Homogenization. Homogenization is a frequently used analytical tool when two distinct length scales are present in a problem. It is a methodology originally designed to account for periodic distribution of heterogeneities but can also be extended to the non periodic cases. Based on the assumptions of periodicity and of approaching the solution by an asymptotic expansion of the function of interest e.g. concentration of ions in the case when the studied property is ionic conductivity, it comes up with effective properties for a homogenized material. In this way, homogenization also predicts how the macroscopic properties are affected by the micro-structure [28]. It has been used lately in modeling the behavior of battery electrodes [69]. Along the same lines homogenization of the Poisson-Nerst-Plank equations combined with Stokes flow can be found in [70]. The only other attempt to apply homogenization on fuel cells can be found in [71] where homogenization is used in modeling the pore geometry of a cathode in PEM fuel cells. Consequently, to the best of our knowledge, this is the first time that homogenization is applied in modeling of a SOFC. In the papers [5], [72] a one dimensional model for a SOFC cathode was derived. In the steady state, solution of the linearized ac response of this model leads to the calculation of the penetration depth: the depth beyond which the electrode is not any more significantly reduced. In addition, it leads to the derivation of an expression for R_{chem} whose chemical and bulk ionic diffusive mechanisms are shown to be the dominating ones for materials like LSCF. This expression reveals dependence of R_{chem} on the length scale of the micro-structure and the

micro-structures geometry. The homogenization analysis given in appendix A, assuming the electrode to be a porous medium with considerable scale separation, provides us with an upscaled equation for the ionic diffusion identical to the one derived by Adler in the afore mentioned model, subsequently leading to the same expression for the Area Specific Resistance as the one provided by Adler. In the same time, upscaling this ionic diffusion equation does not only provide the R_{chem} expression but on top of that, it provides an expression for the calculation of the necessary solid phase tortuosity which is in general very hard to be calculated either computationally or experimentally. The calculation of the tortuosity, necessitated for the R_{chem} calculation, is performed analytically and confirmed computationally for the cylinder and inverse cylinder case and computationally for all other cases using the commercial package Comsol. The purpose of our work is to apply the mathematical rigorousness of homogenization securing by construction of the method that our model incorporates the effects of the micro-scale, benefiting from distinguishing between time scales present in the problem at hand and then calculate for different distinct but fundamental micro-geometries the dimensionless $\widetilde{R}_{chem}$ as a function of the radius of these geometries.

Chapter 7

Homogenization Modeling and Methodology

7.1 Model Description/Simulation setup

7.1.1 Adler's model

The model proposed by Adler [5], concerns the symmetric cell geometry depicted in fig. 7.1 described as follows. The cell consists of an electrolyte layer and two identical oxygen electrodes, having a thickness of L_{el} and L respectively. An intermediate gas layer separates the electrodes surfaces and the perfectly mixed two component gas (oxygen and a diluent gas) on both sides. The thickness of this boundary layer is L_{bl}. The main interfacial reaction mechanisms involved in a typical electrode like the one under discussion are the following:

- charge-transfer of oxygen ion vacancies across the mixed conductor/electrolyte interface,
- charge-transfer of electrons across the current-collector/mixed conductor interface, and
- the chemical exchange of oxygen at the gas/mixed-conductor interface.

From these three, we concentrate on investigating the cells resistance due to the oxygen exchange alone. Furthermore, the model is derived on the basis of the following assumptions:

- Fast gas diffusion. This means that the oxygen concentration can be considered constant everywhere in the electrode.

- Conductivity of electrode is infinite resulting in uniform electrochemical potential of electrons in the mixed conductor.
- Oxygen surface exchange is slow.

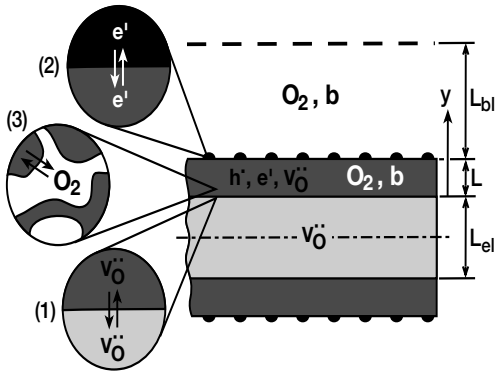

Figure 7.1: Geometry of model cited in [5]

The transport phenomena present in the porous electrode material are dependent on a series of geometric and reaction related features such as: the surface reaction rate r, the porosity ε, the average internal surface area α, and the solid-phase tortuosity τ. The porosity is the volume fraction available for gas diffusion in the material; the internal surface area is the specific area available for reaction; while the tortuosity is a measure quantifying how tortuous the trajectory followed by a particle is, e.g. in our case by an oxygen anion. According to [5], the unsteady diffusion reaction equation for the oxygen vacancies in the bulk is given by:

$$(1-\varepsilon)\partial_t c_V = \frac{1-\varepsilon}{\tau} D_V \partial_y^2 c_V - \alpha r \tag{7.1}$$

Where, c_V is the vacancy concentration and D_V is the vacancy diffusion coefficient. The surface reaction rate is proportional to c_V according to:

$$r = r_o(\alpha_f + \alpha b) A \frac{c_V}{c_V^*} \tag{7.2}$$

Where, r_o is the exchange neutral flux density (in analogy to exchange-current density), α_f and α_f are dimensionless kinetic parameters that depend on the specific mechanism of the surface chemical exchange reaction; A is a thermodynamic factor and c_V^* refers to some reference concentration value. Equation 7.1, first in

a series of a six equations followed by six relevant boundary conditions, allowed Adler et al. to solve for the vacancies, and gas concentrations for the fuel cell of the system described above, in one dimension which is indicated by the y axis in fig. 7.1. A time dependent potential excitation was supposed for the general case, which in the steady state regime, i.e. $\omega = 0$, revealed the nature of two important features of the problem. In the first place, the non-charge-transfer resistance (Area Specific Resistance due to the chemical mechanism) for a porous single-phase mixed conducting cathode reduces to:

$$R_{chem} = \frac{RT}{2F^2}\sqrt{\frac{\tau}{(1-\varepsilon)\alpha c_V D_V r_o(\alpha_f + \alpha_b)}} \tag{7.3}$$

As seen from this last expression, the magnitude of the overall impedance equally depends on both surface reaction and solid state diffusion. Furthermore, increase of any of the factors on the denominator of equation 7.3 is beneficial for the electrode's performance. In addition, we notice that both a very fast reaction and a material with high ionic conductivity impose a decrease on the cell's resistance which is also physically and conceptually correct.

As a second consequence of the model's assumptions, comes the fact that the vacancies' concentration follows an exponential decay with the distance from the electrolyte-electrode interface. This active zone for oxygen reduction is described by a lengthscale called penetration length, δ_p which is defined as:

$$\delta p = \sqrt{\frac{c_V D_V(1-\varepsilon)}{\alpha} r_o(\alpha_f + \alpha_b)\tau} \tag{7.4}$$

We note that despite that in the afore-analyzed model the axis of interest for the conduction of oxygen vacancies is the y axis, in our theoretical and computational implementation we rename it as the z axis.

7.1.2 Derivation of model describing the SOFC cathode through Homogenization

We now proceed by describing the way in which homogenization can provide us with an analytical expression for the bulk diffusion of oxygen vacancies in the SOFC cathode. The cathode material is a porous medium which can be assumed to be of parallelepiped geometry without loss of generality, containing pore networks through which gas oxygen diffusion takes place and solid phases through which ions and electrons are conducted. It can be furthermore proved that by performing a periodic expansion in all directions in space of a fundamental cell, called the Y-cell, in which we can accurately describe in the micro-scale the property of our interest, in this case the diffusivity of oxygen vacancies, we can acquire an expression about the macroscopic description of the material's behavior with respect to the chosen property. In this way we make sure that

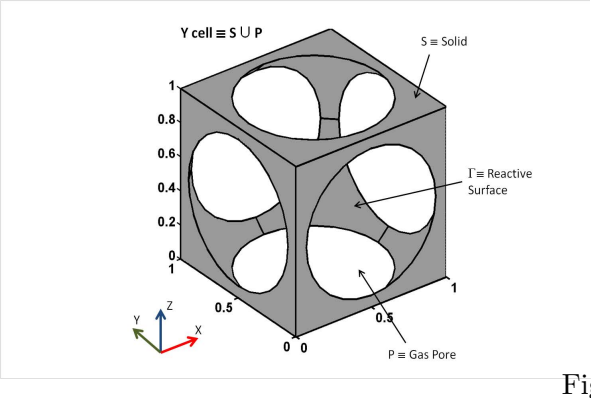

Figure 7.2: Y cell nomenclature

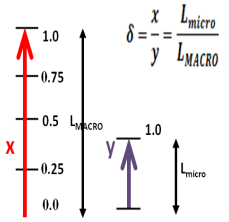

Figure 7.3: Macro and micro homogenization scaling

the heterogeneities spanned throughout our material are incorporated into the so called, "up-scaled" description. The Y-cell shown in fig. 7.2 consists for the sake of demonstrating the introduced concepts of a solid phase of inverse sphere structure and the complementary area inside it with respect to the unit cube is the pore available for gas diffusion. This cell consists of two components. The solid phase denoted by $\mathcal{S}$ and the gas phase (pore) denoted by $\mathcal{P}$. The (lateral) surface available for reaction is denoted by Γ. By the above, it is understood that periodic expansion of this unit cell in x, y, and z produces the bulk electrode material. As already mentioned, all the boundary conditions on this unit cell are periodic. By comparison of the model in Fig. 1 and our unit cell in Fig. 2a the direction of oxygen diffusion of interest is y in the first case and z in the second and this explains why the convection, diffusion reaction equation for the first contains derivatives with respect to y and the second one with respect to z. The argument regarding the periodic expansion of the Y-cell implies a coordinate scaling shown graphically in fig. 7.3 for one dimension, i.e. $\mathbf{y} = \frac{\mathbf{x}}{\delta}$ where y is the coordinate in the micro-scale characterized by the length L_{micro}, x is the coordinate at the macro-scale characterized by the length L_{MACRO}, and δ is the pore size. The homogenized limit is then achieved for $\delta \to 0$i.e. for high number of Y-cells as depicted in fig. 7.5-fig. 7.7, where a cross section of spherical solid phase is shown for simplicity. The shape of the geometry in the Y-cell though, can be more complicated without affecting the validity of the method. Another fundamental assumption is the fact that $\frac{\partial \delta}{\partial t}$ i.e. the pore size does not change with time for our analysis. As a natural consequence of our reasoning comes the fact that on the boundaries of our Y-cell, indicated as ∂Y periodic conditions are enforced.

Moving along and we focus on the local Y-cell $\widetilde{\mathbf{y}} \in Y = [0, L_{micro}]^3$ and write

the oxygen vacancies' convection, diffusion reaction equation namely: $\partial_t c_V = \nabla(D_V \nabla c_V)$ accompanied by a proper boundary condition, $D_V \nabla c_V \widehat{\nu} = k(c_V - c_{V\,ref})$. In the boundary condition equation $\widehat{\nu}$, see fig. 7.4, is the normal unit vector to the solid phase surface pointing from the surface to the pore and $c_{V\,ref}$) is a concentration reference value. In addition, we non-dimensionalize the above equations by using the transformations $\widetilde{\mathbf{x}} = L_{MACRO}\mathbf{x}$ and $\widetilde{\mathbf{y}} = L_{micro}\mathbf{y}$. In this way, we are dealing from now on with cubic cells of length one, i.e. $\widetilde{\mathbf{y}} \in \widetilde{Y} = [0,1]^3$ and we allow for the relevant time scales of the problem to come to the front. The basic ansatz of the method then states that the solution of the vacancies' concentration can be written in an asymptotic expansion of functions of both the micro and the macro scales as in: $c_V = c_{V0}(\mathbf{x},\mathbf{y}) + \delta c_{V1} + \delta^2 c_{V2}(\mathbf{x},\mathbf{y}) + O(\delta^3)$, which when substituted into the local, diffusion reaction equation and its boundary condition equation, properly differentiated and combined with time scaling arguments, concludes in revealing the sought bulk convection, diffusion reaction equation. All the above steps are explicitly and analytically presented in the Appendix of this paper.

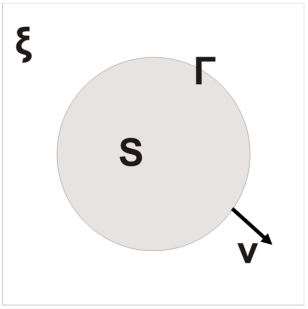

Figure 7.4: Fundamental cell and nomenclature in two dimensions, $\delta = 1$

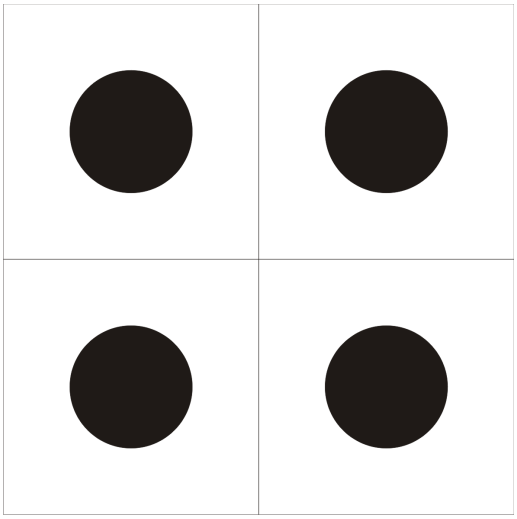

Figure 7.5: $\delta = 1/2$

Derivation of Adler's Formula via Homogenization We refer to literature sources [73],[69] for what follows. The model developed concerns the fuel cell system depicted in fig. 7.1 and the length scaling arguments are understood as presented in fig. 7.2 to fig. 7.7.

The equation that describes the diffusion of oxygen vacancies in the solid phase is described by:

$$\partial_t c_V - \nabla(D_V \nabla c_V = 0) \tag{7.5}$$

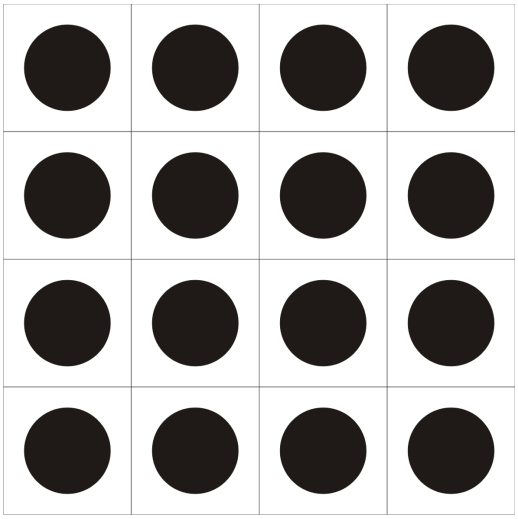

Figure 7.6: $\delta = 1/4$

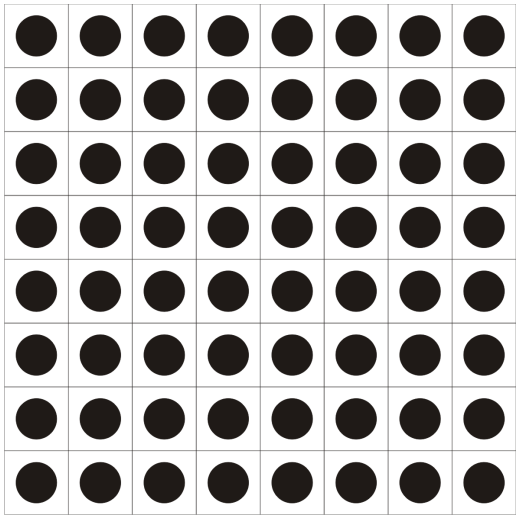

Figure 7.7: $\delta = 1/8$

Accompanied by the boundary condition:

$$D_V \nabla c_V \widehat{\nu} = k(c_V - c_{V_{ref}}) \tag{7.6}$$

In the above formulas c_V is the vacancy concentration, D_V is the coefficient of vacancy diffusion and $\widehat{\nu}$ is the unit normal vector to the interface of solid to gas phase on which the exchange of oxygen takes place, k is the oxygen exchange surface reaction rate (m/s), while $c_{V\,ref}$is a reference value.

For a typical pore size d the micro and macro scale in terms of homogenization theory are related as follows:

$$\mathbf{y} = \frac{\mathbf{x}}{\delta} \tag{7.7}$$

The length scales of the problem are related to the pore size as follows:

$$\delta = \frac{x}{y} = \frac{L_{micro}}{L_{MACRO}} \tag{7.8}$$

We will seek for solutions of this problem to be approximated by the following asymptotic expansion:

$$c_V = c_{V\,0}(\ \mathbf{x},\mathbf{y}) + \delta c_{V\,1} + \delta^2 c_{V\,2}(\ \mathbf{x},\mathbf{y}) + O(\delta^3) \tag{7.9}$$

Any function of x and y as in:

$$f(\ \mathbf{x},\mathbf{y}) = f(\mathbf{x}, \frac{\mathbf{x}}{\delta}) \tag{7.10}$$

, has derivatives which are given by:

$$\nabla f = \nabla_x f + \frac{1}{\delta} \nabla_y f \tag{7.11}$$

One can further make the assumption that the ability of the oxygen vacancies to diffuse is uniform throughout the cathode material, i.e.:

$$D_V = const \tag{7.12}$$

Before proceeding any further it would be convenient to put eq. 7.5and eq. 7.6 into dimensionless form with respect to the spatial coordinates. Applying scaling of the coordinates according to $\widetilde{\mathbf{x}} = L_{MACRO}\mathbf{x}$ where L_{MACRO} is the characteristic length scale of the macro system, we introduce the ion diffusion time scale:

$$T_V = \frac{{L^2}_{MACRO}}{D_V} \tag{7.13}$$

And the surface reaction time scale:

$$T_{RXN} = \frac{L_{MACRO}}{k} \tag{7.14}$$

If we further denote the gas diffusion time scale in the pore by T_G and the electronic one by T_e the assumptions of our model stated in the introduction take the form: $T_{RXN} \gg T_V \gg T_G \gg T_e$ Since the reaction is the slowest of all process involved we can write:

$$\frac{T_V}{T_{RXN}} = \frac{kL_{MACRO}}{D_V} \ll 1 \tag{7.15}$$

In dimensionless coordinate form we can then write:

$$T_V \partial_t c_V = \widetilde{\nabla}(D_V \widetilde{\nabla} c_V) \tag{7.16}$$

$$\widetilde{\nabla} c_V \widehat{\nu} = \frac{kL_{MACRO}}{D_V}(c_v - c_{V_{ref}}) \Rightarrow \widetilde{\nabla} c_V \widehat{\nu} = \frac{T_V}{T_{RXN}}(c_v - c_{V_{ref}}) \tag{7.17}$$

where $\widetilde{\nabla} f = \nabla_{\widetilde{x}} f + \frac{1}{\delta}\nabla_{\widetilde{y}} f$ means differentiation with respect to the new dimensionless coordinates. Applying now the differentiation rule once we get:

$$\widetilde{\nabla} c_V = \nabla_{\widetilde{x}} c_{V0} + \delta \nabla_{\widetilde{x}} c_{V1} + \delta^2 \nabla_{\widetilde{x}} c_{V2} + \frac{1}{\delta}\nabla_{\widetilde{y}} c_{V0} + \nabla_{\widetilde{y}} c_{V1} + \delta \nabla_{\widetilde{y}} c_{V2} \tag{7.18}$$

And for the calculation of the Laplacian of c_V applying the differentiation rule eq. 7.11 to eq. 7.18,

$$\begin{aligned}\widetilde{\nabla}(\widetilde{\nabla}c_V) = {} & \delta^{-2}\nabla^2_{\widetilde{y}}c_{V0} \\ & + \delta^{-1}(\nabla_{\widetilde{x}}\nabla_{\widetilde{y}}c_{V0} + \nabla_{\widetilde{y}}\nabla_{\widetilde{x}}c_{V0} + \nabla^2_{\widetilde{y}}c_{V1}) \\ & + \delta^{0}(\nabla^2_{\widetilde{x}}c_{V0} + \nabla_{\widetilde{x}}\nabla_{\widetilde{y}}c_{V1} + \nabla_{\widetilde{y}}\nabla_{\widetilde{x}}c_{V1} + \nabla^2_{\widetilde{y}}c_{V2}) \\ & + \delta(\nabla^2_{\widetilde{x}}c_{V1} + \nabla_{\widetilde{x}}\nabla_{\widetilde{y}}c_{V2} + \nabla_{\widetilde{y}}\nabla_{\widetilde{x}}c_{V2}) \\ & + \delta^2\nabla^2_{\widetilde{x}}c_{V2}\end{aligned} \tag{7.19}$$

Equation 7.16 through means of eq. 7.9 eq. 7.19 gives:

$$\begin{aligned}T_V(\partial_t c_{V0} + \delta\partial_t c_{V1} + \delta^2\partial_t c_{V2}) = D_V(& \delta^{-2}\nabla^2_{\widetilde{y}}c_{V0} \\ & + \delta^{-1}(\nabla_{\widetilde{x}}\nabla_{\widetilde{y}}c_{V0} + \nabla_{\widetilde{y}}\nabla_{\widetilde{x}}c_{V0} + \nabla^2_{\widetilde{y}}c_{V1}) \\ & + \delta^{0}(\nabla^2_{\widetilde{x}}c_{V0} + \nabla_{\widetilde{x}}\nabla_{\widetilde{y}}c_{V1} + \nabla_{\widetilde{y}}\nabla_{\widetilde{x}}c_{V1} + \nabla^2_{\widetilde{y}}c_{V2}) \\ & + \delta(\nabla^2_{\widetilde{x}}c_{V1} + \nabla_{\widetilde{x}}\nabla_{\widetilde{y}}c_{V2} + \nabla_{\widetilde{y}}\nabla_{\widetilde{x}}c_{V2}) \\ & + \delta^2\nabla^2_{\widetilde{x}}c_{V2})\end{aligned} \tag{7.20}$$

As the homogenization is achieved for the limit of $\delta \to 0$ we have to set the terms multiplied by $1/\delta$ and $1/\delta^2$ equal to zero:

$$\nabla^2_{\widetilde{y}}c_{V0} = 0 \tag{7.21}$$

Differentiation of boundary condition eq. 7.6 according to eq. 7.9 and eq.7.11 provides:

$$\begin{aligned}& -\left(\frac{1}{\delta}\nabla_{\widetilde{y}}c_{V0} + (\nabla_{\widetilde{x}}c_{V0} + \nabla_{\widetilde{y}}c_{V1}) + \delta(\nabla_{\widetilde{x}}c_{V1} + \nabla_{\widetilde{y}}c_{V2}) + \delta^2\nabla_{\widetilde{x}}c_{V2}\right)\widehat{\nu} = \\ & \frac{kL_{MACRO}}{D_V}((c_{V0} - c_{Vref}) + \delta c_{V1} + \delta^2 c_{V2})\end{aligned} \tag{7.22}$$

Because of the δ^{-2} in 7.20(A-16) and the δ^{-1} in 7.22, and of the periodicity of $c_{V0}(\widetilde{\mathbf{x}}, \widetilde{\mathbf{y}})$ in y, we conclude that:

$$c_{V0}(\widetilde{\mathbf{x}}, \widetilde{\mathbf{y}}) = c_{V0}(\widetilde{\mathbf{x}}) \tag{7.23}$$

From the last equation, we see that any mixed derivative of $c_{V0}(\widetilde{\mathbf{x}})$involving differentiation with respect to y will be zero.

$$\nabla_{\widetilde{x}}\nabla_{\widetilde{y}}c_{V0} = \nabla_{\widetilde{y}}\nabla_{\widetilde{x}}c_{V0} = 0 \tag{7.24}$$

In this way, from eq. 7.17 we get:

$$\nabla^2_{\widetilde{x}}c_{V1} = 0 \tag{7.25}$$

We seek solutions of the form,

$$c_{V1}(\widetilde{\mathbf{x}},\widetilde{\mathbf{y}}) = w_j(\widetilde{\mathbf{y}})\partial x_j c_{V0}(\widetilde{\mathbf{x}}) + c_{V1}(\widetilde{\mathbf{x}}) \tag{7.26}$$

$$\nabla_{\widetilde{y}} c_{V1}(\widetilde{\mathbf{x}},\widetilde{\mathbf{y}}) = \nabla_{\widetilde{y}} w_j(\widetilde{\mathbf{y}})\partial\widetilde{\mathbf{x}} c_{V0}(\widetilde{x}) = \widehat{e}_j \partial\widetilde{y}_i w_j(\widetilde{y}_i)\partial\widetilde{\mathbf{x}} c_{V0}(\widetilde{x}) \tag{7.27}$$

$$\nabla_{\widetilde{y}}\nabla_{\widetilde{y}} c_{V1}(\widetilde{\mathbf{x}},\widetilde{\mathbf{y}}) = \partial\widetilde{y}_i\widetilde{y}_i w_j(\widetilde{y}_i)\partial\widetilde{x}_j c_{V0} \tag{7.28}$$

In eq. 7.27 and eq. 7.28 we have used the Einstein index notation where a repeated index conveys to summation over this index. i, $j = 1, 2, 3$.

From eq.7.28 wanting eq.7.29 to be true we get:

$$\nabla^2_{\widetilde{y}}(\widetilde{y}_i) = 0, \quad y \in S \tag{7.29}$$

The boundary condition for eq.7.29 is acquired by order δ^0 terms of eq.7.22

$$-(\nabla_{\widetilde{x}} c_{V0} + \nabla_{\widetilde{y}} c_{V1})\widehat{\nu} = \frac{T_V}{T_{RXN}}(c_{V0} - c_{V\,ref}), \quad \widetilde{x},\widetilde{y} \in \Gamma \tag{7.30}$$

Which taking into consideration eq. 7.15, finally gives for the boundary condition:

$$\partial\widetilde{y}_{\widehat{\nu}} w_i = -\widehat{e}_i\widehat{\nu}_i, \quad y \in \Gamma \tag{7.31}$$

Returning to eq.7.20 we now treat the δ^0 order terms, which by integration over the domain of the solid S, gives:

$$\begin{aligned} &T_V \int_S \partial_t c_{V0} d\widetilde{\mathbf{y}} = \\ &\int_S D_V(\nabla^2_{\widetilde{x}} c_{V0} + \nabla_{\widetilde{x}}\nabla_{\widetilde{y}} c_{V1} + \nabla_{\widetilde{y}}\nabla_{\widetilde{x}} c_{V1} + \nabla^2_{\widetilde{y}} c_{V2}) d\widetilde{\mathbf{y}} = \\ &\int_S D_V \nabla_{\widetilde{x}}(\nabla_{\widetilde{x}} c_{V0} + \nabla_{\widetilde{y}} c_{V1}) d\widetilde{\mathbf{y}} + \int_S D_V \nabla_{\widetilde{y}}(\nabla_{\widetilde{x}} c_{V1} + \nabla_{\widetilde{y}} c_{V2}) d\widetilde{\mathbf{y}} \end{aligned} \tag{7.32}$$

Applying Green's theorem on the second integral of the right hand side reveals:

$$T_V \int_S \partial_t c_{V0} d\widetilde{\mathbf{y}} = \int_S D_V \nabla_{\widetilde{x}}(\nabla_{\widetilde{x}} c_{V0} + \nabla_{\widetilde{y}} c_{V1}) d\widetilde{\mathbf{y}} + \int_\Gamma D_V \nabla_{\widetilde{y}}(\nabla_{\widetilde{x}} c_{V1} + \nabla_{\widetilde{y}} c_{V2})\widehat{\nu} dl \tag{7.33}$$

The boundary condition for eq.7.33 comes from the δ terms of eq.7.22.

$$-(\nabla_{\widetilde{x}} c_{V1} + \nabla_{\widetilde{y}} c_{V2})\widehat{\nu} = \frac{T_V}{T_{RXN}}(c_{V0} - c_{V\,ref}) \tag{7.34}$$

Meaning that because of time scale arguments the second integral of the right hand side of eq.7.33 can be dropped.

The first integral of the right hand side of eq.7.33 because of eq.7.27 is:

$$\begin{aligned}\int_S D_V \nabla_{\widetilde{x}}(\nabla_{\widetilde{x}} c_{V0} + \nabla_{\widetilde{y}} c_{V1}) d\widetilde{\mathbf{y}} &= \int_S D_V(\partial\widetilde{x}_j \partial\widetilde{x}_j c_{V0} + \partial\widetilde{x}_i \partial\widetilde{y}_i w_j(\widetilde{y}_i)\partial\widetilde{x}_j c_{V0}) d\widetilde{\mathbf{y}} \\ &= \int_S D_V(\partial\widetilde{x}_j^2 c_{V0} + \partial\widetilde{y}_i w_j(\widetilde{y}_i)\partial\widetilde{x}_j \partial\widetilde{x}_j c_{V0}) d\widetilde{\mathbf{y}} \\ &= \int_S D_V(\delta_{i,j}\partial\widetilde{x}_i \partial\widetilde{x}_j c_{V0} + \partial\widetilde{y}_i w_j(\widetilde{y}_i)\partial\widetilde{x}_j \partial\widetilde{x}_j c_{V0}) d\widetilde{\mathbf{y}} \\ &= \partial\widetilde{x}_i \partial\widetilde{x}_j c_{V0} \int_S (\delta_{ij} + \partial\widetilde{y}_i w_j(\widetilde{y}_i)) d\widetilde{\mathbf{y}}\end{aligned} \tag{7.35}$$

The following substitution, serves as a definition for tortuosity:

$$\frac{1}{\tau} = \int_S (\delta_{ij} + \partial\widetilde{y}_i w_j(\widetilde{y}_i)) d\widetilde{\mathbf{y}} \tag{7.36}$$

From eq.7.35 and eq.7.36 we get:

$$D_V \int_S \nabla_{\widetilde{x}}(\nabla_{\widetilde{x}} c_{V0} + \nabla_{\widetilde{y}} c_{V1}) d\widetilde{\mathbf{y}} = \frac{1}{\tau}\partial\widetilde{x}_i \partial\widetilde{x}_j c_{V0} \tag{7.37}$$

Collecting everything together, eq.7.33 reads:

$$\begin{aligned} T_V \partial_t \int_S c_{V0} d\widetilde{\mathbf{y}} &= \frac{|S|}{\tau} D_V \partial\widetilde{x}_i \partial\widetilde{x}_j c_{V0} + k \int_\Gamma (c_{V0} - c_{V ref}) dl \\ T_V |S| \partial_t c_{V0} &= \frac{|S|}{\tau} D_V \partial^2 \widetilde{x}_j c_{V0} + k|\Gamma|(c_{V0} - c_{V ref}) \end{aligned} \tag{7.38}$$

Where $|S|$ is the volume fraction of the solid, equal to $1-\varepsilon$. Returning to dimensional coordinate system, the upscaled equation for the diffusion of vacancies is:

$$(1-\varepsilon)\partial_t c_{V0} = \frac{1-\varepsilon}{\tau} D_V \partial_z^2 c_{V0} + k|\Gamma|(c_{V0} - c_{V ref}) \tag{7.39}$$

where c_{V0} is the vacancies concentration of order zero in the asymptotic expansion and $|\Gamma|$ is the surface available for reaction. Equation 7.39 is the exact same equation as Adlers equation (1) in his paper. By comparing equation eq. **??** coming from Homogenization with equation 7.1, taking into consideration equation eq.7.2, coming from [5], we observe that the two expressions are identical. The porosity for the unit cell in this context can be expressed as the volume fraction available for gas diffusion, i.e. as the ratio of the volume occupied by pores divided by the total area, taking $L_Y = 1$ It will simply be:

$$\varepsilon = 1 - \int_S d\mathbf{x} \tag{7.40}$$

$\mathcal{A}$ is given by the total area in the Y-cell of fig.7.2 where reactions occur:

$$\mathcal{A} = \int_{\Gamma} d\mathcal{A} \tag{7.41}$$

The z component of the invert tortuosity is:

$$\frac{1}{\tau} = \int_{S} \left(1 + \frac{\partial w}{\partial z}\right) dy \tag{7.42}$$

And hence,

$$\tau = \frac{1}{\int_{S} \left(1 + \frac{\partial w}{\partial z}\right) dy} \tag{7.43}$$

Summarizing, we can conclude that our approach of the cathode model under the same as Adler's assumptions is dictated by homogenization for a different than Adler's derivation for the reaction diffusion equation of the oxygen vacancies in the bulk, which however gives the same expression, i.e. equation 7.39. Moreover computation of the solid phase tortuosity, which is in general non-trivial, can be achieved from homogenization eq.7.29, by solving the relevant Boundary Value Problem for a Y-periodic auxiliary variable w(y) in the mixed conductor phase for a given structure.

7.2 Non-dimensionalization of Area Specific Resistance and Penetration Depth

Returning to equation eq. 7.3, we rewrite the specific area available for reaction in a way to get into the expression the micro-cube structure edge $_Y$. If S_Y is the surface available for reaction and V_Y is the volume of the solid phase in the Y-cell, then by the definition of specific area the following holds: $\alpha = \frac{S_Y}{V_Y} = \mathcal{A}\frac{1}{L_Y}$, where $\mathcal{A}$ is a rescaling of the area divided by the volume in the case $L_Y = 1$.

This gives that

$$R_{chem} = \frac{RT}{2F^2}\sqrt{\frac{\tau}{(1-\varepsilon)\mathcal{A}}}\sqrt{\frac{L_Y}{c_V D_V r_o(\alpha_f + \alpha_b)}} \tag{7.44}$$

Equation 7.44 is fundamental for our work and a better understanding of it is necessary. It encompasses the fact that there are major factors that affect the cell's resistance and correspondingly three major routes that one can follow to apply changes to it. The first term is the square root of the micro-scale length,L_Y. Given that the behavior of the material is limited by the chemistry, by minimizing the microstructure size L_Y one is able to continuously decrease R_{chem}. This is intuitively plausible, because if we decrease L_Y, we will increase the amount of area available for reactions per unit volume. L_Y is the length which we are free to choose limited only by manufacturing constraints. The next factor

is of electrochemical nature, i.e. $\sqrt{c_V D_V r_o(\alpha_f + \alpha_b)}$. As already mentioned before, fast reaction kinetics and high ionic conductivity lower the area specific resistance of the cell. The last factor involved is geometry, as quantified by the term $\sqrt{\frac{\tau}{(1-\varepsilon)\mathcal{A}}}$. This dependence directly suggests that the choice of micro-structure is crucial for the finally observed R_{chem}. A very tortuous path proves to be unfavorable, while the same is true when there is not a lot of surface for the exchange oxygen reaction to take place or when the ionic diffusion takes place through a narrow solid phase whose volume is $1 - \varepsilon$ in the context of our non dimensionalized Y-cell.

If the size of the Y-cell value and the electrochemical properties appearing in 7.44 are fixed, i.e. having a constant L_Y and for a given material, then we will be able to reduce R_{chem} if and only if the quantity $\frac{\tau}{(1-\varepsilon)\mathcal{A}}$ is reduced. This reduction will be weak as it will go with the square root of the latter quantity. The constant value of L_Y is dictated by the requirements and constraints of our manufacturing capabilities as described in references [66], [64], [74], [75], [76], [65], [67].

Therefore the task of minimizing the R_{chem} can be rewritten as:

$$min\left(\sqrt{\frac{\tau}{(1-\varepsilon)\mathcal{A}}}\right) \tag{7.45}$$

We note however that the limitation for applying the formula above can be reached if the R_{chem} becomes gas-diffusion limited. In this case, the expression above can no longer be used. By the same manipulation the expression for the penetration depth gives:

$$\delta_p = \sqrt{\frac{1-\varepsilon}{\mathcal{A}\tau}}\sqrt{\frac{c_V D_V}{r_o(\alpha_f + \alpha_b}}\sqrt{L_Y} \tag{7.46}$$

i.e. δp increases with the square root of L_Y and with the square root of the micro-structural parameter $\frac{1-\varepsilon}{\mathcal{A}\tau}$.

By dividing eq.7.44 and eq.7.46 by $\frac{RT}{2F^2}\sqrt{\frac{L_Y}{c_V D_V r_o(\alpha_f+\alpha_b)}}$ and $\sqrt{\frac{1-\varepsilon}{\mathcal{A}\tau}}\sqrt{\frac{c_V D_V}{r_o(\alpha_f+\alpha_b}}\sqrt{L_Y}$ respectively, we non-dimensionalize the quantities that drive the optimization and from hereafter we refer to them as $\widetilde{R}_{chem}$ and L_{RXN} i.e.

$$\widetilde{R}_{chem} = \sqrt{\frac{\tau}{(1-\varepsilon)\mathcal{A}}} \tag{7.47}$$

And

$$L_{RXN} = \sqrt{\frac{1-\varepsilon}{\mathcal{A}\tau}} \tag{7.48}$$

7.3 Numerical Calculations Strategy

The employed strategy to achieve the desired $\widetilde{R}_{chem}$ minimization consists of the following steps:

1. Selecting 4 fundamental micro-geometries which according to [66], [64], [74], [75], [76], [65], [67] are already feasible for manufacturing. These geometries are: cylinder, inverse cylinder, sphere and inverse sphere.

2. Solving the boundary value problem of the Laplace equation 7.29 with its boundary condition eq.7.31 for these geometries and then numerically acquire the z component of the gradient of the unknown field w leading to the tortuosity. Additionally, we calculate the porosity and the specific area of reaction either analytically or numerically.

3. Computing $\widetilde{R}_{chem}$ as a function of the radius of the geometry under study and then acquiring graphs relating all the desired quantities involved in equations 7.47 and 7.48.

   The numerical calculations and the solutions' visualizations are performed using the commercial package Comsol and the software's interface to Matlab. Indicative meshes for the geometries studied are shown in fig. 7.8,7.10, 7.11, 7.9. For each case and radius we used at least 5 mesh points in the shortest dimension of the problem while in the areas of big gradients care was taken to insure tightening of the discretization (sphere and inverse sphere). For a typical cylinder, e.g $r = 0.5$, mesh consists of 81485 tetrahedral, 5536 triangular, 192 edge and 8 vertex elements, while the minimum element quality was 0.3842, the average element quality 0.8281, the minimum element size was 0.018 and the maximum element size 0.1

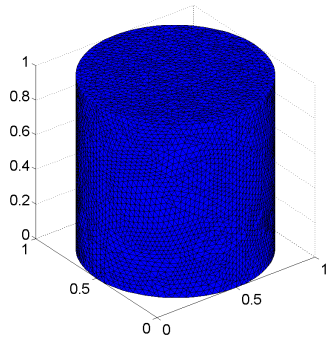

Figure 7.8: Mesh for a typical cylinder geometry, $r = 0.5$

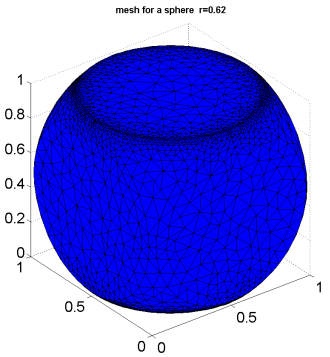

Figure 7.9: Mesh for a typical sphere geometry, $r = 0.62$

The same figures for a typical sphere calculation, e.g. $r = 0.62$, are 40267 tetrahedral, 6798 triangular, 544 edge and 24 vertex elements, the minimum element quality was 0.3443, the average element quality 0.7834 while the minimum element size was 0.0223 and the maximum element size is 0.124. As already

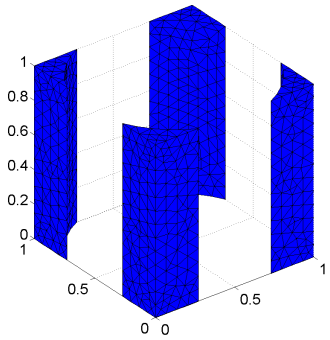

Figure 7.10: Mesh for a typical inverse cylinder geometry, $r = 0.55$

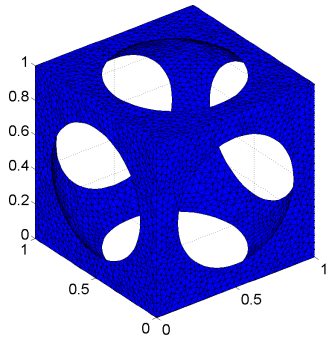

Figure 7.11: Mesh for a typical inverse sphere geometry, $r = 0.61$

mentioned, the boundary conditions are all symmetry conditions. The algorithm used was the direct solver UMFPACK.

7.4 Simulation Setup-Agreement between theoretical derivations and computational implementation

We now proceed with proving the validity of our method and with outlining the most significant aspects of the computational implementation in Comsol. The intersection of the solid phase with the unit cell edges significantly affects the derived formulas concerning the porosity, specific area and tortuosity. In addition, we have to deal with Comsols geometries and their edges definition requirements regarding the appropriate meshing of the computational domain $[0,1]^3$. These two facts dictate the discrimination of different radii regimes as follows. For all the cylinders, the sweeping of the radius ranges from zero to $\sqrt{2}/2$ while we need to distinguish between radius of less and greater than 0.5. For the spheres, the sweeping ranges from 0.5 to $\sqrt{3}/2$ and we have to distinguish between radius less and greater than $\sqrt{2}/2$. The boundary value problem discussed in the previous section leads to the calculation of the z component of the gradient of w. In the case of the cylinder and inverse cylinder, since the boundary condition means that there is no flux coming into or going out of the lateral cylinder surface, w is trivially shown to be constant everywhere and hence $\frac{\partial w}{\partial z} = 0$everywhere as also shown for example in fig. 7.12 where we see 5 slices of the z component of the gradient of w. The tortuosity from its definition equation 7.36 reduces to: $\tau_{cylinder} = \frac{1}{1-\varepsilon}$. For all other cases we rely to Comsol for the calculation of $\frac{\partial w}{\partial z}$.

Therefore, for the cylinder and inverse cylinder cases we have at our disposal theoretical formulas as well as the computational values for the porosity, the tortuosity, the specific area, and the non-dimensional reaction length and area specific resistance. For the sphere and inverse sphere cases and only for $0.5 \leq$

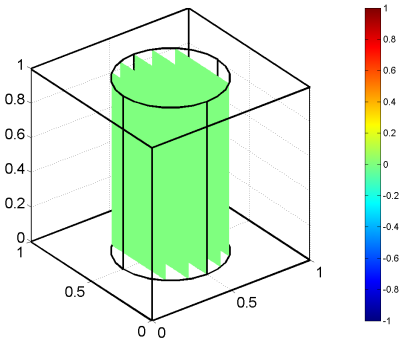

Figure 7.12: $\frac{\partial w}{\partial z} = 0$ for a cylinder geometry, $r = 0.30$

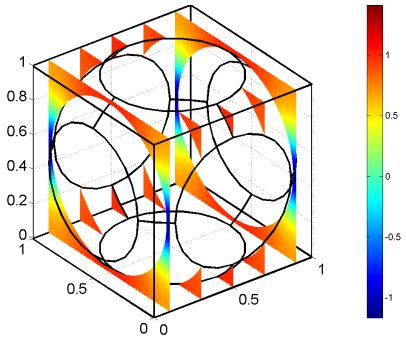

Figure 7.13: Representation of $\frac{\partial w}{\partial z}$ for an inverted spherical geometry, $r = 0.62$

$r \leq \frac{\sqrt{2}}{2}$ we have analytical expressions just for the geometric features in which we are interested in $(\varepsilon, \mathcal{A})$ and τ. In fig.7.13 we show slices of the computational solution for $\frac{\partial w}{\partial z}$ for a typical inverse sphere of $r = 0.62$ with arrows indicating the gradient of the field. We observe that the z component of the gradient of w is almost everywhere positive and hence so is the integral $\int_S \frac{\partial w}{\partial z} dy$ which is of specific interest to us since it affects significantly the calculation of the tortuosity as earlier demonstrated. On the other hand this integral in the spherical case is negative.

- Cylinder

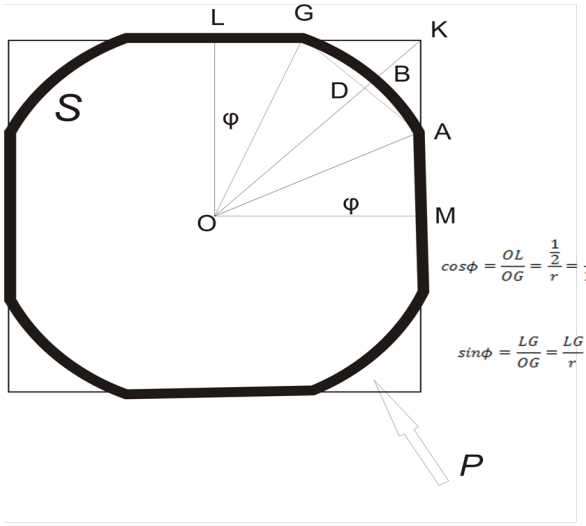

Figure 7.14: Horizontal cross section for a typical cylinder geometry with $0.5 \leq r \leq \frac{\sqrt{2}}{2}$

The upper limit value for the cylinder radius is equal to the half diagonal of the Y-cell cross section, i.e. $\sqrt{2}/2$. The absolute accordance between the theoretical and the computational result for $\widetilde{R}_{chem}$ is presented in Fig.7.15 and for L_{RXN} in fig.7.16 for a cylinder. This agreement also implies the agreement between computation and analytical calculation of the porosity and the specific area.

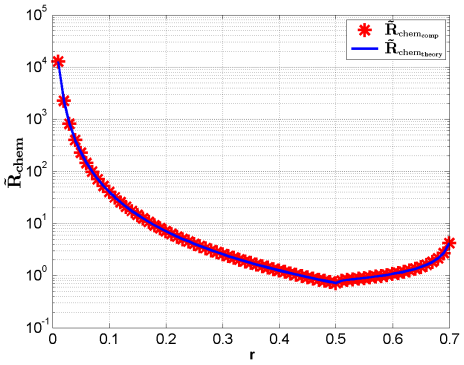

Figure 7.15: Agreement between analytical and computational calculation of $\widetilde{R}_{chem}$ for cylindrical geometries

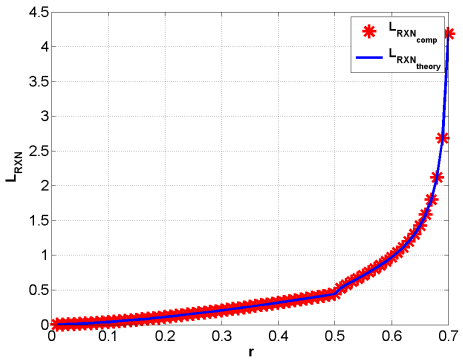

Figure 7.16: Agreement between analytical and computational calculation of L_{RXN} for cylindrical geometries

- Inverse cylinder The upper limit value for the inverse cylinder radius is again $\sqrt{2}/2$. The expected exact agreement between computational and theoretical results is demonstrated for $\widetilde{R}_{chem}$ in fig.7.17 and for L_{RXN} in fig. 7.18. The agreement between theory and computations in the cases of cylinder and inverse cylinder gives us confidence about using the computations in other micro structures cases, where the analytical solution cannot be obtained. This fact brings us to the examination of the sphere and inverse sphere micro structure

- Sphere $0.5 \leq r \leq \sqrt{2}/2$ By performing again some straight forward geometric calculations for the computation of the porosity and the specific area available for reaction for this case, we get good agreement between these theoretically calculated and computed geometric features. In this case however we do not employ any analytical calculation for the τ and correspondingly for the $\widetilde{R}_{chem}$ and the L_{RXN} and rely to Comsol entirely for their calculation. Another issue for the sphere is the realization of the boundary condition eq.7.31. By analysis of the problem we get the expression:

$$\frac{\partial w}{\partial \nu} = -\frac{z - z_0}{R} \tag{7.49}$$

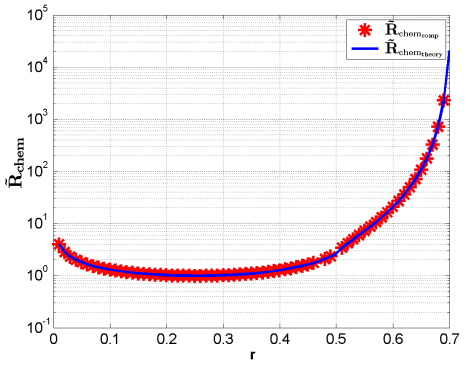

Figure 7.17: Agreement between analytical and computational calculation of $\widetilde{R}_{chem}$ for inverse cylindrical geometries

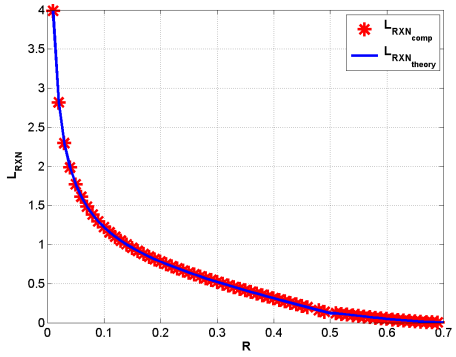

Figure 7.18: Agreement between analytical and computational calculation of L_{rxn} for inverse cylindrical geometries

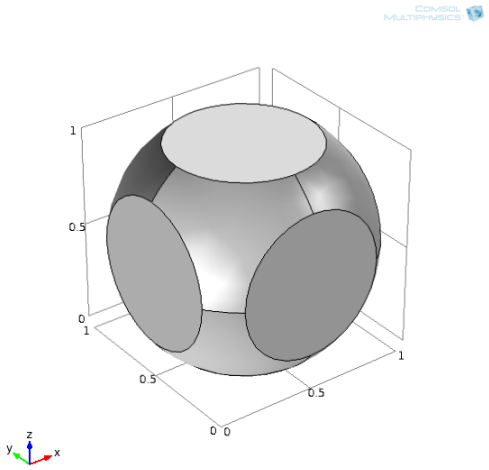

Figure 7.19: Composite object from Boolean difference of a sphere and the unit cube.

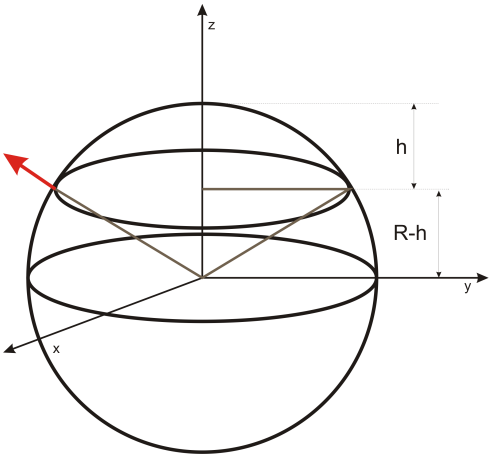

Figure 7.20: 3-dimensional representation of a sphere geometry for the calculation of the spherical caps volume and area

Equation 7.49 is the implementation of the boundary condition incorporated into Comsol scripts for Cartesian coordinates.

- Sphere $\frac{\sqrt{2}}{2} \leq r \leq \frac{\sqrt{3}}{2}$ For this case we acquire all the necessary geometric features computationally from Comsol. This is done through surface and volume integrations across the appropriate surfaces and volumes.

- Inverse Sphere The inverse sphere, being the complementary of the sphere in the unit cell when 0.5=r=v2/2 has analytically calculated porosity and specific area. The porosity is complementary to the spheres one while the specific area is exactly the same as in the sphere case. The case at which the radius ranges between $\frac{\sqrt{2}}{2} \leq r \leq \frac{\sqrt{3}}{2}$ is treated only numerically.

Chapter 8

Homogenization Results and discussion

Before focusing on the L_{RXN} and the $\widetilde{R}_{chem}$ we turn our attention to the geometric features of our problems. In Fig. 8a we show the effect of changing radius on the porosity for the different geometries. From a qualitative perspective it is apparent that the trends appearing following the corresponding change of volume of the solid phase of our structure are right and we have argued about the agreement between computational and analytical results at those cases where both are available.

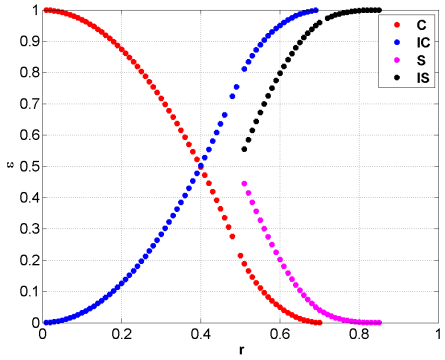

Figure 8.1: Dependence of porosity on radius for all cases

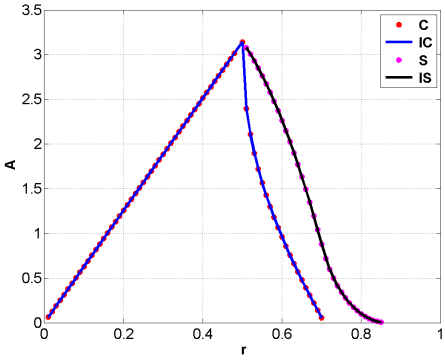

Figure 8.2: Dependence of specific area on radius for all cases

The same holds for the specific area and the tortuosity as presented in fig.8.2 and in fig.8.3 respectively. As shown earlier in equation eq.7.43, the tortuosity's calculation relies on computing the integral of the z component of gradient of w. This integral is negative for the sphere case and positive for the inverse

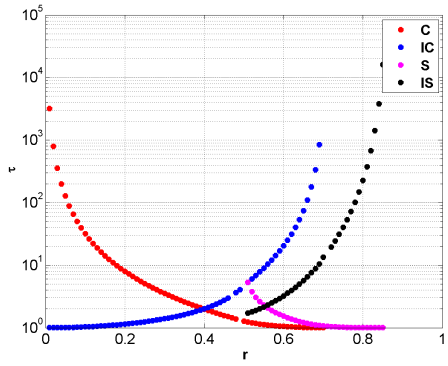

Figure 8.3: Dependence of tortuosity on radius for all cases

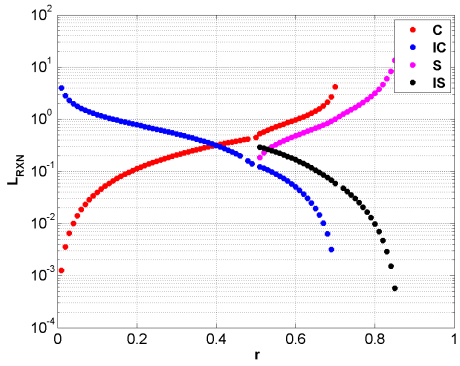

Figure 8.4: Dependence of L_{RXN} on radius for all cases

sphere with absolute value which decreases with increasing radius for both cases. Hence, in the sphere case increasing the radius decreases the tortuosity while in the inverse sphere case it increases it. These results are depicted in the above fig. 8.3. As commented before, in the cases of cylinder and inverse cylinder this integral is trivially shown to be zero.

Increasing the radius of a structure for a cylinder and a sphere, within the limits of their bounds, results in a significant increase, of orders of magnitudes, of the penetration depth. More specifically, as seen in fig.8.4, while the cylinder of radius $r = 0.1$ has a $L_{RXN} = 0.001248$, the cylinder of radius $r = 0.7$ has a $L_{RXN} = 4.182307$. For a sphere of $r = 0.51$ the non-dimensinal penetration depth is $L_{RXN} = 0.184510$, while the one with $r = 0.85$ has $L_{RXN} = 13.555356$. This is conceptually also aligned with our expectations because the increase of the volume of the solid phase results in a better connected material with better access for ions to penetrate in great depth and thus the reducing capacity of the bulk extends further out from the boundary with the electrolyte. The trend is completely inverted following the exact same reasoning, for the cases of inverse cylinder and sphere.

Turning our attention to fig.8.5 which depicts the dependence of the change of radius on the $\widetilde{R}_{chem}$ we observe various trends. In the beginning, for a cylinder and an inverse cylinder of $r = 0.5$ we see that for very small radii their resistance becomes unbounded. This is to be expected since it is exactly what the theoretical expressions for these cases predict, as shown by the following equations:

$$\widetilde{R}_{chem_{cyl.,r\leq 0.5}} = \frac{1}{\pi r^2\sqrt{2\pi r}} \tag{8.1}$$

And

$$\widetilde{R}_{chem_{inv.cyl.,r\leq 0.5}} = \frac{1}{(1-\pi r^2)\sqrt{2\pi r}} \tag{8.2}$$

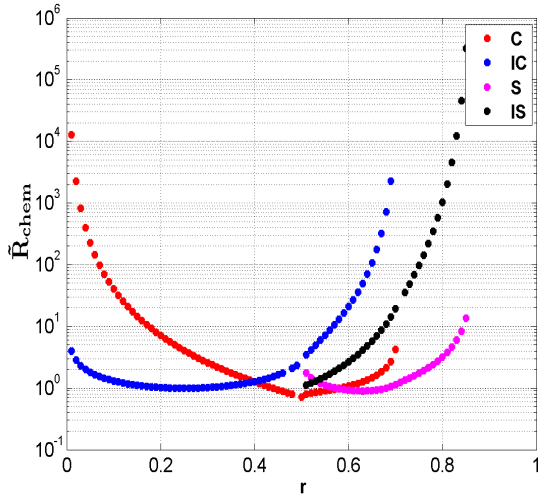

Figure 8.5: Dependence of $\widetilde{R}_{chem}$ on radius for all cases

These expressions belong to the theoretical derivations mentioned earlier and depicted for example in fig.7.15 and fig.7.17 of the previous section. From the same analytical expressions one finds that in both cases, the scaling of the radius coming from the active surface term contributes with a $-\frac{1}{2}$ power scaling while in the case of the cylinder, the cross sectional area, gives an additional scaling of -2, rising through the porosity term, making it $-2\frac{1}{2}$ in total. Furthermore, in the limit of r approaching infinity,$\widetilde{R}_{chem}$ of both sphere and inverse sphere also approaches infinity. Another immediate conclusion coming from fig.8.5 is that for 3 out of the 4 studied geometries a minimum can be achieved. These minima for each case are in Table 8.1 below:

Table 8.1: $\widetilde{R}_{chem}$ minima for the different micro-structure geometries

	r	**Minimum Value**
Cylinder	0.5	0.7180
Inverse Cylinder	0.25	0.9928
Inverse Sphere	0.63	0.8969

Cylinder of radius $r = 0.5$ is the one that will present the smaller loses out of all the geometries included in our study, followed by the sphere of $r = 0.63$ and the inverse cylinder of $r = 0.25$. In order to comprehend the location of the local minimum in each of the above cases, we revert to the fact that all this analysis has come down to a very simple one dimensional optimization problem with independent variable just the radius of the micro structure. Hence by first order differentiation we get the necessary condition for local optimum and the

corresponding location. The first order derivative for the cylinder for $r = 0.5$ from equation 8.3(15) is calculated to be: $-\frac{5}{2\sqrt{2}\pi^{3/2}r^{7/2}}$. However the derivative from the right with respect to $r = 0.5$ is very complicated to be calculated analytically, not to mention that there is definitely a jump between the left and right derivatives at $r = 0.5$ as we can see from fig.8.5. We can however verify the existence of a minimum for $r = 0.5$ for the cylinder as follows. We see from the porosity fig. 8.1 that the porosity is continuously diminishing, so it applies a decrease in $\widetilde{R}_{chem}$ and from the tortuosity Fig.8.3 that it affects the $\widetilde{R}_{chem}$ exactly as the porosity. Hence, any variation in the tangent of the $\widetilde{R}_{chem}$ equation is provoked by the specific area, which indeed at 0.5 has a maximum and hence its square inverse present in $\widetilde{R}_{chem}$, a minimum. As far as the inverse cylinder is concerned, the derivative in the range $0 \leq r \leq 0.5$ we can differentiate and acquire the candidate minimum point. The derivative is:

$$\widetilde{R}'_{chem} = \frac{\sqrt{2\pi}\sqrt{r}}{(1-\pi r^2)^2} - \frac{1}{2\sqrt{2\pi}r^{3/2}(1-\pi r^2)} \tag{8.3}$$

with an analytically calculated root root at $r = \sqrt{\frac{1}{5\pi}} = 0.2523$ as we can see in fig.8.6.

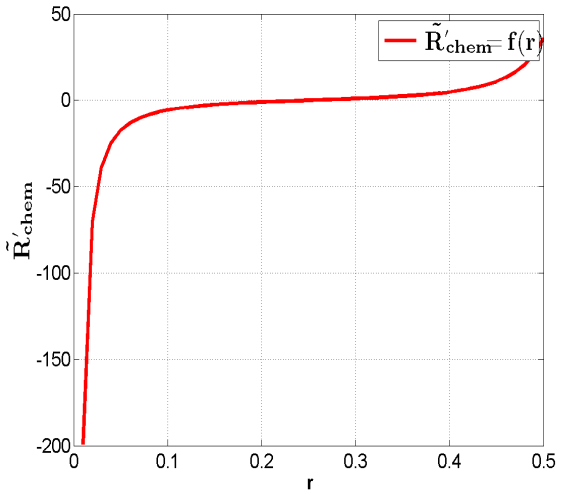

Figure 8.6: Derivative of $\widetilde{R}_{chem}$ for an inverse cylinder with $r \leq 0.5$

Regarding the minimum observed for the sphere, since we do not have in our possession analytical expressions for the $\widetilde{R}_{chem}$ we focus on studying the independent pieces that affect it according to its definition in the range of interest which is $0.5 \leq r \leq \frac{\sqrt{2}}{2}$. In this range, the porosity and the tortuosity have again both a decreasing effect on $\widetilde{R}_{chem}$ but the inverse square of the specific area an increasing one. The balance of these competing tendencies produces the

observed minimum. At that point the porosity is $\varepsilon = 0.139491$, the tortuosity is $\tau = 1.315110$ and the specific area $\mathcal{A} = 1.900042$ giving the observed minimum value for $\widetilde{R}_{chem}$. Finally, using as starting point the observation that the case of the inverse sphere is the only one of those studied exhibiting no minimum for the non-dimensional $\widetilde{R}_{chem}$, we state that further investigation is needed repeating the same calculations for more fundamental geometries, to check if a correlation can be established between the existence of a minimum and the sign of the integral of the z component of the w field.

Chapter 9

Conclusions and Outlook

9.1 Conclusion

In the context of the PhD at hand, the core activities were aimed at the application of multi-scale modeling on SOFCs. In the first place we derived accurate $2D$ models for the electrical potential distribution and the fluid flow for the operation of an anode SOFC interconnect. This theoretical work paid off by providing us with a closed form analytical expression for the cell's net power. Furthermore, the theoretical investigations served as the background for applying the same model in an FEM commercial package for the solution of the PDEs and successively combine it with the popular method of topology optimization to derive geometrical patterns that would enhance our chosen objective, i.e. maximize the cell's net power. The emerging configurations are irregularly spaced and shaped interconnect material. Out of the parameters studied the more pronounced effect of the geometry was offered by the electrical conductivity of interconnect, which in any case justifies the importance that the design of this component of the whole cell, should receive. The stable working model was extended to include the (varying) mass transport in the channel and the diffusion between the gases concentrations, with limited so far reward but with good possibility for greater one in the imminent future. Finally, we have produced by homogenization the up-scaled convection diffusion reaction equation for the oxygen vacancies for a typical cathode material in a SOFC. Our work is aligned with earlier theoretical results which provide an expression for the calculation of the Area Specific Resistance. We then selected four different fundamental micro-structures and calculated for these cases the non-dimensional Area Specific Resistance of the electrode as a function of the structures geometry, for fixed micro-length scale and electrochemical properties. We have been able to minimize the Area Specific Resistance of this electrode in the cases at which the microstructure was a cylin-

der, an inverse cylinder and a sphere. Out of these 3 structures better kinetics are exhibited in the case of cylinder of radius 0.5 situated symmetrically in the center of a non-dimensionalized unit cell. We have further laid the foundation for extending this work in investigating other fundamental structures and also to treat the case of a Mixed Ionic and Electronic Conductor with finite electronic conductivity.

9.2 Outlook

Many directions of possible extensions of our work can be developed and taken. With actual implementation and assisting real mass scale production of SOFCs into mind, a first step could be to exhaust the limits of the theoretical investigations by applying a full scan on the parameterized expressions for all three cases of comparison between the radius of the cylinder and the gas channel's height divided by the square root of twelve. This can serve as a guide in the early design phase of any SOFC interconnect. The derivations made on the anode side, from a theoretical and simulations' point of view, implicitly suggests that a similar model for the cathode is also feasible in 2D as well. Hence, the whole cell's operation can be described following the same as ours reasoning.
One path of particular interest that would make a full 2D model could come in two steps. Relatively easy as first step, is the addition of the PDE that describes the temperature distribution in the cell. This is one extra equation with just only one extra unknown. Acquiring access on the temperature, opens the door to addition of a full structural analysis of the cell, where the support that should be offered by the pillars to the planar rectangular plate of the interconnect above the channel can be calculated. Our method's of dealing the suppression of the third dimensions of the fluid flow by introducing the damping term coming form lubrication theory can handle variable channel heights as well, with just a simple modification of the continuity equation, as similar work in the context of our group's and personal activities have shown, in model cases of combining fluid flow with membranes' mechanical support, structurally optimized.

One step further, having the solid tool founded here, it would be very interesting to perform the numerical calculation for a multiplicity of other objective functions. The efficiency of the cell and the interconnect should be the first cases examined in this respect. The quantitative analysis missing in some aspects of the work on the simulations part of all subproblems, like for example the area of material in total as a percentage of the cell's area and the average area of each structure introduced by the topology optimization, as a variable of the numerical runs parameters is natural and straight forward. Another future challenge would be the broadening of those parameters, to include the height of the gas channel,

synonymous to the height of the current collector's pillars, which has proven to be so catalytic in our theoretical approach. Industry for example would certainly be interested to find out what are the limits of this extreme aspect ratio of the channel (the ratio between the height and the length of the channel) and how low it should get and with what expected gain. However, this would require extra care in resolving numerical hardships that would also arise as a consequence of introducing smaller and smaller length scales.

Our work on homogenization has laid the ground for what is a straight forward extension, i.e. the treatment of MIEC material for the cathode with finite electrical conductivity in the steady state. By preliminary work on this topic, we have already seen that the result will include the solution of a system of two coupled up-scaled PDE's for the electronic and the ionic electrochemical potentials.

At the next level of what is a harder problem to deal with, we wish to attack the problem of modeling the impedance response of grain and grain boundaries. Here we will use asymptotic analysis similar to the one exhibited in the relevant chapter, to study samples composed by many grains assuming that we have still two distinct macro and micro length scales.

Bibliography

[1] R. Bove and S.Ubertini. *Modeling Solid Oxide Fuel Cells*. Springer, 2 edition, 2009. [cited at p. ix, 3, 28, 40]

[2] A. Salogni and P. Colonna b. Modeling of solid oxide fuel cells for dynamic simulations of integrated systems. *Applied Thermal Engineering*, 30:464–477, 2010. [cited at p. ix, 4]

[3] J. Larminie and A. Dicks. *Fuel Cell Systems Explained*. 2003. [cited at p. ix, 4, 10, 37]

[4] American Ceramic Society Bulletin, Vol. 89, No. 3. [cited at p. ix, 8]

[5] S. B. Adler, J. A. Lane, and B. C. H. Steele. Electrode kinetics of porous mixed-conducting oxygen electrodes. *Journal of the Electrochemical Society*, 143(11):3554–3564, 1996. [cited at p. xi, 76, 77, 79, 80, 88]

[6] Andrew L. Dicks. Hydrogen generation from natural gas for the fuel cell systems of tomorrow. *Journal of Power Sources*, 61:113–124, 1996. [cited at p. 2]

[7] A. Samson Nesaraj. Recent developments in solid oxide fuel cell technology - a review. *Journal of Scientific and Industrial Research*, 69:169–176, 2010. [cited at p. 2]

[8] K. Pointon T.A. Smith S.H. Clarke, A.L. Dicks and A. Swann. Catalytic aspects of the steam reforming of hydrocarbons in internal reforming fuel cells. *Catalysis Today*, 38:411–423, 1997. [cited at p. 2]

[9] R. Peters, R. Dahl, U. Kluttgen, C. Palm, and D. Stolten. Internal reforming of methane in solid oxide fuel cell systems. *Journal of Power Sources*, 106:238–244, 2002. [cited at p. 2]

[10] B. Sorensen. *Hydrogen and Fuel Cells*. Elsevier Academic Press, 1 edition, 2005. [cited at p. 2]

[11] S.C. Singhal and K. Kendall. *High Temperature Solid Oxide Fuel Cells.* Elsevier Academic Press, 1 edition, 2003. [cited at p. 2]

[12] Charles E. Compson. *Design, fabrication and characterization of novel planar solid oxide fuel cells.* PhD thesis, Georgia Institute of Technology, 2007. [cited at p. 3, 11]

[13] Jeffrey W. Fergus, Jiujun Zhang, Xianguo Li, David P. Wilkinson, and Rob Hui. *Solid Oxide Fuel Cells, Materials Properties and Performance.* CRC Press, 2009. [cited at p. 3]

[14] Demetrios A. Presvytes. *Solid Oxide Fuel Cells: Triode Operation, Mathematical Modeling and Temperature Programmed Desorption Study.* PhD thesis, University of Patras, 2009. [cited at p. 3, 11]

[15] Jonh D. Anderson Jr. *Fundamentals of Aerodynamics.* McGraw Hill, Inc., 5 edition, 2005. [cited at p. 14]

[16] Henrik Bruus. *Theoretical Microfluidics.* Oxford Master Series in Physics. Oxford University Press, 2008. [cited at p. 14, 16]

[17] G.K. Batchelor. *An Introduction to Fluid Dynamics.* Cambridge University Press, 1967. [cited at p. 16, 17]

[18] Frank M. White. *Visous Fuid Flow.* McGraw Hill, Inc., 2 edition, 1991. [cited at p. 16, 17]

[19] B. Todd and J. B. Young. Thermodynamic and transport properties of gases for use in solid oxide fuel cell modelling. *Journal of Power Sources*, 110(1):186–200, 2002. Times Cited: 145. [cited at p. 17]

[20] T. Borrvall and J. Petersson. Topology optimization of fluids in stokes flow. *International Journal for Numerical Methods in Fluids*, 41(1):77–107, 2003. Times Cited: 101 Borrvall, T Petersson, J. [cited at p. 17, 48, 57]

[21] L.M. Milne-Thomson. *Theoretical Hydrodynamics.* 4 edition, 1962. [cited at p. 17]

[22] S. M. Abane. Calculation of oseen flows past a circular-cylinder at low reynolds-numbers. *Applied Scientific Research*, 34(4):413–426, 1978. Times Cited: 0. [cited at p. 17]

[23] S. Goldstein. The steady flow of viscous fluid past a fixed spherical obstacle at small reynolds numbers. *Proceedings of the Royal Society of London Series a-Containing Papers of a Mathematical and Physical Character*, 123(791):225–235, 1929. Times Cited: 81. [cited at p. 17, 19]

[24] S. Tomotika and T. Aoi. The steady flow of viscous fluid past a sphere and circular cylinder at small reynolds numbers. *Quarterly Journal of Mechanics and Applied Mathematics*, 3(2):140–161, 1950. [cited at p. 17, 19, 22]

[25] Jrgen Fredse Mutlu Sumer. *Hydrodynamics around Cylindrical Structures.* World sceintific Publishing, 2006. [cited at p. 18]

[26] Ira Cohen Pijush Kundu. *Fluid Mechanics.* Academic Press, 2002. [cited at p. 18]

[27] Stephen Childress. *An introdustion to Theoretical Fluid Mechanics.* 2009. [cited at p. 18]

[28] I. Proudman and J. R. A. Pearson. Expansions at small reynolds numbers for the flow past a sphere and a circular cylinder. *Journal of Fluid Mechanics*, 2(3):237–262, 1957. Times Cited: 506. [cited at p. 19, 22]

[29] F. Mandujano and R. Peralta-Fabi. On the viscous steady flow around a circular cylinder. *Revista Mexicana De Fisica*, 51(1):87–99, 2005. Times Cited: 2. [cited at p. 19]

[30] Erwin Kreyszig. *Advanced Engineering Mathematics.* 8 edition. [cited at p. 36]

[31] Mathias Brinch-Larsen. Investigations and modelling of solid oxide fuel cell cathodes. Master's thesis, DTU-RIS, 2012. [cited at p. 37, 38]

[32] C. Chatzichristodoulou, M. Sogaard, and P. V. Hendriksen. Oxygen permeation in thin, dense ce0.9gd0.1o1.95-delta membranes i. model study. *Journal of the Electrochemical Society*, 158(5):F61–F72, 2011. Times Cited: 7. [cited at p. 41]

[33] M. P. Bendsoe and N. Kikuchi. Generating optimal topologies in structural design using a homogenization method. *Computer Methods in Applied Mechanics and Engineering*, 71(2):197–224, 1988. Times Cited: 1416 Bendsoe, mp kikuchi, n. [cited at p. 47]

[34] Ole Sigmund Martin .P. Bendsoe. *Topology Optimization, Theory Methods and Applications.* Springer, 2003. [cited at p. 47, 60]

[35] Anders Klarbring Peter .W. Christensen. *An introduction to Structural Optimization.* Springer, 2009. [cited at p. 47]

[36] Eschenauer H. and Olhoff N. Topology optimization of continuum structures: A review. *Applied Mechanics Rev*, 54(4), 2001. [cited at p. 47]

[37] L. H. Olesen, F. Okkels, and H. Bruus. A high-level programming-language implementation of topology optimization applied to steady-state navier-stokes flow. *International Journal for Numerical Methods in Engineering*, 65(7):975–1001, 2006. Times Cited: 59 Olesen, LH Okkels, F Bruus, H. [cited at p. 48, 51, 55, 57, 58]

[38] [cited at p. 48]

[39] A. Evgrafov. Topology optimization of slightly compressible fluids. *Zamm-Zeitschrift Fur Angewandte Mathematik Und Mechanik*, 86(1):46–62, 2006. Times Cited: 8. [cited at p. 48]

[40] A. Evgrafov. The limits of porous materials in the topology optimization of stokes flows. *Applied Mathematics and Optimization*, 52(3):263–277, 2005. Times Cited: 14 Evgrafov, A. [cited at p. 48]

[41] J. K. Guest and J. H. Prevost. Topology optimization of creeping fluid flows using a darcy-stokes finite element. *International Journal for Numerical Methods in Engineering*, 66(3):461–484, 2006. Times Cited: 42 Guest, JK Prevost, JH. [cited at p. 48]

[42] C. S. Andreasen, A. R. Gersborg, and O. Sigmund. Topology optimization of microfluidic mixers. *International Journal for Numerical Methods in Fluids*, 61(5):498–513, 2009. Times Cited: 13 Andreasen, Casper Schousboe Gersborg, Allan Roulund Sigmund, Ole. [cited at p. 48, 57]

[43] N. Aage, T. H. Poulsen, A. Gersborg-Hansen, and O. Sigmund. Topology optimization of large scale stokes flow problems. *Structural and Multidisciplinary Optimization*, 35(2):175–180, 2008. Times Cited: 14 Aage, Niels Poulsen, Thomas H. Gersborg-Hansen, Allan Sigmund, Ole. [cited at p. 48, 60]

[44] Xiankai Song, Diaz A.R., and Benard A. A 3d topology optimization model of the cathode air supply channel in planar solid oxide fuel cell. 2013. [cited at p. 48]

[45] C. Kim and H. Sun. Topology optimization of gas flow channel routes in an automotive fuel cell. *International Journal of Automotive Technology*, 13(5):783–789, 2012. Times Cited: 0 Kim, C. Sun, H. [cited at p. 48]

[46] S.J. Arora. *Introduction to Optimum Design*. McGraw-Hill, 1989. [cited at p. 49]

[47] L. D. Landau and E. M. Lifshitz. *Fluid Mechanics, Course of Theoretical Physics, Vol. 6*. Pergamon, Oxford, 2 edition, 1987. [cited at p. 51]

[48] M. A. Khaleel, Z. Lin, P. Singh, W. Surdoval, and D. Collin. A finite element analysis modeling tool for solid oxide fuel cell development: coupled electrochemistry, thermal and flow analysis in marc((r)). *Journal of Power Sources*, 130(1-2):136–148, 2004. Times Cited: 96 Khaleel, MA Lin, Z Singh, P Surdoval, W Collin, D. [cited at p. 52]

[49] Krister Svanberg. The method of moving asymptotes-a new method for structural optimization. *International Journal for Numerical Methods in Engineering*, 24:359–373, 1987. [cited at p. 57]

[50] N. Wiker, A. Klarbring, and T. Borrvall. The darcy-stokes topology optimization problem. 137:551–558, 2006. Times Cited: 0 Wiker, Niclas Klarbring, Anders Borrvall, Thomas IUTAM Symposium on Topological Design Optimization of Structures, Machines and Materials Oct, 2005 Copenhagen, DENMARK. [cited at p. 57]

[51] P. Michaleris, D. A. Tortorelli, and C. A. Vidal. Tangent operators and design sensitivity formulations for transient nonlinear coupled problems with applications to elastoplasticity. *International Journal for Numerical Methods in Engineering*, 37(14):2471–2499, 1994. Times Cited: 117. [cited at p. 58]

[52] S. B. Adler. Factors governing oxygen reduction in solid oxide fuel cell cathodes. *Chemical Reviews*, 104(10):4791–4843, 2004. [cited at p. 76]

[53] J. Fleig. Solid oxide fuel cell cathodes: Polarization mechanisms and modeling of the electrochemical performance. *Annual Review of Materials Research*, 33:361–382, 2003. [cited at p. 76]

[54] S. M. Haile. Fuel cell materials and components. *Acta Materialia*, 51(19):5981–6000, 2003. [cited at p. 76]

[55] J. Li S.P. Jiang. *Solid Oxide Fuel Cells, Materials Properties and Performance*. Green Chemistry and Chemical Engineering. CRC Press Taylor & Francis Group, LLC, 2009. [cited at p. 76]

[56] J. Deseure, Y. Bultel, L. Dessemond, E. Siebert, and P. Ozil. Modelling the porous cathode of a sofc: oxygen reduction mechanism effect. *Journal of Applied Electrochemistry*, 37(1):129–136, 2007. [cited at p. 76]

[57] Torben Jacobsen Martin Sgaard, Peter Vang Hendriksen and Mogens Mogensen. Modelling of the polarization resistance from surface exchange and diffusion coefficient data, 2006. [cited at p. 76]

[58] Y. H. Li, R. Gemmen, and X. B. Liu. Oxygen reduction and transportation mechanisms in solid oxide fuel cell cathodes. *Journal of Power Sources*, 195(11):3345–3358, 2010. [cited at p. 76]

[59] J. D. Fehribach and R. O'Hayre. Triple phase boundaries in solid-oxide cathodes. *Siam Journal on Applied Mathematics*, 70(2):510–530, 2009. [cited at p. 76]

[60] Y. W. Zeng, C. G. Tian, and L. M. Bao. A modeling investigation on the electrochemical behavior of porous mixed conducting cathodes for solid oxide fuel cells. *Journal of Power Sources*, 139(1-2):35–43, 2005. [cited at p. 76]

[61] S. Y. Wang, J. Yoon, G. Kim, D. X. Huang, H. Y. Wang, and A. J. Jacobson. Electrochemical properties of nanocrystalline la0.5sr0.5coo3-x thin films. *Chemistry of Materials*, 22(3):776–782, 2010. [cited at p. 76]

[62] [cited at p. 76]

[63] B. Ruger, A. Weber, and E. Ivers-Tiffee. *3D-Modelling and Performance Evaluation of Mixed Conducting (MIEC) Cathodes*, volume 7 of *ECS Transactions*, pages 2065–2074. 2007. [cited at p. 76]

[64] Y. An, S. J. Skinner, and D. W. McComb. Template-assisted fabrication of macroporous thin films for solid oxide fuel cells. *Journal of Materials Chemistry*, 20(2):248–254, 2010. [cited at p. 77, 90, 91]

[65] J. C. Ruiz-Morales, D. Marrero-Lopez, M. Galvez-Sanchez, J. Canales-Vazquez, C. Savaniu, and S. N. Savvin. Engineering of materials for solid oxide fuel cells and other energy and environmental applications. *Energy & Environmental Science*, 3(11):1670–1681, 2010. [cited at p. 77, 90, 91]

[66] G. A. Umeda, W. C. Chueh, L. Noailles, S. M. Haile, and B. S. Dunn. Inverse opal ceria-zirconia: architectural engineering for heterogeneous catalysis. *Energy & Environmental Science*, 1(4):484–486, 2008. [cited at p. 77, 90, 91]

[67] E. C. Brown, S. K. Wilke, D. A. Boyd, D. G. Goodwin, and S. M. Haile. Polymer sphere lithography for solid oxide fuel cells: a route to functional, well-defined electrode structures. *Journal of Materials Chemistry*, 20(11):2190–2196, 2010. [cited at p. 77, 90, 91]

[68] J. H. Kim, W. K. Liu, and C. Lee. Multi-scale solid oxide fuel cell materials modeling. *Computational Mechanics*, 44(5):683–703, 2009. [cited at p. 77]

[69] F. Ciucci and W. Lai. Derivation of micro/macro lithium battery models from homogenization. *Transport in Porous Media*, 88(2):249–270, 2011. [cited at p. 77, 83]

[70] M. Schmuck. Modeling and deriving porous media stokes-poisson-nernst-planck equations by a multi-scale approach. *Communications in Mathematical Sciences*, 9(3):685–710, 2011. [cited at p. 77]

[71] M. Mihailovici and B. Schweizer. Effective model for the cathode catalyst layer in fuel cells. *Asymptotic Analysis*, 57(1-2):105–123, 2008. [cited at p. 77]

[72] S. B. Adler. Mechanism and kinetics of oxygen reduction on porous la1-xsrxcoo3-delta electrodes. *Solid State Ionics*, 111(1-2):125–134, 1998. [cited at p. 77]

[73] Ulrich Hornung. *Homogenization and Porous Media*. Interdisciplinary Applied Mathematics. Springer-Verlag NY Inc, 1996. [cited at p. 83]

[74] W. P. Pan, Z. Lu, K. F. Chen, X. B. Zhu, X. Q. Huang, Y. H. Zhang, B. Wei, and W. H. Su. Paper-fibres used as a pore-former for anode substrate of solid oxide fuel cell. *Fuel Cells*, 11(2):172–177, 2011. [cited at p. 90, 91]

[75] J. C. Ruiz-Morales, J. Canales-Vazquez, J. Pena-Martinez, D. Marrero-Lopez, J. T. S. Irvine, and P. Nunez. Microstructural optimisation of materials for sofc applications using pmma microspheres. *Journal of Materials Chemistry*, 16(6):540–542, 2006. [cited at p. 90, 91]

[76] J. C. Ruiz-Morales, D. Marrero-Lopez, J. Canales-Vazquez, P. Nunez, and J. M. Dominguez-Gonzalez. A novel approach to engineer the microstructure of solid oxide fuel cell materials. *Fuel Cells*, 11(1):144–149, 2011. [cited at p. 90, 91]

Appendix A

Papers

INTERNATIONAL JOURNAL OF HYDROGEN ENERGY XXX (2013) 1–6

Available online at www.sciencedirect.com

SciVerse ScienceDirect

journal homepage: www.elsevier.com/locate/he

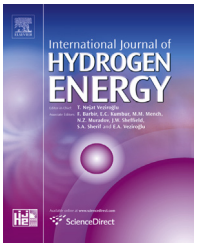

Polymer-stable magnesium nanocomposites prepared by laser ablation for efficient hydrogen storage

S.S. Makridis [a,b,*], E.I. Gkanas [a,b], G. Panagakos [a], E.S. Kikkinides [b], A.K. Stubos [a], P. Wagener [c], S. Barcikowski [c]

[a] Environmental Technology Laboratory, Institute of Nuclear Technology and Radiation Protection, NCSR 'Demokritos', Agia Paraskevi, Athens 15310, Greece

[b] Department of Mechanical Engineering, University of Western Macedonia, Bakola & Sialvera Street, Kozani 50100, Greece

[c] Technical Chemistry I and Center for Nanointegration Duisburg-Essen (CENIDE), University of Duisburg, Universitaetsstrasse 7, D-45141 Essen, Germany

ARTICLE INFO

Article history:
Received 2 November 2012
Received in revised form
3 April 2013
Accepted 5 April 2013
Available online xxx

Keywords:
Hydrogen storage
Mg-nanoparticles
Polymer matrix composites
Laser ablation

ABSTRACT

Hydrogen is a promising alternative energy carrier that can potentially facilitate the transition from fossil fuels to sources of clean energy because of its prominent advantages such as high energy density (142 MJ kg^{-1}), great variety of potential sources (for example water, biomass, organic matter), and low environmental impact (water is the sole combustion product). However, due to its light weight, the efficient storage of hydrogen is still an issue investigated intensely. Various solid media have been considered in that respect among which magnesium hydride stands out as a candidate offering distinct advantages.

Recent theoretical work indicates that MgH_2 becomes less thermodynamically stable as particle diameter decreases below 2 nm. Our DFT (density functional theory) modeling studies have shown that the smallest enthalpy change, corresponding to 2 unit-cell thickness (1.6 Å Mg/3.0Å MgH_2) of the film, is 57.7 kJ/molMg. This enthalpy change is over 10 kJ/molMg smaller than that of the bulk. It is important to note that the range of enthalpy change for systems that are suitable for mobile storage applications is 15–24 kJ/molH at 298 K.

The important key for the development of air-stable Mg-nanocrystals is the use of PMMA (polymethylmethacrylate) as an encapsulation agent. In our work we use laser ablation, a non-electrochemical method, for producing well-dispersed nanoparticles without the presence of any long-range aggregation. The observed improved hydrogenation characteristics of the polymer-stable Mg-nanoparticles are associated to the preparation procedure and in any case the polymer-laser ablation is a new approach for the production of air-protected and inexpensive Mg-nanoparticles.

* *Corresponding author*. Department of Mechanical Engineering, University of Western Macedonia, Bakola & Sialvera Street, Kozani 50100, Greece. Tel.: +30 2461056752; fax: +30 2461056601.

E-mail addresses: sofmak@ipta.demokritos.gr, ssmakridis@gmail.com (S.S. Makridis).

0360-3199/$ – see front matter Copyright © 2013, Hydrogen Energy Publications, LLC. Published by Elsevier Ltd. All rights reserved.
http://dx.doi.org/10.1016/j.ijhydene.2013.04.031

1. Introduction

The continuous growth of world population and the intense economic expansion of developing countries are among the major causes of the increasing demand for energy and the alarming and continuous release of greenhouse gases. Among several scenarios, hydrogen is the most promising energy carrier to satisfy the required conditions for the ideal fuel. It is the cleanest fuel and has a heating value three times higher than petroleum. While it seems to be the ideal means of transport and conversion of energy for mobile and stationary applications, a major problem is the storage of hydrogen which presents several issues mainly related to safety and amount of stored hydrogen [1].

In recent years a lot of research has been done on materials for hydrogen storage. Magnesium-based alloys have attracted much attention due to high hydrogen capacity and low cost. It is reported that pure Mg can store up to 7.6 wt% [1–3]. For pure Mg, the hydrogenation enthalpy is around −74.7 kJ/mol H_2 and its activation energy is evaluated to be 86 kJ/mol H_2 [4,5].

Despite the relatively high capacity, there are certain important disadvantages of using Mg alloys such as slow kinetics, high operation temperatures and high reactivity with oxygen [6–10] which constitute significant obstacles for practical on-board applications.

Considerable research has been conducted on magnesium metals to synthesize new high performance materials and develop more efficient techniques. These studies are mainly focused on the (a) element substitution [11]; (b) new production methods by using for example different hydrogen pressures [12,13]; (c) preparation of composite materials through the addition of dopants in order to improve microstructure/microchemistry [14]; and (d) annealing [15] in order to improve hydrogen storage characteristics [16].

It is known that preparation and synthesis methods are important factors which can influence the characteristics of the samples. Mechanical alloying (MA) and ball milling (BM) are widely used for preparation of Mg materials [8,11,17–19]. For powder metallurgy (PM) an important step to synthesize these compounds is sintering which improves the bonding between the powders and minimizes the porosity [20]. Unfortunately, all these methods require long times and can cause contaminations to the alloys even under protective atmosphere.

Another known technique is the hydriding combustion synthesis (HCS) which can produce much purer samples but needs a stable temperature for several hours [12,21–23].

In order to eliminate the problems caused by conventional methods, a new rapid heating technique should be used. Microwave heating is a technology that is mostly used for ceramics, carbides and ferrites and has not been applied for metals due to the fact that metals reflect microwaves. Gupta et al. [20] reported for the first time that Mg alloys can be synthesized by hybrid microwave heating [24–26]. Li et al. [27] prepared Mg_2Ni alloys using microwave-assisted activation synthesis (MAAS) and showed that these materials can absorb 3.2%wt of H_2 in only 50 s at 523 K under 3 MPa H_2. Wong et al. [28] studied the effect of microwaves on the structural and microstructural characteristics of Mg-based compounds. His team revealed that there were no defects and the surface was smooth and free of radial and circumferential cracks. They also showed that there was an increase in hardness with the addition of nanometer – scale reinforcements. In short, heating by microwaves has certain advantages over the conventional methods such as (a) reduction of processing time, (b) uniform heating, (c) improved properties and (d) environmental friendliness [29].

Recently, nanomaterials have attracted a great interest because of their unique characteristics, different from bulk materials. Therefore, a wide range of synthetic approaches regarding the preparation of metal nanoparticles in various matrices, including reduction method, sol–gel process, solvent evaporation of hydrophobic colloids have been reported [30–32]. Laser ablation which is usually applied to in-situ elemental analysis [33], forming thin film (PLD: pulsed laser deposition) [34] has been also used to prepare nanoparticles [35–42]. In particular, the temperature and pressure of the plume induced by pulsed laser irradiation onto the metal target surface in liquid are very high [43,44] compared to their values in vacuum or atmosphere because of the confinement effect. Since there are ablated particles in this plume, crystalline nanoparticles can be obtained without any heat treatments [45]. The laser ablation method offers a great advantage regarding the production of nanoparicles while aggregation and dispersion can be controlled by using surfactant or any appropriate liquid [36,46,47]. So, by this technique pure nanoparticles can be obtained and be captured in principle in any liquid. As ablated particles go through the plume induced by laser ablation in liquid in which the temperature and pressure are very high, nanoparticles with new optical, electrical and mechanical properties can be expected to be fabricated.

The development of new Mg-type of materials or composites via nanoscale fabrication techniques for more efficient hydrogen storage systems has been extensively studied by other groups [48–57]. By decreasing theoretically the particle size diameter below 2 nm, the nanoparticles of magnesium hydride have less thermodynamic stability [58,59]. Density functional theory studies have shown that the smallest enthalpy change is 57.7 kJ/molMg and corresponds to a two unit-cell thickness (1.6 Å Mg/3.0Å MgH_2) of the thin film. It is really important that this enthalpy change is over 10 kJ/molMg smaller than that of the pure bulk magnesium. At room temperature, the desired and targeted range of enthalpy change for mobile storage systems technology is 15–24 kJ/molH [60].

According to the published information on hydrogen storage technology, there is a need of air-stable materials and especially in magnesium hydrides with relatively nanosize grains, the key for the development of the air-stable nanocrystals [61] is the PMMA (polymethylmethacrylate) polymer. In order to overcome chemical or electrochemical ways of producing air-stable nanoparticles we used the laser ablation technique. It is suggested as one of the most reliable techniques for having well dispersed nanoparticles with no long-range aggregations.

Please cite this article in press as: Makridis SS, et al., Polymer-stable magnesium nanocomposites prepared by laser ablation for efficient hydrogen storage, International Journal of Hydrogen Energy (2013), http://dx.doi.org/10.1016/j.ijhydene.2013.04.031

2. Experimental

Laser ablation of solid targets into liquids is a quite new alternative physical method for fabrication of nanoparticles. The metal target was placed on the bottom of a glass cuvette filled with 1.5 mL of pure deionized water and in polymer matrices. The rod was irradiated with the fundamental (1064 nm) of a Nd:YAG laser (Quanta-Ray GCR-190, Spectra Physics) operating at 10 Hz on a rotating base with speed 4.5°/s. The laser beam was focused 1 mm below the surface target, and the irradiation time was kept constant (30 min). Upon irradiation, the solution gradually turned in different experiments from light red to wine red. The absorption spectra of the colloidal solutions were measured immediately after fabrication by a Cary UV–Visible spectrophotometer. The above procedure in polymer matrix may reveal very well dispersed nanoparticles below 5 nm.

X-ray diffraction analysis of the alloys was carried out on the powders at room temperature by using Cu-K_α radiation, in a SIEMENS D500 X-Ray diffractometer. Rietveld analysis has been performed on the XRD patterns with the use of the RIETICA software. Nanoanalysis has been performed by using an HR-TEM operating at 200 kV and equipped with a spherical aberration corrector in the objective lens, to ensure a point resolution of 1.2 A. The SCION image software has been used for the particle size analysis. The hydrogenation/dehydrogenation kinetics and cycle stability of the sample have been studied, using a Magnetic Suspension Balance (Rubotherm). In this equipment, hydrogen desorption and re-absorption, can be investigated at constant hydrogen pressures in the range from 1 to 20 MPa (flow-through mode).

3. Results and discussion

The nanoMg/PMMA composites were synthesized at room temperature from a homogeneous tetrahydrofuran (THF) solution containing the gas-selective polymer poly(methyl methacrylate) (PMMA). This polymer has been used in the sol–gel type technique elsewhere [61] and air-stable high quality nanoparticles have been produced. Laser ablation has been used to produce rapidly and more efficiently well dispersed nanoparticles for upscaling purposes in the hydrogen storage technology. We target on the development of low cost and air-stable high surface metal nanodispersions in polymer matrix.

The principle of the laser-based synthesis of nanoparticles in liquids is illustrated in Fig. 1. Here a pulsed laser beam is focused on a target in a solvent. After absorption of the laser pulse energy, the target material is vaporized and condenses in the solvent thus forming nanoparticles. The use of ultrashort pulses enables application of volatile organic solvents or monomers. In general, every combination of target material and dispersion phase is possible.

By varying the manufacturing process numerous material combinations can be tested in short time. The laser process can be called “rapid nanomaterial prototyping” or regarding the composite synthetics as “rapid nanocomposite manufacturing”, both because of the nearly unlimited material variety and because it is easy to adapt the parameters [62]. Either metallic or ceramic nanoparticles can be generated in aqueous or organic solvents [63].

The X-ray diffraction pattern of the as ablated nanoparticles in the PMMA matrix, as shown in Fig. 2, shows characteristic reflexes of a single phase hexagonal magnesium. This is attributed to a very high quality ablation in the composite matrix so that the nanoparticles do not react with the air. As an inset, it can be seen that there are no reflexes that belong to Mg–O or Mg–OH phases that deteriorate the hydrogenation capacity (it is well known the negative effect of oxidations on the metal hydride efficiency).

As revealed from the analysis of the XRD line profile broadening of each reflex, the grain size can be estimated. By using the well-known Scherrer’s formula we estimated that the grain-particle size of the nanoparticles is below 7 nm. This

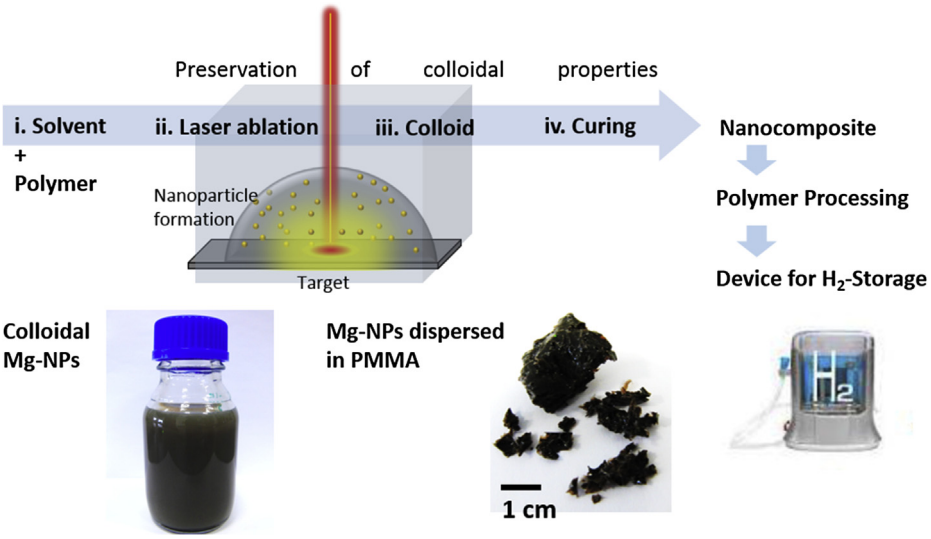

Fig. 1 – Laser-generated nanoparticles for nanocomposites (solution turns darker with the experiment, which implies the increase in nanoparticle concentration).

Please cite this article in press as: Makridis SS, et al., Polymer-stable magnesium nanocomposites prepared by laser ablation for efficient hydrogen storage, International Journal of Hydrogen Energy (2013), http://dx.doi.org/10.1016/j.ijhydene.2013.04.031

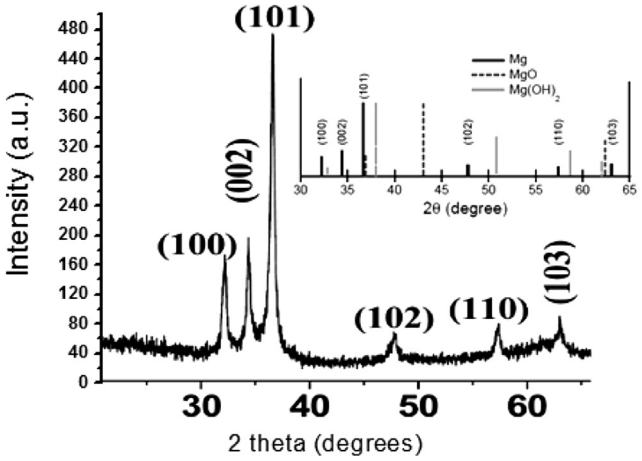

Fig. 2 – XRD pattern of Mg-nanoparticles and as inset are shown the PCPDF cards of the Mg, MgO and $Mg(OH)_2$. Only Mg (hkl) planes have been traced and indexed. Cards: Hexagonal Mg (solid black line, JCPDS 04-0770), cubic MgO (dashed black line, JCPDS 89-7746), and hexagonal $Mg(OH)_2$ (pale grey line, JCPDS 07-0239). Crystallographic characteristics: $a = 3.212$ (2) A, $c = 5.218$ (4) A.

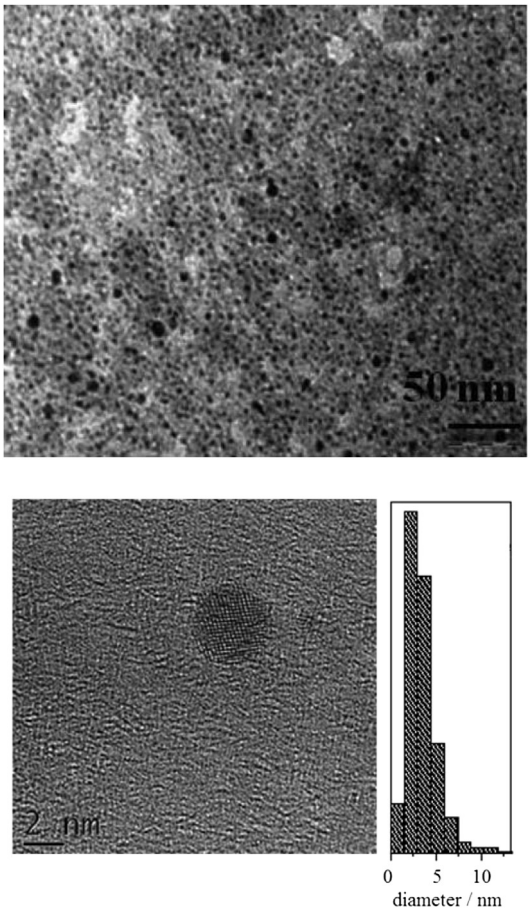

Fig. 3 – TEM (up), HR-TEM micrograph and particle size estimation (down) of laser ablated nanoMg/PMMA composite.

means that the particles in our analysis present almost half the size in comparison to the chemically produced air-stable composite Mg-nanoparticles, as it reveals from an already published work [61]. In our case, as shown in Fig. 3, the estimated particle size from the TEM analysis is very close to the experimental value. The results of the line profile analysis of the reflexes showed that the particles are much better dispersed and this should be associated to the fact that the absorption/desorption analysis is faster and more efficient in the laser ablated nanoparticles, as shown in Fig. 4, compared to other published results [61].

The fact that the particle size estimation from the TEM micrograph analysis by using the SCION image software and the XRD grain size calculations are very close suggests that the particle dispersion is much better than the sol–gel method discussed in the recently published literature ([61] and Supplementary data). As shown in Fig. 4, the kinetics and hydrogen capacity for the laser ablated Mg-nanoparticles of this work are very comparable to those of Ref. [61] but the reversible hydrogen content is considerably better (~96% of the absorbed hydrogen amount was desorbed at 250 °C in less than 20 min) since full re-chargeability has been found in our case under similar conditions. Grain-particle size distribution in the polymer matrix seems to play a mandatory role in the hydrogen reversibility and kinetics, as expected. After activation procedure, in all three charges we obtain fully saturated nanostructured materials since no difference in the curves was found in the hydrogenation/dehydrogenation procedure. A slight difference in the desorbed amount of hydrogen under both 1 bar and 10^{-2} bar (vacuum) was observed after each discharging. The absorbed amount is the same at the highest pressure of 25 bar of hydrogen. The reversibility is almost the same in all three curves and the slight difference between the three discharges could be attributed to the Mg to Mg–H ratio in the polymer matrix or to the hydrogen molecules remaining as adsorbed amount at the boundaries of Mg to polymer. Those assumptions are according to the fact that realistically, at the nanoscale,

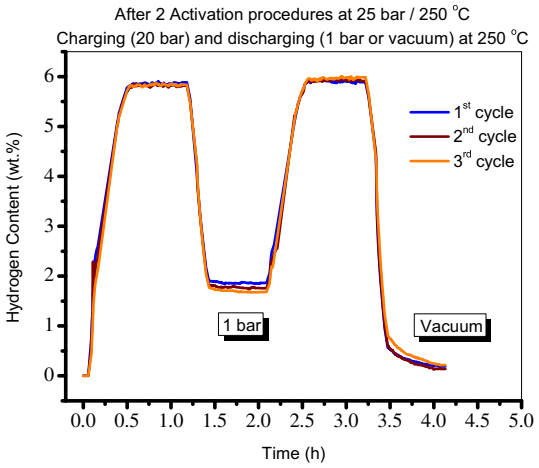

Fig. 4 – Hydrogenation/dehydrogenation process in the magnetic suspension balance equipment: Mg composite nanoparticles in PMMA.

Please cite this article in press as: Makridis SS, et al., Polymer-stable magnesium nanocomposites prepared by laser ablation for efficient hydrogen storage, International Journal of Hydrogen Energy (2013), http://dx.doi.org/10.1016/j.ijhydene.2013.04.031

hydrogen may be adsorbed also on the surface of the particle (or film).

4. Conclusions

Novel Mg-nanoparticles have been synthesized in a polymer matrix by using laser ablation, an ultrafast and highly efficient method. The latter is found to be a powerful tool to produce very fine, well dispersed, single phase nanoparticles. It is also suggested as a potential efficient technique for upscaling the production of high surface metallic particles in the hydrogen storage technology. By encapsulation in a polymer matrix, the Mg-nanoparticles exhibit more rapid, compared to other Mg-pure types, uptake of hydrogen (<20 min at 250 °C) with a high capacity (6 wt. % in Mg, 5.5 wt. % overall). Compared to the sol–gel obtained nanoparticles published elsewhere [61], the laser ablated nanoparticles have excellent reversibility under vacuum and at 250 °C, a relatively low temperature with regard to the necessary ~330 °C for Mg-bulk materials.

In future work other types of intermetallic hydrides or polymer-types could be considered for the development of novel materials for hydrogen storage purposes.

Acknowledgements

This work was partially supported by the ATLAS-H2 IAPP European Project (Grant Agreement 251562).

REFERENCES

[1] Schlapbach L, Züttel A. Hydrogen-storage materials for mobile applications. Nature 2001;414:353–8.
[2] Selvam P, Viswanathan B, Swamy CS, Srinivasan V. Magnesium and magnesium alloy hydrides. Int J Hydrogen Energy 1986;11:169–92.
[3] Song MY, Park HR. Pressure-composition isotherms in the Mg_2Ni–H_2 system. J Alloys Compd 1998;270:164–7.
[4] Reiser A, Bogdanovic B, Schlichte K. The application of mg-based metal-hydrides as heat energy storage systems. Int J Hydrogen Energy 2000;25:420–30.
[5] Kojima Y, Kawai Y, Haga T. Magnesium-based nano-composite materials for hydrogen storage. J Alloys Compd 2006;424:294–8.
[6] Huot J, Liang G, Schultz R. Mechanically alloyed metal hydride systems. Appl Phys A Mater Sci Process 2001;72:187–95.
[7] Reilly JJ, Wiswall RH. The reaction of hydrogen with alloys of magnesium and nickel and the formation of Mg_2NiH_4. J Inorg Chem 1968;7:2254–6.
[8] Zaluska A, Zaluski L, Ström-Olsen JO. Nanocrystalline magnesium for hydrogen storage. J Alloys Compd 1999;288:217–25.
[9] Orimo S, Fujii H, Ikeda K. Notable hydriding properties of a nanostructured composite material of the Mg_2Ni–H system synthesized by reactive mechanical grinding. Acta Mater 1997;45:331–41.
[10] Herrich M, Ismail N, Lyubia J, Pratt A, Gutfleisch O. Synthesis and decomposition of Mg_2FeH_6 prepared by reactive milling. Mater Sci Eng B 2004;108:28–32.
[11] Grigorova E, Khristov M, Khrussanova M, Bobet JL, Peshev P. Effect of additives on the hydrogen sorption properties of mechanically alloyed composites based on Mg and Mg_2Ni. Int J Hydrogen Energy 2005;30:1099–105.
[12] Li L, Akiyama T, Yagi J. Activation behaviors of Mg_2NiH_4 at different hydrogen pressure in hydriding combustion synthesis. Int J Hydrogen Energy 2001;26:1035–40.
[13] Kamegawa A, Goto Y, Kataoka R, Takamura H, Okada M. High-pressure synthesis of novel compounds in an Mg–Ni system. Renewable Energy 2008;33:221–5.
[14] Barkhordarian G, Klassen T, Bormann R. Effect of Nb_2O_5 content on hydrogen reaction kinetics of Mg. J Alloys Compd 2004;364:242–6.
[15] Spassov T, Solsona P, Suriñach S, Baró MD. Optimization of the ball-milling and heat treatment parameters for synthesis of amorphous and nanocrystalline Mg_2Ni-based alloys. J Alloys Compd 2003;349:242–54.
[16] Simicić MV, Zdujić M, Dimitrijević R, Nikolić-Bujanović LJ, Popović NH. Hydrogen absorption and electrochemical properties of Mg_2Ni-type alloys synthesized by mechanical alloying. J Power Sources 2006;158:730–4.
[17] Aizawa T, Kuji T, Nakano H. Synthesis of Mg_2Ni alloy by bulk mechanical alloying. J Alloys Compd 1999;291:248–53.
[18] Lee HY, Goo NH, Jeong WT, Lee KS. The surface state of nanocrystalline and amorphous Mg_2Ni alloys prepared by mechanical alloying. J Alloys Compd 2000;313:258–62.
[19] Li Q, Liu J, Liu Y, Chou KC. Comparative study on the controlled hydriding combustion synthesis and the microwave synthesis to prepare Mg_2Ni from micro-particles. Int J Hydrogen Energy 2010;35:3129–35.
[20] Gupta M, Wong WLE. Enhancing overall mechanical performance of metallic materials using two-directional microwave assisted rapid sintering. Scr Mater 2005;52:479–83.
[21] Liu D, Zhu Y, Li L. Crystal defect analysis and surface characteristics of Mg_2NiH_4 produced by hydriding combustion synthesis. Int J Hydrogen Energy 2007;32:2417–21.
[22] Li L, Saita I, Akiyama T. Intermediate products of hydriding combustion synthesis of Mg_2NiH_4 studied by optical microscopy and field-emission scanning electron microscopy. Intermetallics 2005;13:662–8.
[23] Li L, Saita I, Saito K, Akiyama T. Effect of synthesis temperature on the purity of product in hydriding combustion synthesis of Mg_2NiH_4. J Alloys Compd 2002;345:189–95.
[24] Tun KS, Gupta M. Effect of extrusion ratio on microstructure and mechanical properties of microwave-sintered magnesium and Mg/Y_2O_3 nanocomposite. J Mat Sci 2008;43:4503–11.
[25] Tun KS, Gupta M. Effect of heating rate during hybrid microwave sintering on the tensile properties of magnesium and Mg/Y_2O_3 nanocomposite. J Alloys Compd 2008;466:140–5.
[26] Tun KS, Gupta M. Development of magnesium/(yttria + nickel) hybrid nanocomposites using hybrid microwave sintering: microstructure and tensile properties. J Alloys Compd 2009;487:76–82.
[27] Liu Y, Li Q, Lin G, Chou K, Xu K. Properties of Mg_2NiH_4 prepared by microwave-assisted activation synthesis from micro-particles. J Alloys Compd 2009;468:455–61.
[28] Wong WLE, Tun KS, Gupta M. Microwave processing of magnesium based materials: a review. Kovove Mater 2011;49:219–31.
[29] Roy R, Agrawal D, Cheng J, Gedevanishvili S. Full sintering of powdered-metal bodies in a microwave field. Nature 1999;399:668–70.
[30] Teranishi T, Miyake M. Size control of Palladium nanoparticles and their crystal structures. Chem Matter 1998;10:594–600.

Please cite this article in press as: Makridis SS, et al., Polymer-stable magnesium nanocomposites prepared by laser ablation for efficient hydrogen storage, International Journal of Hydrogen Energy (2013), http://dx.doi.org/10.1016/j.ijhydene.2013.04.031

[31] Li T, Moon J, Morrone AA, Mecholsky JJ, Talham DR, Adair JH. Preparation of Ag/SiO_2 nanosize composites by a reverse micelle and sol-gel technique. Langmuir 1999;15:4328–34.
[32] Petit C, Taleb A, Pileni MP. Self-organization of magnetic nanosized cobalt particles. Adv Matter 1998;10:259–61.
[33] Nishi T, Sakka T, Oguchi H, Fukami K, Ogata YK. In-situ electrode surface analysis by laser-induced breakdown spectroscopy. J Electrochem Soc 2008;155:237–40.
[34] Xue MZ, Fu ZW. Electrochemical reactivity mechanism of $CuInSe_2$ with lithium. Thin Solid Films 2008;516:8386–92.
[35] Singh SC, Gopal R. Laser irradiance and wavelength-dependent compositional evolution of inorganic ZnO and ZnOOH/Organic SDS nanocomposite material. J Phys Chem C 2008;112:2812–9.
[36] Tilaki RM, Irajizad A, Mahdavi SM. Stability, size and optical properties of silver nanoparticles prepared by laser ablation in different carrier media. Appl Phys A 2006;84:215–9.
[37] He C, Sasaki T, Usui H, Shimizu Y, Koshizaki N. Fabrication of ZnO nanoparticles by pulsed laser ablation in aqueous media and pH-dependent particle size: an approach to study the mechanism of enhanced green photoluminescence. J Photochem Photobiol A 2007;191:66–73.
[38] Hwang CB, Fu YS, Lu YL, Jang SW, Chou PT, Wang CRC, et al. Synthesis, characterization, and highly efficient catalytic reactivity of suspended Palladium nanoparticles. J Catal 2000;195:336–41.
[39] Nichols WT, Sasaki T, Koshizaki N. Laser ablation of a platinum target in water. I. Ablation mechanisms. J Appl Phys 2006;100:114911–7.
[40] Tsuji T, Iryo K, Nishimura Y, Tsuji M. Preparation of metal colloids by a laser ablation technique in solution: influence of laser wavelength on the ablation efficiency (II). J Photochem Photobiol A 2001;145:201–7.
[41] Tsuji T, Iryo K, Ohta H, Nishimura Y. Preparation of metal colloids by a laser ablation technique in solution: influence of laser wavelength on the efficiencies of colloid formation. Jpn J Appl Phys Part2 2000;39:L981–3.
[42] Okada T, Suehiro J. Synthesis of nano-structured materials by laser-ablation and their application to sensors. Appl Surf Sci 2007;253:7840–7.
[43] Kawaguchi Y, Ding X, Narazaki A, Sato T, Niino H. Transient pressure induced by laser ablation of liquid toluene: toward the understanding of laser-induced backside wet etching. Appl Phys A 2004;79:883–5.
[44] Saito K, Sakka T, Ogata YH. Rotational spectra and temperature evaluation of C_2 molecules produced by pulsed laser irradiation to a graphite–water interface. J Appl Phys 2003;94:5530–7.
[45] Zhu MJ, Bylander DM, Kleinman L. Ferromagnetic properties of Pd monolayers. Phys Rev B 1990;42:2874–7.
[46] Angappane S, Park J, Jang Y, Hyeon T, Park JG. Magnetic Pd nanoparticles: effects of surface atoms. J Phys Condensed Matter 2008;20:295,209–295,214.
[47] Compagnini G, Scalisi AA, Puglisi O. Production of gold nanoparticles by laser ablation in liquid alkanes. J Appl Phys 2003;94:7874–7.
[48] Delhomme B, De Rango P, Marty P, Bacia M, Zawilski, Raufast Cécile, et al. Large scale magnesium hydride tank coupled with an external heat source. Int J Hydrogen Energy 2012;37:9103–11.
[49] Garrier S, Chaise A, De Rango P, Marty P, Delhomme B, Fruchart D, et al. MgH_2 intermediate scale tank tests under various experimental conditions. Int J Hydrogen Energy 2011;36:9719–26.
[50] Chaise A, De Rango P, Marty Ph, Fruchart D. Experimental and numerical study of a magnesium hydride tank. Int J Hydrogen Energy 2010;35:6311–22.
[51] Chaise A, De Rango P, Marty Ph, Fruchart D, Miraglia S, Olivès R, et al. Enhancement of hydrogen sorption in magnesium hydride using expanded natural graphite. Int J Hydrogen Energy 2009;34:8589–96.
[52] Kasperovich VS, Shelyapina MG, Kharkov B, Rykov I, Osipov V, Kurenkova E, et al. NMR study of metal-hydrogen systems for hydrogen storage. J Alloys Compd 2011;509:S804–8.
[53] Shelyapina MG, Fruchart D, Wolfers P. Electronic structure and stability of new FCC magnesium hydrides Mg7MH16 and Mg6MH16 (M = Ti, V, Nb): an ab initio study. Int J Hydrogen Energy 2010;35:2025–32.
[54] Chaise A, Marty P, De Rango P, Fruchart D. A simple criterion for estimating the effect of pressure gradients during hydrogen absorption in a hydride reactor. Int J Heat Mass Transfer 2009;52:4564–72.
[55] Marty Ph, Fourmigue JF, De Rango P, Fruchart D, Charbonnier J. Numerical simulation of heat and mass transfer during the absorption of hydrogen in a magnesium hydride. Energy Convers Manage 2006;47:3632–43.
[56] Siretskiy MYu, Shelyapina MG, Fruchart D, Miraglia S, Skryabina NE. Influence of a transition metal atom on the geometry and electronic structure of Mg and Mg–H clusters. J Alloys Compd 2009;480:114–6.
[57] de Rango P, Chaise A, Charbonnier J, Fruchart D, Jehan M, Marty Ph, et al. Nanostructured magnesium hydride for pilot tank development. J Alloys Compd 2007;446, 447:52–7.
[58] Cheung S, Deng WQ, van Duin ACT, Goddard WA. ReaxFF: MgH reactive force field for magnesium hydride systems. J Phys Chem A 2005;109:851–9.
[59] Wagemans RWP, van Lenthe JH, de Jongh PE, Jos van Dillen A, de Jong KP. Hydrogen storage in magnesium clusters: quantum chemical study. J Am Chem Soc 2005;127:16,675–16,680.
[60] Batsoulis N, Makridis SS, Stubos AK. Nano-theoretical engineering of Mg and Mg_2Ni hydrogen absorption/desorption character for electrochromic and energy efficient solar applications, NANOSMAT-5; 2010.
[61] Jeon KJ, Moon HR, Ruminski AM, Jiang B, Kisielowski C, Bardhan R, et al. Air-stable magnesium nanocomposites provide rapid and high-capacity hydrogen storage without using heavy-metal catalysts. Nat Mater 2011;10:286–90.
[62] Wagener P, Brandes G, Schwenke A, Barcikowski S. Impact of in situ polymer coating on particle dispersion into solid laser-generated nanocomposites. Phys Chem Chem Phys 2011;13:5120–6.
[63] Bärsch N, Jakobi J, Weiler S, Barcikowski S. Pure colloidal metal and ceramic nanoparticles from high-power picosecond laser ablation in water and acetone. Nanotechnology 2009;20:445,603–445,611.

Please cite this article in press as: Makridis SS, et al., Polymer-stable magnesium nanocomposites prepared by laser ablation for efficient hydrogen storage, International Journal of Hydrogen Energy (2013), http://dx.doi.org/10.1016/j.ijhydene.2013.04.031

Assessing the Identifiability in Isotope Exchange Depth Profiling Measurements

Francesco Ciucci [1,2], Grigorios Panagakos[3], Chi Chen[1], Dengjie Chen[1]

1) The Hong Kong University of Science and Technology, Dept. of Mechanical Engineering.

2) The Hong Kong University of Science and Technology, Dept. of Chemical and Biomolecular Engineering.

3) Technical University of Denmark, Department of Micro- and Nano-technology

Abstract

Accurate identification of the physical parameters describing the surface exchange kinetic coefficient *k* and oxygen diffusion coefficient *D* can shed light on the development of solid state ionics, as many ionic devices highly rely on the behavior of such parameters. In this work we extend and generalize the concept of identifiability in Isotope Exchange Depth Profiling (IEDP), an important characterization tool in the ionics field by exploring the measurability of *k* and *D* as a function of two dimensionless quantities, the Biot number, and the annealing time divided by the diffusional time scale. In addition we show a novel approximate computation for the confidence intervals for *k* and *D*. The new estimator, which is proportional to the error done in the IEDP measurement and inversely proportional to the number of measurement points, gives a generalized estimate for the confidence bands of both parameters.

KEYWORDS: Diffusion, Isotope Exchange, Identification, Biot number, Mixed conductor.

1 Introduction

The identification of the desired parameters *k* and *D* is usually performed by fitting the results of a relevant experimental technique against a model sufficiently describing the incorporation of oxygen through a surface and its transport through the bulk of a material. Researchers and practitioners in the area of ionics often employ Electrical Conductivity Relaxation (ECR) [1], Electrochemical Impedance Spectroscopy (EIS) and Isotope Exchange Depth Profiling (IEDP) [2-4]. IEDP has received a lot of attention [5], since it is the only of the relevant methods described above that can directly probe the isotope profile on mixed conducting materials.

By mapping the IEDP with secondary ion mass spectrometry (SIMS), the aforementioned parameters *k* and *D* can be successfully determined. This technique has already been widely applied for the characterization of bulk samples. Recently, thin film samples, e.g., $Ba_{0.5}Sr_{0.5}Co_{0.8}Fe_{0.2}O_{3-\delta,}$ [6], $PrBaCo_2O_{5+\delta}$ [7], and $La_{1-x}Sr_xCoO_{3-\delta}$ [8], were also performed by using this method, but special attention should be paid to obtain the accurate parameters when considering the characteristic length.

Establishing the confidence regions for the estimated parameters in IEDP and determining how to improve the measurement accuracy is critically important for further development of the technique. Sensitivity analysis, asymptotic statistics and heuristic methods are some of the tools that have been employed in the past. Strategies to understand the measurability of both *k* and *D* in the context of IEDP [9-11] and ECR [12, 13] have been discussed in previous reports. This work generalizes previous results by framing the identification problem in terms of non-dimensional time and Biot number, hereby making it applicable to nearly all thin film IEDP works. In particular we prove that our *k* and *D* standard deviation estimates depend linearly on the number *N* of IEDP measurement points and on the standard deviation of the measurement error.

2 Theory

2.1 Model

The concept of the Biot number is well established in heat transfer problems coupling both convection and conduction. In an analogous way, the Biot number Bi for reaction/diffusion problems arising in ionics may be defined as the ratio of the diffusion and the reaction time scales [13]. If the former is defined as $\tau_D = \frac{L^2}{D}$ and the latter as $\tau_k = \frac{L}{k}$, where L is a characteristic time scale, then the chemical Biot number is given as $\mathrm{Bi} = \frac{\tau_D}{\tau_k} = \frac{kL}{D}$.

IEDP measurements are typically fitted against an analytical model describing one-dimensional unsteady Fickian diffusion coupled with linearized surface kinetics. Such model outputs the normalized concentration $c^*\left(t_{\mathrm{exp}}, x\right)$ of tracer $^{18}\mathrm{O}$ as a function of position x and annealing time t_{exp}. The corresponding diffusion equation describing the IEDP response can be solved to give the following expression [8, 10, 14]

$$c^*(t^*_{\mathrm{exp}}, \mathrm{Bi}, \frac{x}{L}) = 1 - \sum_{n=1}^{\infty} \frac{2\ \mathrm{Bi} \quad \cos\left(\beta_n\ (1 - \frac{x}{L})\right) \exp(-\beta_n^2\ t^*)}{(\beta_n^2 + \mathrm{Bi}^2 + \mathrm{Bi})\cos(\beta_n)} \qquad (1)$$

where the β_n's are the positive roots of the transcendental equation $\beta\ \tan\beta = \mathrm{Bi}$ and t^* is the normalized time defined as $t^*_{\mathrm{exp}} = \frac{t_{\mathrm{exp}}}{\tau_D}$.

2.2 Statistical Analysis of *k* and *D* Estimation

Since the goal of a typical IEDP experiment is to evaluate both parameters *k* and *D* with good confidence, we need to address the confidence bands of these parameters. For that, we take the classical (frequentist) statistical approach . That is we assume that the measured normalized isotope concentration is given by the stochastic process $c^*_{\text{meas}} = c^*(t^*_{\text{exp}}, \text{Bi}, \frac{x}{L}) + \epsilon$, where $c^*\left(t^*_{\text{exp}}, \overline{\text{Bi}}, \frac{x}{L}\right)$ is the noise-free outcome of a measurement and ϵ is a uncorrelated Gaussian error with standard deviation σ^2. We recall that we have denoted with *k* and *D* the parameters that we need to identify and with Bi the corresponding Biot number. On the other hand, $\bar{k}$ and $\bar{D}$, the "exact" or "true" values of the same parameters, correspond to the "exact" or "true" Biot number $\overline{\text{Bi}}$. A previous publication showed that the relative errors on the parameters *k* and *D* can be obtained from the following asymptotic covariance matrix

$\mathbf{V} = \sigma^2(\mathbf{J}\mathbf{J}^{\mathrm{T}})^{-1}$	(2)

where $(\boldsymbol{J})_{1j} = k\frac{\partial c^*\left(t^*_{\text{exp}}, \overline{\text{Bi}}, \frac{x_j}{L}\right)}{\partial k}$, $(\boldsymbol{J})_{2j} = D\frac{\partial c^*\left(t^*_{\text{exp}}, \overline{\text{Bi}}, \frac{x_j}{L}\right)}{\partial D}$ [1]. In this last expression we have denoted with x_j the location of the j-th spatial measurement. Furthermore we note that the $\mathbf{J}\mathbf{J}^{\mathrm{T}}$ may be seen as

$(\mathbf{J}\mathbf{J}^{\mathrm{T}})_{11} = \sum_{j=1}^{N}\left(k\frac{\partial c^*\left(t^*_{\text{exp}}, \overline{\text{Bi}}, \frac{x_j}{L}\right)}{\partial k}\right)^2$	(3)

[1] It is also easy to show that $k\frac{\partial c^*}{\partial k} = \text{Bi}\frac{\partial c^*}{\partial \text{Bi}}$ and $D\frac{\partial c^*}{\partial D} = -\text{Bi}\frac{\partial c^*}{\partial Bi} + t^*\frac{\partial c^*}{\partial t^*}$.

$$(\mathbf{J}\mathbf{J}^{\mathrm{T}})_{12} = (\mathbf{J}\mathbf{J}^{\mathrm{T}})_{21} = \sum_{j=1}^{N} \left(k \frac{\partial c^* \left(t^*_{\mathrm{exp}}, \overline{\mathrm{Bi}}, \frac{x_j}{L} \right)}{\partial k} \right) \left(D \frac{\partial c^* \left(t^*_{\mathrm{exp}}, \overline{\mathrm{Bi}}, \frac{x_j}{L} \right)}{\partial D} \right)$$	(4)
$$(\mathbf{J}\mathbf{J}^{\mathrm{T}})_{22} = \sum_{j=1}^{N} \left(k \frac{\partial c^* \left(t^*_{\mathrm{exp}}, \overline{\mathrm{Bi}}, \frac{x_j}{L} \right)}{\partial k} \right)^2$$	(5)

It is easy to prove that the matrix **V** is in general positive semi-definite and the isosurfaces of the corresponding quadratic form (the confidence regions) are ellipsoids [15]. Typically, one may map these ellipsoids into scalar quantities, which describe one of their geometric features. The function $\phi_D = \det(\boldsymbol{V})$ is commonly used to assess the overall quality of the experiment since it is closely linked to the volume of the confidence region[16] . We shall employ this quantity later in the manuscript.

An alternative to the asymptotic covariance matrix $\boldsymbol{V}$ is derived by recalling the definition of trapezoidal quadrature rules and by assuming that the spacing between the experimental points is uniform. In order to keep the notation compact we shall define the square of the sensitivity with respect to *k* at a location x_j as $S_k^2\left(\frac{x_j}{L}\right) = \left(k \frac{\partial c^* \left(t^*_{\mathrm{exp}}, \overline{\mathrm{Bi}}, \frac{x_j}{L} \right)}{\partial k} \right)^2$. This allows us to rewrite (3) as

$$(\mathbf{J}\mathbf{J}^{\mathrm{T}})_{11} = \frac{1}{2} S_k^2\left(\frac{x_1}{L}\right) + \frac{1}{2} \sum_{j=1}^{N-1} \left[S_k^2\left(\frac{x_j}{L}\right) + f\left(\frac{x_{j+1}}{L}\right) \right] + \frac{1}{2} S_k^2\left(\frac{x_N}{L}\right)$$	(6)

The mid-term in the right hand side of the previous expression can be further approximated as[2]

$$\frac{N-1}{L}\int_0^L S_k^2\left(\frac{x}{L}\right)\mathrm{d}x \approx \frac{1}{2}\sum_{j=1}^{N-1}\left[S_k^2\left(\frac{x_j}{L}\right)+S_k^2\left(\frac{x_{j+1}}{L}\right)\right] \quad (7)$$

If we eliminate the first and last term of (6) and substitute back the last expression then we can approximate the $(\mathbf{J}\mathbf{J}^{\mathrm{T}})_{11}$ as *N-1* times the average k-sensitivity squared $\langle S_k^2\rangle$ ($\langle\cdot\rangle$ indicates the space average over the sample depth)

$$(\mathbf{J}\mathbf{J}^{\mathrm{T}})_{11} \approx \frac{N-1}{L}\int_0^L S_k^2\,\mathrm{d}x = (N-1)\langle S_k^2\rangle \quad (8)$$

More generally we can write

$$\mathbf{J}\mathbf{J}^{\mathrm{T}} \approx (N-1)\begin{pmatrix}\langle S_k^2\rangle & \langle S_k\ S_D\rangle\\ \langle S_k\ S_D\rangle & \langle S_D^2\rangle\end{pmatrix} \quad (9)$$

where S_D is the relative sensitivity on *D*. This leads to the following approximated asymptotic covariance matrix

$$\mathbf{V}^{\mathrm{approx}} = \frac{\sigma^2}{N-1}\begin{pmatrix}\langle S_k^2\rangle & \langle S_k\ S_D\rangle\\ \langle S_k\ S_D\rangle & \langle S_D^2\rangle\end{pmatrix}^{-1} \quad (10)$$

This formulation has a main advantage over expression (2) in that **V** is directly proportional to *N*. In addition it indicates that if the integral of the sensitivities over the domain increases, then *k* and *D* can be captured with greatest confidence. This is intuitive and useful for assessing identifiability of IEDP. An alternative option in order to assess measurability is to monitor the actual sensitivity of both *k* and *D*. If the maximum sensitivity of the parameter is above a certain threshold value, then one may infer that the parameter is measurable. This alternative approach, while useful and

[2] Note that analogous expressions can be found for non-uniform x_j spacing.

particularly suitable for ECR [13], was not employed here as it required the plot of a quantity depending on three variables.

3 Results

In contrast with earlier work which addressed the identifiability of the parameters *k* and *D* as a function of dimensional quantities, here we generalize identifiability results to be a function of Bi and *t** and we plot the relative asymptotic standand deviation of both parameters in Figure 1. In Figure 1 (a) we report the relative standard deviation for *k*; in particular, we depict the $\log_{10}$ of the following quantity

$$\sigma_k^* = \sqrt{\frac{N-1}{\sigma^2}\left(\mathbf{V}^{\text{approx}}\right)_{11}} \qquad (11)$$

We note that identifiability of *k* is greatest (lowest σ_k^*) for $\text{Bi} \ll 1$. This is because, when $\tau_k \gg \tau_D$ the behavior of the system is controlled entirely by the reaction kinetics and the any diffusional perturbation has sufficent time to relax, hence the optimal time t_{exp} is found to be of the order of τ_k . More specifically the optimal identifiability is found for $\text{Bi} = 10^{-2}$ and for $t_{\text{exp}} \approx 0.47\ \tau_k$ within the bounds of Figure 1.

We perform a similar analysis on the normalized standard deviation on the estimated *D* by plotting the $\log_{10} \sigma_D^*$, where σ_D^* is

$$\sigma_D^* = \sqrt{\frac{N-1}{\sigma^2}\left(\mathbf{V}^{\text{approx}}\right)_{22}} \qquad (12)$$

It is clear from Figure 1 (b), that the parameter *D* is characterized by lowest relative error for $\text{Bi} \gg 1$. This is consistent with intuition. In fact, if $\tau_D \gg \tau_k$ the system is diffusion-controlled, in other words chemical reaction kinetics is extremely fast and the system will only witness changes

due to diffusion. This entails that the system will be sensitive solely to *D*. In addition, the optimal time is found for $t_{\text{exp}} \sim \tau_D$. More specifically, in the Figure the identifiability of *D* is optimal for $\text{Bi} = 10^2$ in the domain and for $t_{\text{exp}} \approx 0.23\ \tau_D$. Figure 1 is also significant because it provides an actual quantitative value for the $\mathbf{V}^{\text{approx}}$**.** If one has *N*, the number of experimental points, a suitable guesses for the experimental error σ^2 , the Biot number and experimental time, then one may be able to quickly quantify the confidence on the *k* and *D* obtained by IEDP, and example determine if different anneal time is required.

Some of the information contained in the two panels is also show in Figure 2 (a) , where the minima of σ_k^* and σ_D^* for Biot numbers ranging from 10^{-2} to 10^2 are shown. The minima are computed with respect to the experimental anneal time t_{exp}^*. This quantity is in turn reported Figure 2 (b). The same trend as above is retrieved: *k* is identifiable for $\text{Bi} \ll 1$, and *D* is identifiable for $\text{Bi} \gg 1$. Identifiability for both parameters is achievable only for $\text{Bi} \sim 1$. Aside from that this figure is significant because for a given Bi it provides the minimum error that can be obtained when identifying either *k* and *D*. As shown in Figure 2 (b), optimal identifiability of *k* is achieved for $t_{\text{exp}} \sim \text{Bi}$ ($\tau_D = \tau_k$), while the minimum *D*-error is obtained for $t_{\text{exp}} \sim \tau_D$.

In Figure 3 we report of the dimensionless conterpart of ϕ_D defined as $\phi_D^* = \frac{N-1}{\sigma^2} \det\left(\boldsymbol{V}^{\text{approx}}\right)$. This quantity provides a measure of the confidence region volume. Thereby, it defines a criterion for simulataneous identifiability of *k* and *D*. A minimum can be seen at $\text{Bi} \approx 2.35$ and $t_{\text{exp}} \approx 0.43\ \tau_D$. This minimum is in the region where the dynamics of IEDP is controlled by both the diffusion and the reaction processes. As already mentioned above, if this is the case, then the concentration of tracer atoms is sensitive to both *D* and *k*, allowing identification of both parameters. It should be noted though that the heuristic criterion that states that optimality for IEDP

identification occurs at Bi $= 1$ ($\tau_k = \tau_D$) and for $t_{\exp} = \tau_D$ seems to be only qualitative, confirming earlier ECR results

Lastly, we checked whether the computed σ_k^* and σ_D^* match the corresponding quantities computed using the approximation given by (2); the latter were shown to capture estimated parameter distributions well for synthetic EIS, IEDP and ECR experiments [10, 13, 17, 18]. For this purpose we compared the following two quantities: $\Delta\sigma_k^* = \frac{\left|\sqrt{\left(\mathbf{V}^{\text{approx}}\right)_{11}} - \sqrt{(\mathbf{V})_{11}}\right|}{\sqrt{\left(\mathbf{V}^{\text{approx}}\right)_{11}}}$ and $\Delta\sigma_D^* = \frac{\left|\sqrt{\left(\mathbf{V}^{\text{approx}}\right)_{22}} - \sqrt{(\mathbf{V})_{22}}\right|}{\sqrt{\left(\mathbf{V}^{\text{approx}}\right)_{22}}}$. These represent of the errors we make on approximating the confidence bands (2) with (10) for *k* and D respectively. We find that the error decays both cases with *N* and that in a log-log plot this decay is linear. In Figure 4 we report $\Delta\sigma_k^*$ for Bi = 1 and $t_{\exp}^* = 1$ and note that similar trends are found for $\Delta\sigma_D^*$

4 Conclusions

In this article we address the identifiability of parameters *k* and *D* obtained from IEDP experiments. We take a frequentist approach and we compute the relative errors on the estimated *k* and *D* through asymptotic analysis. We also propose an additional approximation for the covariance matrix $\boldsymbol{V}$ which is based on the space-averaged sensitivities of the normalized concentration with respect to the parameters *k* and *D*.

While sensitivity analysis provides only a qualitative view on the identifiability of k and D, our present approach generalizes such concepts. We found a novel estimator which provides the

standard deviations on *k* and *D*. Such standard deviations are shown to be proportional to the experimental error and inversely proportional to the square root of the number of experimental points measured. In addition the normalized errors are shown to be dependent only on the Biot number and dimensionless experimental time. This generalizes concepts derived in previous work and provides a quick reference for assessing the identifiability of *k* and *D* in IEDP experiments.

AUTHOR INFORMATION

Corresponding Author

Francesco Ciucci mefrank@ust.hk

Acknowledgements

FC thanks HKUST for providing startup funds. FC, CC and DC acknowledge partial support from DAG grants DAG12EG07-12 and DAG12EG06.

REFERENCES

[1] D. Chen, Z. Shao, *Intl J Hydrogen Energ* **36** (2011) (11) 6948.
[2] J.A. Kilner, R.A. De Souza, I.C. Fullarton, *Solid State Ionics* **86–88, Part 2** (1996) (0) 703.
[3] R.A. De Souza, M. Martin, *MRS Bulletin* **34** (2009) (12) 907.
[4] R.A. De Souza, R.J. Chater, *Solid State Ionics* **176** (2005) (23–24) 1915.
[5] J.R. Macdonald, *Ann. Biomed. Eng.* **20** (1992) (3) 289.
[6] L. Wang, R. Merkle, J. Maier, T. Acarturk, U. Starke, *APPLIED PHYSICS LETTERS* **94** (2009) (7) 071908.
[7] G. Kim, S. Wang, A.J. Jacobson, Z. Yuan, W. Donner, C.L. Chen, L. Reimus, P. Brodersen, C.A. Mims, *Appl Phys Lett* **88** (2006) (2) 024103.
[8] M. Kubicek, Z. Cai, W. Ma, B. Yildiz, H. Hutter, J. Fleig, *ACS Nano* **7** (2013) (4) 3276.
[9] E. Fischer, J.L. Hertz, *Solid State Ionics* **218** (2012) (0) 18.
[10] F. Ciucci, *Solid State Ionics* **232** (2013) (0) 97.
[11] P. Fielitz, G. Borchardt, *Solid State Ionics* **144** (2001) (1–2) 71.
[12] R.A. Cox-Galhotra, S. McIntosh, *Solid State Ionics* **181** (2010) (31–32) 1429.
[13] F. Ciucci, *Solid State Ionics* **239** (2013) (0) 28.
[14] J. Zapata, M. Burriel, P. Garcia, J.A. Kilner, J. Santiso, *Journal of Materials Chemistry A* (2013).
[15] L. Wasserman, *All of Statistics: A Concise Course in Statistical Inference*, Springer (2003).
[16] A.C. Atkinson, A.N. Donev, *Optimum experimental design*, Clarendon Press (1992).
[17] F. Ciucci, T. Carraro, W.C. Chueh, W. Lai, *Electrochim. Acta* **56** (2011) (15) 5416.
[18] F. Ciucci, *Electrochim Acta* **87** (2013) (0) 532.

(a)

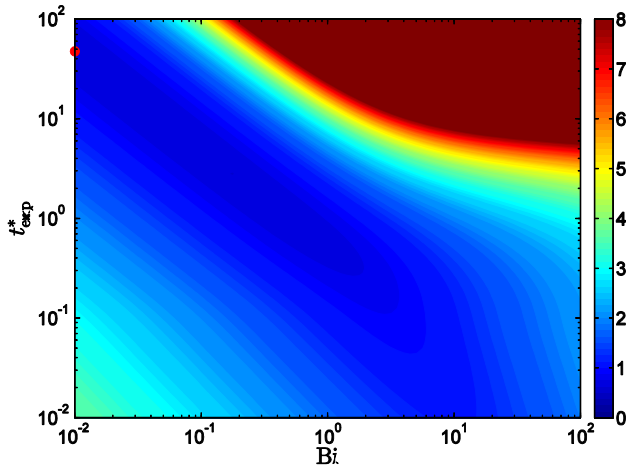

(b)

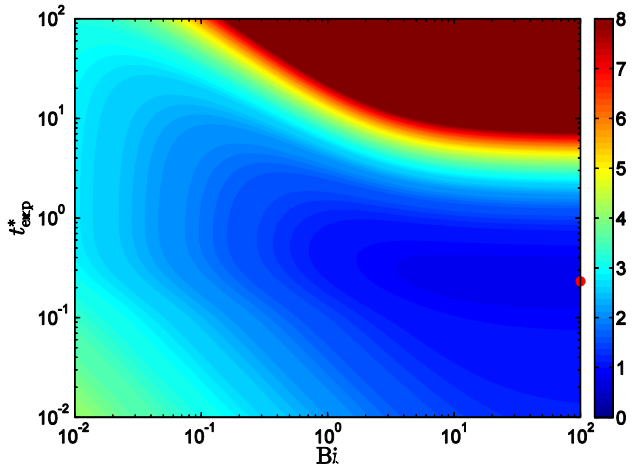

Figure 1

(a) Contour plot of $\log_{10} \sigma_k^*$, the log10 of the normalized relative standard deviation on k as a function of Bi, the Biot number, and t^*_{exp}, the anneal time normalized with respect to the diffusional timescale. (b) Contour plot $\log_{10} \sigma_D^*$, the log10 of the normalized relative standard deviation on k, versus Biot number and t^*_{exp}. The corresponding minima are highlighted in the plots with a red dot.

(a)

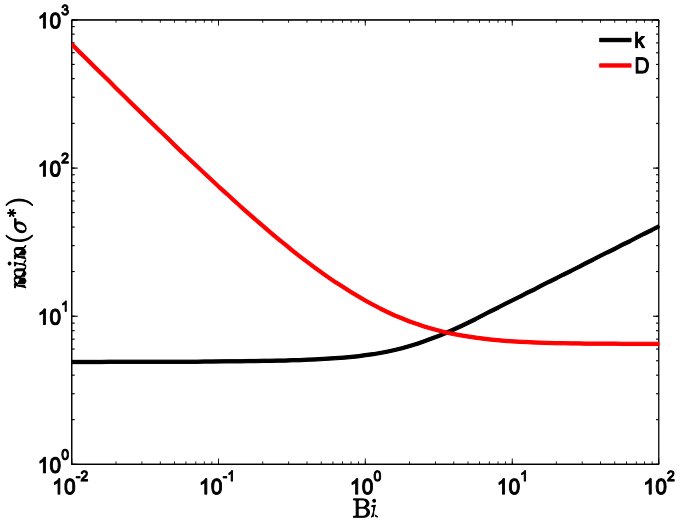

(b)

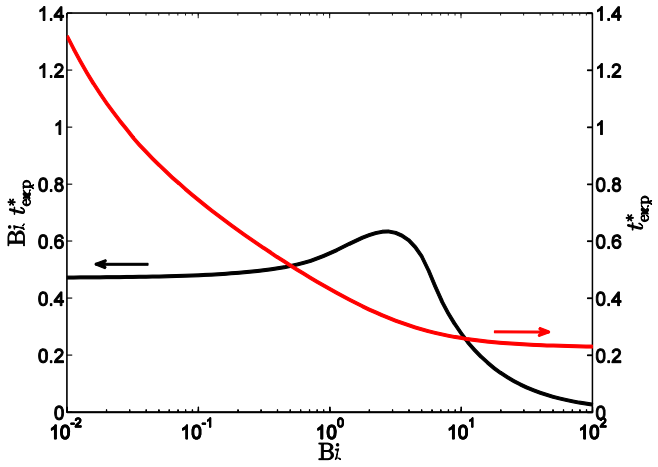

Figure 2

(a) Plot of the minimal values of σ_k^* and σ_D^* as a function of the Biot number.The mimimum is obtained by mimizing $t_{\exp}^*$. (b) Plot of the $t_{\exp}^*$ at which the minimum σ_k^* and σ_D^* are achieved. The corresponding k-minimal time is plotted as $t_{\exp}^* = t_{\exp}/\tau_D$.

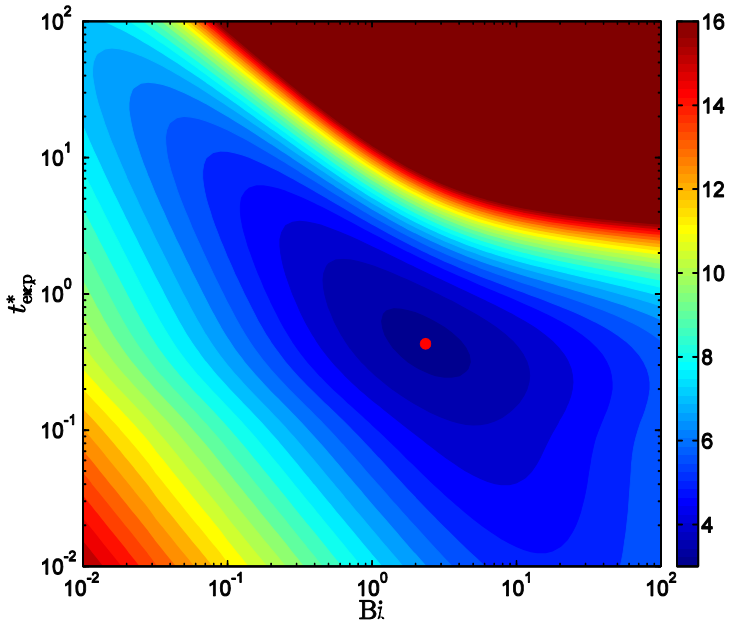

Figure 3

Contour plot of $\log_{10} \phi_D^*$ as a function of Bi and t^*_{exp}. The minimum is shown with a red dot.

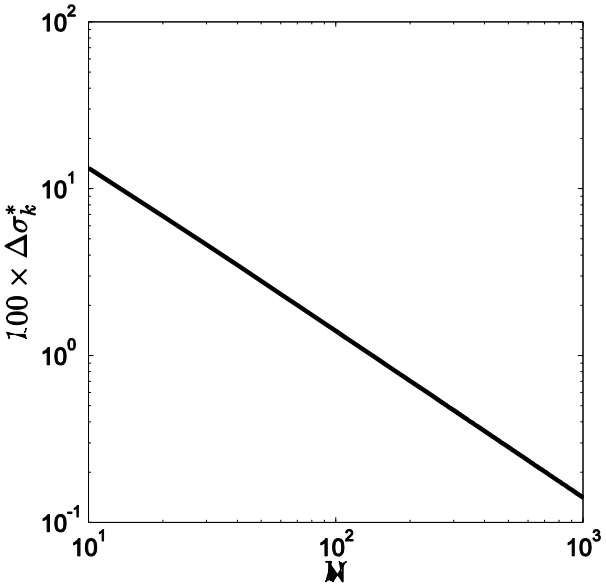

Figure 4

Relative $\Delta\sigma_k^*$ error, expressed in percent, due to the novel confidence band approximation versus the number of experimental points *N*.